

GEOLOGIC MAP OF THE TENALQUOT PRAIRIE AND NORTHERN TWO-THIRDS OF THE VAIL 7.5-MINUTE QUADRANGLES, THURSTON AND PIERCE COUNTIES, WASHINGTON

by Michael Polenz, Frank R. Hladky, Megan L. Anderson,
Jeffrey H. Tepper, Alison E. Horst, Daniel P. Miggins,
and Gabriel Legoretta Paulín

WASHINGTON
GEOLOGICAL SURVEY
Map Series 2021-02
December 2021

INTERNALLY REVIEWED



WASHINGTON STATE DEPARTMENT OF
NATURAL RESOURCES
WASHINGTON GEOLOGICAL SURVEY

GEOLOGIC MAP OF THE TENALQUOT PRAIRIE AND NORTHERN TWO-THIRDS OF THE VAIL 7.5-MINUTE QUADRANGLES, THURSTON AND PIERCE COUNTIES, WASHINGTON

by Michael Polenz, Frank R. Hladky, Megan L. Anderson, Jeffrey H. Tepper,
Alison E. Horst, Daniel P. Miggins, and Gabriel Legoretta Paulín

WASHINGTON
GEOLOGICAL SURVEY
Map Series 2021-02
December 2021

*This geologic map was funded in part by
the USGS National Cooperative Geologic
Mapping Program, award no. G20AC00247*

*This publication has been subject to an iterative technical review
process by at least one Survey geologist who is not an author.
This publication has also been subject to an iterative
review process with Survey editors and cartographers.*



WASHINGTON STATE DEPARTMENT OF
NATURAL RESOURCES
WASHINGTON GEOLOGICAL SURVEY

DISCLAIMER

Neither the State of Washington, nor any agency thereof, nor any of their employees, makes any warranty, express or implied, or assumes any legal liability or responsibility for the accuracy, completeness, or usefulness of any information, apparatus, product, or process disclosed, or represents that its use would not infringe privately owned rights. Reference herein to any specific commercial product, process, or service by trade name, trademark, manufacturer, or otherwise, does not necessarily constitute or imply its endorsement, recommendation, or favoring by the State of Washington or any agency thereof. The views and opinions of authors expressed herein do not necessarily state or reflect those of the State of Washington or any agency thereof.

INDEMNIFICATION

Research supported by the U.S. Geological Survey, National Cooperative Geologic Mapping Program, under USGS award number G20AC00247. The views and conclusions contained in this document are those of the authors and should not be interpreted as necessarily representing the official policies, either expressed or implied, of the U.S. Government.

WASHINGTON STATE DEPARTMENT OF NATURAL RESOURCES

Hilary S. Franz—*Commissioner of Public Lands*

WASHINGTON GEOLOGICAL SURVEY

Casey R. Hanell—*State Geologist*

Jessica L. Czajkowski—*Assistant State Geologist*

Ana Shafer—*Assistant State Geologist*

Washington State Department of Natural Resources Washington Geological Survey

Mailing Address:

1111 Washington St. SE

MS 47007

Olympia, WA 98504-7007

Street Address:

Natural Resources Bldg, Rm 148

1111 Washington St SE

Olympia, WA 98504

Phone: 360-902-1450

Fax: 360-902-1785

Email: geology@dnr.wa.gov

Website: <http://www.dnr.wa.gov/geology>

Publications and Maps:

[www.dnr.wa.gov/programs-and-services/geology/
publications-and-data/publications-and-maps](http://www.dnr.wa.gov/programs-and-services/geology/publications-and-data/publications-and-maps)



Washington Geology Library Searchable Catalog:

[www.dnr.wa.gov/programs-and-services/geology/
washington-geology-library](http://www.dnr.wa.gov/programs-and-services/geology/washington-geology-library)

Suggested Citation: Polenz, Michael; Hladky, F. R.; Anderson, M. L.; Tepper, J. H.; Horst, A. E.; Miggins, D. P.; Legoretta Paulín, Gabriel, 2021, Geologic map of the Tenalquot Prairie and northern two-thirds of the Vail 7.5-minute quadrangles, Thurston and Pierce Counties, Washington: Washington Geological Survey Map Series 2021-02, 1 sheet, scale 1:24,000, 47 p. text. [https://www.dnr.wa.gov/publications/ger_ms2021-02_geol_map_tenalquot_prairie_northern_vail_24k.zip]



POLENZ, MICHAEL

Michael Ber
December 2021

Contents

Introduction	1
Geologic Overview	2
Bedrock	2
Unlithified Glacial Deposits.....	2
Overview of Regional Structure	2
Geologic Hazards.....	3
Methods.....	3
Geologic Mapping	3
Geophysics.....	3
Description of Map Units.....	3
Holocene to Pleistocene Nonglacial Deposits	3
Pleistocene Glacial and Nonglacial Sediments.....	5
Eocene Volcanic and Sedimentary Rocks.....	9
Discussion	12
Eocene Bedrock	12
Whole Rock Geochemistry	15
Description of Structures	15
Suggestions for Further Study.....	19
Acknowledgments.....	19
Author roles	19
References.....	19
Appendix A. New Luminescence Age Estimate	24
Appendix B. New Detrital U/Pb Age Estimate	27
Appendix C. New $^{40}\text{Ar}/^{39}\text{Ar}$ Age Estimates.....	29

FIGURES

Figure 1. Gabbro inclusions in Northcraft lava flow	13
Figure 2. Northern highwall of the Columbia Granite Quarry.....	14
Figure 3. Total alkalis versus silica plot	16
Figure 4. AFM diagram.....	16
Figure 5. SiO_2 –FeO/MgO plot.....	17
Figure 6. MORB-normalized spider diagram	17
Fig A1A. Age distributions as a radial plot and histogram	25
Fig A1B. Anomalous fading measurement for a representative aliquot	25
Fig A1C. Typical IRSL decay curve for a naturally dosed aliquot.....	26
Fig A1D. Typical OSL decay curve for a naturally dosed aliquot.....	26
Figure B1A. Concordia plot $^{207}\text{Pb}/^{206}\text{Pb}$ vs. $^{238}\text{U}/^{206}\text{Pb}$	27
Figure B1B. Concordia plot $^{206}\text{Pb}/^{238}\text{U}$ vs. $^{207}\text{Pb}/^{235}\text{U}$	28
Figure B1C. Spectrum of Detrital Zircon Ages from age site GD4	28
Figure C1. Step-heating results for $^{40}\text{Ar}/^{39}\text{Ar}$ analysis on unit Eva_n at age site GD5.....	33
Figure C2. Step-heating results for $^{40}\text{Ar}/^{39}\text{Ar}$ analysis on unit Eva_n at age site GD6.	35
Figure C3. Step-heating results for $^{40}\text{Ar}/^{39}\text{Ar}$ analysis on unit Eva_n at age site GD7.....	37
Figure C4. Step-heating results for $^{40}\text{Ar}/^{39}\text{Ar}$ analysis on unit Eva_n at age site GD8.....	39
Figure C5. Step-heating results for $^{40}\text{Ar}/^{39}\text{Ar}$ analysis on unit Eva_n at age site GD9.....	41
Figure C6. Step-heating results for $^{40}\text{Ar}/^{39}\text{Ar}$ analysis on unit Eva_n at age site GD10.....	43
Figure C7. Step-heating results for $^{40}\text{Ar}/^{39}\text{Ar}$ analysis on unit Eig_n at age site GD11.	45

TABLES

Table 1. Clast composition ranges from 17 clast counts from the map area (Yelm lobe derivation) compared with clast counts from the Olympia lobe drift west of the map area	5
Table 2. New Northcraft Formation radiometric ages from the map area	10
Table 3. Comparison of chemical traits of rock from Littlerock quadrangle unit Evb (Polenz and others, 2017) lava versus Northcraft Formation (this study).	19
Table A1. Optically Stimulated Luminescence (OSL) and Infrared Stimulated Luminescence (ISL) results from Age Site GD3	24
Table B1. Detrital zircon maximum constraining age on tuffaceous sediment.	27
Table C1. Summary of seven new $^{40}\text{Ar}/^{39}\text{Ar}$ ages from the Tenalquot Prairie and Vail 7.5-minute quadrangles	30

MAP SHEET

Geologic Map of the Tenalquot Prairie and Northern Two-Thirds of the Vail
7.5-Minute Quadrangles, Thurston and Pierce Counties, Washington

Figure M1. Geophysical interpretation for the map area

Geologic Map of the Tenalquot Prairie and Northern Two-Thirds of the Vail 7.5-minute Quadrangles, Thurston and Pierce Counties, Washington

by Michael Polenz¹, Frank R. Hladky¹, Megan L. Anderson¹, Jeffrey H. Tepper², Alison E. Horst¹, Daniel P. Miggins³, Gabriel Legoretta Paulín⁴

¹ Washington
Geological Survey
MS 47007
Olympia, WA
98504-7007

² Department of Geology
University of
Puget Sound
1500 N Warner St. #1048
Tacoma, WA
98416-1048

³ Argon Geochronology
Laboratory,
Oregon State University,
Corvallis, OR
97331

⁴ Instituto de Geografía,
Universidad Nacional
Autónoma de México
Ciudad Universitaria
Del Coyoacán
cp 04510, México, D.F.

ABSTRACT

The map area includes the Tenalquot Prairie quadrangle and the northern two thirds of the Vail quadrangle in Washington's southern Puget Lowland. This map supports private and public resource management with insights into geologic deposits, structures, and hazards. Based on 59 new whole rock analyses, all igneous rocks in the map area are from the Northcraft Formation. Eight new radiometric ages between 45.8 ± 0.07 Ma and $<38.4 \pm 0.5$ Ma establish this unit as the oldest known expression of Cascade arc magmatism. These ages also indicate that Cascade volcanism overlapped the waning stages of Siletzia volcanism.

Preliminary analysis of aeromagnetic and gravity potential fields suggests that the Olympia geophysical lineament results from a normal fault and the Tacoma basin northeast of it contains a significant thickness of shallow igneous rocks that likely are Northcraft Formation. If both are true, then the Olympia fault has experienced no major northeast-down movement since the end of Northcraft Formation volcanism—which our age control suggests may be entirely middle Eocene in the map area.

Vashon glacial sediments, especially outwash, provide productive but easily polluted aquifers for private water wells and the cities of Yelm and Olympia. The extensive outwash gravel terraces in Tenalquot Prairie and the Deschutes River valley also host widespread, enigmatic Mima mounds. Lacustrine sand above outwash gravel and moraine deposits between Tenalquot Prairie and Lake Saint Clair suggest that large outwash channels were somehow later submerged by an ice-dammed lake with a shoreline at 400 ft elevation. Terminal moraines from the eastern (Yelm) and western (Olympia) ice lobes appear as hummocky glacial sediments east, north, and west of Tenalquot Prairie and along the hill front south of the Deschutes River, suggesting Vashon ice did not override Tenalquot Prairie. Heavily weathered pre-Vashon Drift extends miles farther south in this area but approximates the Vashon ice limit farther east and west. Bouldery outwash trains and denuded bedrock surfaces in the valleys of Johnson Creek and the Skookumchuck River document massive proglacial meltwater discharge south of all known ice limits.

INTRODUCTION

The map area includes the entire Tenalquot Prairie quadrangle and the northern two thirds of the Vail quadrangle. These quadrangles are located east of Olympia in the southeast Puget Lowland, between the Puget Sound and the hills of the Cascade Range. Principal land uses range from military training in the forests and prairies at Joint Base Lewis–McChord to urban and rural residences, forestry, and agriculture and industrial operations. Multiple quarries mine aggregate from glacial outwash within both quadrangles and volcanic bedrock in the hills of the Vail quadrangle. The glacial deposits in and near the map area are

the main source of water for the cities of Olympia, Lacey, Yelm, and surrounding areas (Thomas and others, 2007).

Previous geologic mapping campaigns were carried out mostly in the 1950s and 1960s (Bretz, 1913; Mundorff and others, 1955; Snively and others, 1951, 1958; Wallace and Molenaar, 1961; Noble and Wallace, 1966; Walters and Kimmel, 1968). While mapping and descriptions of glacial deposits and landforms by Bretz (1911, 1913) remain seminal in the project area, more recent projects have improved understanding of the thickness and distribution of Pleistocene units near the map area (Lea, 1984; Walsh and Logan, 2005; Logan and others, 2009;

Walsh and Pitre, 2013; Polenz and others, 2017, 2018, 2019). Others improved the characterization of aquifers in and near the map area (Mundorff and others, 1955; Wallace and Molenaar, 1961; Noble and Wallace, 1966; Walters and Kimmel, 1968; Drost and others, 1999; Walsh and others 2003a; Walsh and Pitre, 2013).

The 1:24,000 scale of this mapping project provides a previously unattained level of geologic detail for private and public land use decisions and aims to improve understanding of geologic hazards (earthquakes, landslides, floods) and resources (water, aggregate, other quarry rock). It offers a new perspective on the poorly understood Olympia structure and provides insights into rock types, their properties and ages, and the processes that formed the landscape—from Eocene volcanism that formed the hills in the Vail quadrangle to Pleistocene glacial scour and deposition that created striking landforms. These landforms include streamlined hills (drumlins) that reveal the direction of ice movement, chaotic hummocks that mark glacial moraines, eskers, and kettles where glacial ice stagnated and melted in place, and Mima mounds, whose origin remains enigmatic despite more than a century of study and popular fascination.

GEOLOGIC OVERVIEW

Bedrock

The hills in the southern part of the map area expose middle-to-late Eocene, subaerial, mostly andesitic volcanic and volcanoclastic rocks of the Northcraft Formation (Snively and others, 1951, 1958; Buckovic, 1979; Hagen, 1987; Schasse, 1987; Walsh and others, 1987; Phillips and others, 1989). Isolated, intrusive rock exposures have been locally mapped as Tertiary gabbro (Snively and others, 1958; Schasse, 1987) or Oligocene–Miocene gabbro (Walsh and others, 1987). All of these rocks are part of the ancestral western Cascade volcanic arc of Oregon and southern Washington (McBirney, 1978; Stanley and others, 1989). This relict arc is deeply eroded, broader than the modern Cascade volcanic arc, and centered farther west. West of the map area, and perhaps in the subsurface beneath it, Northcraft lavas and volcanoclastic rocks are flanked by Eocene sedimentary rocks of the marine McIntosh Formation and the deltaic to freshwater Skookumchuck Formation (Snively and others, 1951, 1958, 1959; Buckovic, 1979; Polenz and others, 2018, 2020; Sadowski and others, 2018, 2019). Detrital zircon spectra suggest that Northcraft Formation rocks provided a volcanic source for these Eocene sedimentary rocks and for the younger Eocene to Miocene sedimentary rocks of the Lincoln Creek, Astoria, and Wilkes Formations, which are widespread to the west and southwest outside of the map area (Snively and others, 1951, 1958; Buckovic, 1979; Polenz and others, 2018, 2020; Sadowski and others, 2018, 2019).

Unexposed crustal rocks in the subsurface of the map area also very likely include the early Eocene Crescent Formation basalt of the Siletzia terrane (Finn, 1990; Wells and others, 2014; Eddy and others, 2017), which accreted to North America during the early Eocene (Eddy and others, 2016, 2017) and appears to be underlain by ultramafic, relict mantle rocks (Finn, 1990).

Unlithified Glacial Deposits

Glacial till and outwash cover most of the map area with sediment derived from the Cascade Range, the San Juan Islands, and the Coast Ranges of British Columbia. Most of this drift documents an incursion of the northern-sourced Cordilleran ice sheet during the late Wisconsin Vashon stade (MIS2; Upham, 1904; Bretz, 1911; Lea, 1984; Walsh and others, 2003a,b; Walsh and Logan, 2005; Polenz and others, 2018, 2019), when the ice reached its southern terminus in and near the map area (Bretz, 1913; Mundorff and others, 1955; Snively and others, 1958; Noble and Wallace, 1966; Walters and Kimmel, 1968; Walsh and others, 2003, 2005). Polenz and others (2015) estimated that the Vashon glacial advance and retreat occurred between about 16 and 15.3 ka, thereby revising Porter and Swanson's (1998) earlier assessment of 16.95 to 16.75 ka. Older drift from at least one pre-Vashon incursion of Cordilleran ice drapes some of the hillsides around Johnson Creek and the north-facing hill front in the Vail quadrangle (Noble and Wallace, 1966; Schasse, 1987). Pleistocene glaciation of Mount Rainier and surrounding areas east of the map area (Crandell and Miller, 1974) additionally sent gravelly outwash from the Cascade Range west into the map area (Walsh and others, 2003a).

The most recent Cordilleran ice sheet split into two lobes within the map area, the Olympia lobe on the west and the Yelm lobe on the east (Bretz, 1913; Lea, 1984; Walsh and Logan, 2005; Logan and others, 2009; Polenz and others, 2018). The Yelm lobe dammed rivers that drained the Cascade Range, forming a series of glacially impounded lakes and diverting the runoff along the southeastern edge of the Puget Lowland. Radiocarbon dates show that the ice advanced gradually but collapsed quickly, perhaps in just a few years (at least in the Olympia lobe). The retreat caused at least one outburst flood across the map area (Pringle and Goldstein, 2002). This flooding and other ice-marginal drainage modified landforms and deposits into a complex system of geomorphic features and sediments that remain readily apparent in high-quality lidar images. The most vexing landforms are Mima mounds, which are widespread on Vashon glacial outwash in the map area but are not yet understood (Bretz, 1913; Washburn, 1988; Walsh and Logan, 2005; Logan and Walsh, 2009; Horwath Burnham and Johnson, 2012; Gabet and others, 2016).

Overview of Regional Structure

Throughout western Washington, northwest-trending bands of seismicity within the Cascade Range volcanic arc trend toward basin-bounding, northwest-striking, dextral oblique faults and east–west-striking reverse faults in the Puget Lowland (Gower and others, 1985; Brocher and others, 2001). Many, and maybe all of these faults are active, and as a group they accommodate ongoing crustal shortening and plate rotation in the Cascadia forearc (Wells and McCaffrey, 2013; McCaffrey and others, 2013; Wells and others, 2014). In the map area, the northwest orientation of the Olympia structure broadly fits this pattern. A clear understanding of what this structure is, and what hazards it may present, have remained elusive (Gower and others, 1985; Pratt and others, 1997; Brocher and others, 2001; Sherrod, 2001; Magsino and others, 2003; Van Wagoner and

others, 2002; Walsh and Logan, 2005; Blakely and others, 2009; Odum and others, 2016; Polenz and others, 2016).

The Olympia structure corresponds to a northeast-down gravity gradient first noted by Daneš and others (1965). It marks the southwestern edge of the Tacoma basin from the Olympic Mountains to the map area and coincides with a distinct aeromagnetic lineament. Northeast of the Olympia structure, sedimentary rocks and Pleistocene to Holocene, mostly glacial sediments fill the near surface of the Tacoma basin, which gradually deepens northward to an estimated depth of 5–7 km (Pratt and others, 1997; Brocher and others, 2001; van Wagoner and others, 2002). The north side of the Tacoma basin is flanked by the active Tacoma fault (Brocher and others, 2001; Nelson and others, 2008). Along the Olympia structure northwest of the map area, studies have identified: (1) post-glacial faulting on the northeast side of the geophysical lineament (Clement and others, 2010; Odum and others, 2016), (2) heavily disturbed Quaternary sediment on the southwest side (Polenz and others, 2016), and (3) evidence for Holocene subsidence in the southern Puget Lowland that may be related to the structure (Sherrod, 2001). However, no evidence for Quaternary tectonic deformation has to date been clearly connected to any large segment of the Olympia structure, and the subsurface geometry and kinematics of the structure as a whole remain poorly defined.

South of the Olympia structure, Snively and others (1958) show the northern ends of three, northwest-striking normal faults entering the map area in the southern half of the Vail quadrangle. These faults roughly parallel several mostly strike-slip to compressional faults and folds south and southwest of the map area (Snively and others, 1958; Schasse, 1987; Anderson and others, 2018, 2019; Lau and others, 2018; Polenz and others, 2018, 2019, 2020; Sadowski and others, 2018, 2019). The Crawford Mountain anticline of Snively and others (1951, 1958) penetrates the southwest corner of the map area.

Geologic Hazards

The poorly consolidated Quaternary sediments in the map area would amplify ground shaking during earthquakes, and the thicker package of less well-consolidated sediment filling the Tacoma basin, paired with steep basin edges, can both amplify and prolong shaking during an earthquake (see, for example, Wirth and others, 2019). Topical efforts of Palmer and others (1999, 2004) have placed some constraints on liquefaction hazards in some of these sediments.

Other active hazards in the map area include Mount Rainier-sourced debris flows and landslides along the steep walls of the Nisqually River valley (Scott and others, 1995). Landslides are also common among the volcanic rocks south of the Deschutes River.

METHODS

Geologic Mapping

We identified units from field observations in the Tenalquot Prairie quadrangle and northern two-thirds of the Vail quadrangle in the summer and fall of 2020. We collected field data and constructed preliminary field-based maps using Esri ArcMap. Most outcrops

were small, and many quite weathered, so measured features (bedding, joints, or shears) could not be traced beyond individual outcrops. We refined the field mapping through geochemical analyses, petrographic review of thin sections, $^{40}\text{Ar}/^{39}\text{Ar}$ and U/Pb age analyses, clast counts, geophysical data, analysis of well and boring records, geotechnical reports, prior geologic mapping and studies, aerial orthophotos, and geomorphic features identified from lidar. We used a lidar-based digital elevation model (DEM) with a 2-m grid resolution (Puget Sound Lidar consortium, 1999–2005, 2012; Pierce County, 2011, U.S. Geological Survey, 2016; Thurston County Geodata Center, 2011) to estimate site elevations and derive hillshade images, contours, and other products. Edge mismatches with the adjacent Nisqually and East Olympia quadrangles (Walsh and others, 2003a; Walsh and Logan, 2005) are intentional based on insights from our latest mapping. We used the geologic time scale of the United States Geological Survey (USGS) Geologic Names Committee (2010). Where that scale lacks Epoch subdivisions, we referred to Walker and Geissman (2009).

Geophysics

We collected 163 new gravity stations to construct a refined gravity map across areas of interest (for example, across the Olympia structure). In addition, we applied a horizontal gradient filter to the isostatic gravity grid and used an algorithm to select linear maxima (or “max spots”; Fig. M1A). Aeromagnetic data (Fig. M1) were compiled from Blakely and others (1999, 2020). Modeled isostatic gravity and aeromagnetic potential field profiles (using GM-SYS; Geosoft, Inc.) along line X–X’ (Fig. M1B) tested some of the qualitative interpretations of map-view data. Rock density and magnetic susceptibility measurements of 111 samples from 34 outcrops within and beyond the map area helped constrain these models. These geophysical data and analyses supplemented our interpretations.

DESCRIPTION OF MAP UNITS

Holocene to Pleistocene Nonglacial Deposits

- | | |
|----|--|
| af | Artificial fill (Holocene) —Cobbles, pebbles, sand, silt, clay, and boulders, all in various amounts, engineered and non-engineered; placed to raise roadbeds and other surfaces. Excludes small or shallow fills (less than 5 ft deep) such as most road-related deposits. |
| ml | Modified land (Holocene) —Locally derived soil, cobbles, pebbles, sand, silt, clay, and boulders, all in various amounts, reworked by excavation and (or) redistribution that modified topography; includes gravel pits and other developments. Excludes small or shallow reworking such as most residential site preparation and road-related modifications with excavations or deposits less than 5 ft deep or thick. |
| Qp | Peat (Holocene to Pleistocene) —Organic and organic-matter-rich mineral sediments (peat, gyttja, muck, silt, clay, and sand) in flat-bottomed depressions or other |

poorly drained flats; mostly mapped where lidar reveals such landforms and true-color or infrared aerial photos suggest hydrophilic vegetation and (or) wet conditions. Unit **Qp** is postglacial except possibly in four locations amid the hills south of the Skookumchuck River: three small troughs likely carved by pre-Vashon glaciation (Secs. 30 and 31, T16N R1E and Sec. 6, T15N R1E) and one landslide sag pond (Sec. 8, T15N R1E).

Qa, Qoa Alluvium (Holocene to Pleistocene)—Floodplain and channel sediments of pebbles, cobbles, boulders, sand, silt, clay, and peat, all in various amounts; gray to pale gray and brown to pale brown, weathers brown, orange, red, and yellow; generally fresh to mildly weathered but locally supplemented with proximally derived, weathered particles; loose; mostly well-rounded and moderately to well-sorted; north of the Deschutes River lithologically similar to northern-sourced glacial drift, and likely mostly reworked from there; south of the Deschutes River comprised of andesitic volcanic rocks derived from the Northcraft Formation, except where mixed with clasts of the above-mentioned drift in outwash corridors and downslope of the ice limit. In the Nisqually River valley, unit **Qa** includes Mount Rainier-derived debris flow diamictos, mud flow deposits, and lahar run-out deposits, such as those targeted by ¹⁴C ages GD1 and GD2 (Scott and others, 1995). The alluvium forms a highly permeable and productive, generally unconfined aquifer. These traits render the aquifer sensitive to pollution and the surface locally prone to drought. Although generally postglacial in age, unit **Qa** may locally include pre-Vashon deposits in the hills south of the Deschutes River; it is only mapped where alluvial transport appears to be active, however.

Unit **Qoa** identifies alluvium that no longer receives sediment. In tributaries of Johnson Creek (Vail quadrangle), landforms locally suggest that unit **Qoa** was deposited in response to tributary impoundment when glacial ice (or outwash?) filled Johnson Creek; unit **Qoa** in those tributaries therefore may include pre-Vashon outwash. Unit **Qoa** locally includes relict alluvial fans, such as 1,400 ft west of the confluence of Thompson Creek and the Nisqually River (N½ Sec. 11, T17N R1E).

Qaf Alluvial fan (Holocene to Pleistocene)—Pebbles, sand, silt, cobbles, and boulders, all in various amounts, deposited in broad, concentric lobes where confined channels spill out onto broader, less steeply sloping surfaces, and in glaciated parts of the map area commonly capped by dark brown to black, mucky loamy soils; gray to brown; loose; subangular to rounded; moderately to poorly sorted; stratified to unstratified. Unit **Qaf** was mostly mapped from fan-shaped landforms expressed in lidar. Alluvial fans tend to be subject to hazardous floods and debris flows, but in some locations the unit appears relict from periglacial conditions (and thus no longer subject to these hazards).

For example, at significant site S1 (Sec. 33, T7N, R1E), the alluvium appears to have been supplied by an ice-borne channel that also deposited an esker east of the alluvial fan. Most alluvial fans in the west half of the Tenaquot Prairie quadrangle probably began to form while residual Vashon ice was melting upslope, and for some of these fans, an absence of sharply incised upslope channels and (or) sizeable troughs from which sediments might have been sourced suggests that the fans have received no post-glacial sediment—for instance, at significant site S2 (Sec. 24, T17N R1W). In the west half of the Tenaquot Prairie quadrangle below about 400 ft elevation, relatively smooth landforms and nearby observations of glacial lake sands (roughly outlined by units **Qgos** and **Qgimos**; for instance at significant site S3: Sec. 8, T17N, R1E) further suggest that some relict fans are also draped with well-sorted glaciolacustrine sand or silt.

Qls

Landslide deposits (Holocene to Pleistocene)—Sand, silt, clay, pebbles, cobbles, and boulders, all in various amounts, derived from units upslope; weathering varied; particles angular to rounded; typically loose, unsorted, and jumbled; locally stratified in blocks; mostly mapped from landforms expressed in lidar (for example, hummocky slopes, deranged and disrupted drainages, disrupted or irregular slopes, tilted benches in hillsides, and concave upper and convex lower slope forms). Similar landforms are locally common but not necessarily indicative of landslides among Northcraft Formation volcanic rocks and in glacial deposits resting thereon, suggesting that we may have erroneously mapped some landslides in the Vail quadrangle and failed to map others. Our mapping of more than 120 landslides in the hills of the Vail quadrangle suggests that landslides are common there. In contrast, we mapped only two small landslides in the glaciated lowlands north of the Deschutes River; landslides along active cutbanks of the Nisqually River sometimes occur but none are mapped because their deposits have been removed by the river. Most landslides are located south of the Vashon ice limit, where some likely initiated before the Vashon stade.

Qmw

Colluvium (Holocene to Pleistocene)—Loose soil, rocks, sand, silt, and clay, all in various amounts, deposited by shallow raveling and soil creep; locally includes small landslides and alluvial fans, but fan-shaped deposits in unit **Qmw** are typically steeper than those in unit **Qaf**, and based on lidar images, commonly lack well-defined upslope feeder channels; shown where colluvium masks the underlying geology; mostly identified from landforms, and may locally include exposures of underlying deposits, especially where those are volcanic; unit not mapped on smooth slope surfaces where all pre-Vashon units tend to have clayey soils subject to some creep. All mapped instances of unit **Qmw** appear to be of post-glacial

age, but similar deposits that have gone unrecognized or proved too small to map may range to pre-Vashon age, especially south of the Vashon ice limit.

Pleistocene Glacial and Nonglacial Sediments

LATE PLEISTOCENE CONTINENTAL GLACIAL SEDIMENTS

The Puget lobe of the Cordilleran ice sheet advanced from the north and reached its southern terminus in the map area (Upham, 1904; Bretz, 1911) during the late Wisconsinan Vashon stade (marine oxygen isotope stage 2, MIS 2¹) and during one or more earlier glaciations (Lea, 1984; Walsh and Logan, 2005; Polenz and others, 2018, 2019). The map area straddles the southern terminus of the most far-reaching Cordilleran ice advances, which suggests that glaciers entered the map area only during the strongest global glaciations. This clearly includes the Vashon ice advance; for an estimate of when this ice advance reached the map area, we refer to the approximately 16 to 15.3 ka age range identified in the unit correlation diagram, and to Polenz and others' (2015) fig. 3 and discussion.

Weathering of pre-Vashon Drift varies widely but is generally more advanced than in Vashon Drift (Table DS5), consistent with varied weathering observed in pre-Vashon Drift west of the map area (Polenz and others, 2017, 2018, 2019). This may point to more than one pre-Vashon ice incursion. A strengthening of glacial maxima starting roughly 1 Ma (Pena and Goldstein, 2014) suggests that the pre-Vashon Drift(s) in the map area are <1 Ma old. Maximum depositional ages of pre-Vashon Drift samples west of the map area are consistent with this age range (between MIS6 and <1Ma)(Polenz and others, 2019).

Sediments from Cordilleran ice advances (hereafter "northern-sourced" drift) are sourced from plutons and metamorphic rocks in the north Cascades, the San Juan Islands, and the Coast Ranges of British Columbia, and porphyritic volcanic rocks from the Cascade Range (Polenz and others, 2019). These northern-sourced deposits can be identified by their rock and mineral constituents: granite with pink plagioclase, schist, gneiss, bright pink garnets, detrital epidote, granodiorite where abundant (Noble and Wallace, 1966), and, as noted by Walsh and Logan (2005), abundant polycrystalline quartz and a more diverse clast assemblage than anything sourced from the Cascade Range. Large quantities of hypersthene are distinctive of Mount Rainier provenance (Noble and Wallace, 1966).

¹MIS: global marine oxygen isotope stage curve, where even-numbered stages are used as a proxy for timing and intensity of global glacial periods (Morrison, 1991). For discussion of corresponding Cordilleran ice sheet advances into the Puget Lowland, see Booth and others (2004), Troost and Booth (2008), Polenz and others (2013, 2015), and Troost (2016). For timing of the MIS 2 ice advance into the map area at the southern limit of the Vashon glaciation, we refer to Polenz and others' (2015) fig. 3 and discussion, although the southern tip of their fig. 3 should have been extended south of Olympia to the Vashon ice limit south of the Deschutes River in the map area (and south of Scatter Creek farther west).

The Vashon-age Puget ice sheet was divided into a western (Olympia) and eastern (Yelm) lobe (Bretz, 1913; Noble and Wallace, 1966; Walsh and Logan, 2005). Clast counts from the map area are associated with the Yelm lobe. Their range of compositions closely resembles clast counts from the Olympia lobe—but still suggests a systematic difference. Seventeen clast counts of at least 50 clasts each ($n \geq 50$) and two partial counts ($n < 50$) from the Tenalquot Prairie and Vail quadrangles targeted deposits from the Vashon-aged Yelm lobe (10 counts, units Qgog, Qgim), pre-Vashon glacial deposits (4 counts, unit Qpd), and Cascade Range-sourced Nisqually River sediment (5 counts, units Qpc, Qoa, and Qa). The compositional ranges of the 17 full clast counts from the map area are reported in Table 1. Geochemical analyses of bedrock samples revealed that many rocks we field assessed as basalt are in fact andesite, suggesting that our clast count tallies also over-counted basalt and under-counted intermediate volcanic rocks. Consequently, compared to Olympia lobe tallies from west of the map area (Table 1), clast assemblages in the 17 "full" counts from the map area likely contain more intermediate and felsic igneous rocks at the expense of basalt. Only two of the 19 counts from the map area include sedimentary rocks (2%), and both are Vashon Drift. Whereas this is similar to Vashon-aged assemblages tallied west of the map area by Polenz and others (2018, 2019), it contrasts with some of their clast counts of pre-Vashon Drift, which revealed appreciable quantities of sedimentary rocks (0–28%).

Vashon Drift

Qgo **Recessional or proglacial outwash, undivided (late Pleistocene)**—Pebble gravel, locally ranges to cobble and boulder gravel; less commonly pebbly sand or sand; locally diamicton (unobserved but inferred—see last paragraph of this unit description); gray to pale gray, or mildly weathered to pale brown, brown, or variegated with iron stains; loose and commonly cohesionless; well-rounded to subrounded; moderately sorted to well-sorted and in gravel facies clast-supported, locally with matrix and interbeds of silt and sand; faintly bedded or structureless; lithologically diverse, with clast assemblages mostly from the Yelm ice lobe, except near the western map edge, where Olympia lobe clast assemblages locally prevail (See *Pleistocene Continental Glacial Sediments* above for corresponding lithologic percentages.)

Table 1. Clast composition ranges from 17 clast counts from the map area (Yelm lobe derivation) compared with clast counts from the Olympia lobe drift west of the map area (Polenz and others, 2018, 2019).

Lithology	Yelm lobe composition	Olympia lobe composition
Mafic igneous	28–84%	30–60%
Intermediate and felsic igneous	14–62%	15–35%
Quartz and chert	0–24%	5–25%
Metamorphic	0–14%	2–13%

Terrace risers (mostly in subunit Qgog) suggest that unit thickness may exceed 100 ft near the Deschutes River; Olympia city well records from the Lake Saint Clair area just north of the map area (well PW24 in Walsh and Pitre, 2013) suggest more than 400 ft of recessional outwash there.

Undivided unit Qgo is mapped where observations or map scale did not permit mapping of its textural or paleoenvironmental subunits. It is widely mapped along the Deschutes River valley but smaller patches can be found farther south along Mulqueen Road and in the valley of Johnson Creek, and scattered farther north across the Tenalquot Prairie quadrangle. Unit Qgo is of Vashon recessional age and stratigraphically overlies Vashon Till (including end moraines) and most ice-contact deposits. However, unit Qgo and its subunits Qgog and Qgos also include all proglacial Vashon outwash south of the Vashon ice limit, where the absence of glacial overriding prevented compaction of advance outwash (if any), and separation of advance and recessional outwash therefore becomes impractical (and inconsequential). Undivided unit Qgo likely mostly underlies its subunit Qgos and underlies all post-glacial units, except parts of Qoa (where that includes pre-Vashon sediment).

Unit Qgo and its subunits are laterally continuous with outwash units mapped west of the map area by Walsh and Logan (2005), who in their fig. 1 also outlined extension of their units into the Tenalquot Prairie and Vail quadrangles. Although Walsh and Logan's (2005) analysis provides great insight into the deglaciation of the map area, their outwash unit numbering would have led to inconsistencies in our map area. We relied instead on terrace riser symbols to illustrate cross-cutting relationships without numbering channels.

Outwash deposition near the ice margin was punctuated by high-discharge events. Walsh and Logan (2005) attribute 2–3 ft diameter boulders on the surface of their outwash unit Qgo_{y3} west of the map area to the andesite-rich, Mount Rainier-sourced Tanwax flood of Pringle and Goldstein (2002; see also Parker and others, 2008). This flood crossed the map area from east to west and deposited debris flow diamicton west of the map area (Pringle and Goldstein, 2002; Parker and others, 2008; Polenz and others, 2018; Pringle and Goldstein, Centralia College and Univ. of Puget Sound, respectively, written commun., 2018). Walsh and Logan's (2005) unit Qgo_{y3} is laterally continuous with outwash terraces in the map area, for instance in Sec. 12, T16N R1W, and although we did not specifically observe debris flow deposits or flood runoff deposits, it follows that both are part of the gravelly outwash in the map area.

Qgog **Recessional or proglacial outwash gravel (late Pleistocene)**—Loose pebbles, cobbles, and boulders, in various amounts, locally with sandy matrix and sand lenses or

interbeds; debris flow deposits (diamicton) unobserved but inferred in the map area from high discharge events such as the Tanwax flood (see undivided unit Qgo); tan to gray; variably sorted; mostly well rounded; lithologically diverse, with clast assemblages that we interpret as deposits mostly from the Yelm ice lobe, except near the western map edge, where outwash surfaces locally appear to have been fed by meltwater from the Olympia lobe (See *Pleistocene Continental Glacial Deposits* above for corresponding lithologic percentages.) Unit thickness is mostly unconstrained, but terrace risers in Tenalquot Prairie and along the Deschutes River valley suggest that it may exceed 100 ft. In the valleys of the Skookumchuck River and Johnson Creek, observed exposures of unit Qgog are mostly boulder gravel, consistent with the inference that large meltwater volumes flowed through these corridors when ice blocked all periglacial outwash pathways farther north (see also *Discussion*).

Qgos **Recessional or proglacial outwash sand (late Pleistocene)**—Sand and silt, locally pebbly or containing minor interbeds of pebble gravel; tan to brown; loose; clasts moderately to well-rounded; generally well sorted; sand and silt composition rich in polycrystalline quartz carried by Vashon ice; clast lithologies as described above for the Yelm and Olympia ice lobes (see *Pleistocene Continental Glacial Deposits*); varies in thickness from about 4 to 20 ft.

At least a few feet of unit Qgos is locally exposed amid more gravelly outwash terraces (unit Qgog) at the southern fringe of Tenalquot Prairie, suggesting patchy interludes of quiet water deposition on this part of the gravelly terraces. Unit Qgos in this area also locally onlaps pre-Vashon Till (unit Qpd). Unit Qgos forms an extensive blanket of sand in the north half of the Tenalquot Prairie quadrangle south of Lake Saint Clair and west of the terminal moraine extent indicated by units Qgim and Qgimos. In this area, unit Qgos is associated with smoother, more rounded landforms than would be typical of the common underlying units Qgim and Qgog, and unit Qgos was apparently deposited in an early glaciorecessional ice-dammed lake. This lake partly overlaps Lakes Nisqually and Russell (Bretz, 1913; Walsh and Logan, 2005), but appears to have reached a higher maximum lake surface around 400 ft elevation. Closed depressions within parts of

the former lake bottom, especially around Lake Saint Clair, suggest deposition while residual ice blocks resting amid outwash or till persisted underground. Several hundred feet of underlying, more gravelly recessional outwash in the Lake Saint Clair area suggests that the above-mentioned lake, and therefore most deposition of unit Qgos in the map area, mark the end of proglacial sedimentation in the map area.

Qgoi **Recessional ice-contact outwash (late Pleistocene)**—Sand and gravel deposited in ice-contact braid plains or channels; also sand or mixed sand and gravel in kettle walls, and sand or silt in kettle bottoms—commonly draped with a veneer of post-glacial peat where kettle bottoms are flat; tan to gray; loose; moderately to well-rounded and sorted; gently bedded in undisturbed channels or braid plains, but with bedding locally oversteepened and (or) chaotic and disrupted by kettle collapse. Stones, sand, and silt in the unit include northern-sourced clasts and sediment grains.

Qgim **End moraine (late Pleistocene)**—Pebbly to cobbly till, pebbles, sand, cobbles, silt, clay, and boulders, all in various amounts; gray, tan, and reddish brown; loose to compact; unbedded in till, unbedded to bedded in other facies. Topographic relief in a kettled part of the unit at the southern edge of Sec. 27, T17N R1E suggests at least 160 ft unit thickness. Most landforms within unit Qgim are strongly hummocky, commonly with kettles and eskers. Compared to units Qgic and Qgt, unit Qgim in most areas forms more hummocky surfaces and lacks drumlins and flutes. Lesser compaction in most exposures additionally separates it from unit Qgt. Boulders (glacial erratics) are common on the surface of unit Qgim. Many exposures at or near the ice limit, mainly in unit Qgim, are more weathered than is elsewhere typical of Vashon Drift. This suggests that older sediment was commonly reworked into Vashon deposits in this map area, and at least in exposures of unit Qgim south of the Deschutes River, there is commonly enough proximally reworked, older sediment to locally affect the character of the unit. Unit Qgim dropped out of melting, stagnant ice at the southwestern margin of the Yelm ice lobe and the southeastern margin of the Olympia ice lobe. The unit is locally supplemented or reworked by ice-contact outwash from meltwater that flowed or ponded along the ice front, which in the Vail quadrangle locally resulted in a kame terrace setting south of the Deschutes River, for instance at and near significant site S5, where slightly pebbly, moderately to well-sorted, loose sand contrasts with more compact nearby till. North of the Deschutes River, mainly on the northwestern fringe of Tenalquot Prairie, cross-cutting

relations between outwash terraces in unit Qgog, and the adjacent deposition of units Qgimo, Qgimos, and Qgoi, indicate that the Olympia lobe ice front had begun to disintegrate while meltwater from the Yelm lobe continued to construct units Qgog, Qgimo, Qgimos, and Qgoi west of the Yelm lobe. As a result, nearly all surficial drift in the map area consists of sediment from the Yelm lobe, with Olympia lobe sediment mostly limited to subsurface deposits (mainly in unit Qgim, but also in units Qgt, Qgic, and Qga).

Qgimo **End moraine draped with outwash (late Pleistocene)**—Glacial outwash pebbles, sand, cobbles, and boulders, all in various amounts, resting on an end moraine consisting of pebbly to cobbly till, pebbles, sand, cobbles, silt, clay, and boulders, all in various amounts; gray, tan, and reddish brown; loose in outwash, loose to compact in moraine; moderately to well-sorted in outwash, unsorted in till; unbedded to bedded in outwash, unbedded in till. Thickness is mostly unknown, but we suspect that surficial outwash is mostly less than 10 ft thick whereas kettle relief locally implies more than 100 ft total unit thickness in parts of Sec. 30, T17N R1E. Unit Qgimo is distinguished from unit Qgim by systematic presence of surficial outwash deposited in ice-contact channel surfaces that are now heavily fragmented by kettles. The kettles in unit Qgimo are more pervasive than those in unit Qgoi. Like unit Qgim, the underlying moraine dropped out of melting, stagnant ice at the southern ice margin. In Sec. 25, T17N R1W, the unit transitions westward into outwash draped over flutes and drumlins that suggest transition to a substrate of lodgment till or scoured, older deposits.

Qgimos **End moraine draped with glaciolacustrine outwash sand (late Pleistocene)**—Glacial outwash sand, locally ranging to pebbly sand or silt, resting on an end moraine that consists of pebbly to cobbly till, pebbles, sand, cobbles, silt, clay, and boulders, all in various amounts; gray, tan, and reddish brown; loose in outwash, loose to compact in moraine; moderately to well-sorted in outwash, unsorted in till; unbedded to bedded in outwash, unbedded in till. Thickness is mostly unknown, but we suspect that surficial outwash is mostly less than 10 ft thick whereas kettle relief locally implies more than 100 ft total unit thickness in Secs. 18 and 19, T17N R1E. Unit Qgimos is distinguished from unit Qgim by systematic presence in unit Qgimos of smoothed landforms that suggest a surficial drape of lacustrine sand that also covers apparent lake-bottom surfaces adjacent farther north and west (unit Qgos). The kettles in unit Qgimos are more pervasive than those in

unit Qgoj. Like units Qgim and Qgimo, the underlying moraine dropped out of melting, stagnant ice at the southern ice margin.

Qge **Esker (late Pleistocene)**—Pebbles and sand; medium gray; lightly to moderately weathered; mostly loose; clasts well-rounded; well-sorted; distinctly channel-bedded in most exposures, with beds commonly oversteepened because source water, confined beneath ice, locally flowed uphill, or because bedding was deformed when englacial and supraglacial deposits sank to the ground during ice melt. Unit Qge was deposited by subglacial, englacial, and supraglacial meltwater and is found amid or adjacent to units Qgic and Qgim. Unit Qge is clearly marked by distinctive sinuous hill landforms—and in most locations was mapped on their account.

Qgic **Ice contact deposits (late Pleistocene)**—Undivided till and outwash, consisting of loose to compact diamicton, pebble gravel (locally cobbly) and sand; pale gray to brown and reddish brown; mildly weathered; mostly loose and crumbly in ablation till and outwash, ranging to compact in lodgment till, but typically lacking thick, continuous, or widespread deposits of lodgment till at the ground surface, though small till exposures and detrital till fragments are common; particle sizes range from cobbles to medium sand, with finer particles common in till matrix and boulders locally in till and outwash; varied rounding and sorting; northern sourced, mostly from the Yelm ice lobe. Unit thickness is highly varied; much of the unit is likely less than 10 ft thick, but relief in Sec. 35, T17N R1E locally suggests more than 80 ft. Unit Qgic is marked by irregular landforms that document sediment deposition and meltwater scour beneath, in, or on stagnant ice, such as kettles, eskers, and rounded channels that commonly connect to eskers, and drumlin and flute surfaces that are usually fainter and less regular than those in unit Qgt but still record some ice movement.

Qgt **Lodgment till (late Pleistocene)**—Diamicton containing boulders, smaller rocks, and sand, with an unsorted or poorly sorted matrix comprised of sand to clay-sized particles, in various amounts; matrix supported in nearly all exposures; gray to pale reddish brown; mildly to moderately weathered; mostly compact to very compact, acts as aquitard, not usually penetrated by roots; clasts well rounded to faceted or angular, and commonly striated, matrix mostly angular; thickness in map area mostly unknown and likely to pinch out locally; thickness commonly varies across short distances (<100 ft), with the thickest observed exposure in the map area revealing a 6 ft minimum thickness (along the east edge of Sec. 22, T16N R1E) and some exposures of well-developed lodgment till measuring less than 1 ft thick (for instance, at significant site S6, Sec. 11, T17N R1E); unsorted and nearly everywhere

matrix supported; unbedded but in some exposures flow banded (resembling bedding); inferred to be northern sourced from the Yelm ice lobe, but west of Tenalquot Prairie inferred to be sourced from the Olympia ice lobe. Unit Qgt is deposited directly by glacial ice and usually includes a loose, surficial cover of 2–10 ft of ablation till and (or) outwash clay, silt, sand, and gravel. That cover appears to be the main parent material for the post-glacial soil, whereas the underlying lodgment till tends to be mostly unweathered. Till in unit Qgt is in most exposures more compact and resists root penetration and water percolation more effectively than unit Qgic. Compared to unit Qgic, unit Qgt tends to be accompanied by better-developed flutes and drumlins and fewer landforms whose preservation would signal stagnant ice (subglacial meltwater channel scour, kettles, eskers). Landforms were used to help delineate unit boundaries between units Qgic and unit Qgt. Unit Qgt overlies unit Qga and older deposits.

Qga **Advance outwash (late Pleistocene)**—Fluvial pebble gravel, cobble gravel, boulder gravel, sand, and lacustrine sand, silt, and clay, inferred in various amounts but mostly observed as gravel in sparsely scattered exposures and well records; gray to light brown; compact, but in well-rounded, well-sorted gravel or sand commonly lacking cohesion and therefore resembling loose recessional outwash; mostly moderately or well-rounded; mostly northern-sourced but locally with abundant Cascade Range-sourced particles, especially along and near the Deschutes valley, where drainage from the Cascade Range was confined between hillsides and the advancing ice; sand, silt, and clay consisting of mostly plutonic, polycrystalline quartz, and minor metamorphic grains. Unit Qga is distinguished from recessional outwash by compaction of unit Qga from overriding ice and stratigraphic position of unit Qga beneath Vashon Till (unit Qgt). Unit Qga may include pre-Vashon fluvial sediment (of units Qpd and Qpc) where similarity of deposits precludes differentiation of these units.

Pre-Vashon Drift

Qpd **Pre-Vashon, northern-sourced glacial sediment, undivided (Pleistocene)**—Pre-Vashon glacial till, pebbles, cobbles, sand, silt, clay, and boulders, all in various amounts; light brown or gray to yellowish-brown, orange, red, or reddish brown; loose or too weathered to preserve evidence of former compaction; where not fully weathered to clay, unit includes mostly mafic igneous and intermediate to felsic volcanic clasts, but clast assemblages in four full counts and one partial count (C11, C16, C17, C19, and small sample count C15) proved highly varied, with all ten clasts in C15 field identified as mafic igneous and the other three counts looking profoundly different from each other. Sand and smaller particles in a thin section from clast count site C16 (Sec. 25, T16N R1W) include

mostly clay, 3–5 percent broken plagioclase, and 1–2 percent black oxides and trace amounts of quartz. Unit Qpd includes direct ice deposits (till) and outwash, locally in close association (in moraine, stagnant ice, or kame deposits). We observed unit Qpd near the southern end of Tenalquot Prairie, in the hills along both sides of Johnson Creek, and on the north-facing slopes south of the Deschutes River, where many exposures were too small and patchy to be mapped. Unit Qpd is queried at well site W8 near the south end of Tenalquot Prairie (Sec. 7, T16N R1E) because the driller's log reported more than 200 ft of sandstone below 8 ft well depth—suggesting that what the log reported as “sandy clay” in the top 8 ft might have developed from sandstone. Nearby exposures of unit Qpd were mostly clay at the surface, whereas a resident reported an absence of mud cracking throughout his property at and near well W8. However, the “sandy clay” from the driller's log and the resident's report of “gravelly” soil may be consistent with Noble and Wallace's (1966) mapping of pre-Vashon Drift. We mapped all pre-Vashon, northern-sourced glacial deposits as undivided drift because distinctions between outwash and till are mostly no longer viable due to weathering. Varied weathering of clasts in clast counts C11, C15, C16, C17, and C19 is consistent with suggestions west of the map area of multiple pre-Vashon ice incursions during the past 1 million years (see *Pleistocene Continental Glacial Sediments*).

OTHER PRE-VASHON SEDIMENTS

Qpc Pre-Vashon alluvium from the Cascade Range, undivided (late Pleistocene)—Pebbles, cobbles, sand, silt, clay, peat, boulders, and diamicton; lithologically dominated by volcanolithic clasts of Mount Rainier or other Cascade Range sources; pale gray to light brown and reddish brown; compact. Sand fraction petrographic point counts on two samples (n=50 each) revealed 27–58 percent perthitic K-feldspar, 20–25 percent plagioclase, 20–46 percent iron oxides and lithics, 15–30 percent quartz, 15–20 percent black opaques, and 10–13 percent femic minerals. We observed unit Qpc only along the sidewalls of the Nisqually River valley near the northeastern map corner. A systematic down-section increase in weathering was suggested by general field impressions and clast counts C4 (collocated with luminescence site GD3, 155 ft above river level), C2 (50 ft above river level), and C3 (modern alluvium). Clast count C1 is the lowest in elevation and seemingly lowest in section. Anomalously, this clast count suggested weathering comparable to modern channel alluvium collected nearby (C3). However, large (lag?) boulders (up to 8 ft in diameter) observed by Walsh and others (2003a) at river level near C1 are deeply weathered (chisel end of rock hammer penetrates at least several inches deep). Some of the deeply weathered boulders are glacially striated, suggesting that they may be Cascade Range-sourced

alpine drift, and Walsh and others (2003a) suggested possible correlation to the alpine Hayden Creek Drift (Crandell and Miller, 1974; Walsh and others, 1987) or the alpine Wingate Hill Drift (Crandell, 1963; Walsh and others, 1987). A luminescence age estimate (GD3) from the upper, western valley wall about 155 ft above river level suggests a mid-to-late MIS 3 age at that site. That age, in turn, suggests a potential for downvalley stratigraphic correlation to Mount St. Helens C tephra on Anderson Island north of the Nisqually River's marine delta (Walsh and others, 2003b; Lesemann and others, 2013).

Eocene Volcanic and Sedimentary Rocks

NORTHCRAFT FORMATION VOLCANIC ROCKS (MIDDLE TO LATE EOCENE)

Ev_n Undivided igneous rocks (middle to late Eocene)—Mostly dark gray to medium gray lavas with rare dikes, mostly andesite and basaltic andesite, but ranging from basalt to basaltic trachyandesite and trachyandesite (all grouped into subunit Ev_{an} where that is separately mapped); interbedded with volcanic ash and light brown to tan and olive pyroclastics, flow breccia, lahar deposits, and other volcanoclastics (subunit Ev_{cn}); may locally include dacite and rhyolite (subunit Ev_{dn}) (see *Geochemistry*), lapilli ash, and andesitic block-and-ash flow tuffs (subunit Ev_{vn}); locally with intrusions (subunit Eig_n). Undivided unit Ev_n is mapped where subunits could not be separated out. Eight new Northcraft Formation radiometric ages from the map area range from 45.8 ± 0.07 Ma to <38.4 ± 0.05 Ma (Table 2; Appendices B and C, Tables DS2, DS3A–G) and are further discussed below (see *Discussion*). This age range applies fully to units Ev_{an}, Ev_{cn}, and Ev_{vn}. It is less clear if the chemically distinct unit Ev_{dn} shares the same age range and if unit Eig_n was shorter-lived.

Ev_{an} Andesite and basaltic andesite flows (middle to late Eocene)—Lava flows of mainly andesite and basaltic andesite, and less commonly trachyandesite, basaltic trachyandesite, and basalt (see *Geochemistry*); locally includes interbedded volcanoclastic rocks (unit Ev_{cn}) and vent breccia (unit Ev_{vn}); dark olive gray to dark gray and medium gray, weathers variously orange-brown, brown, and gray; greenish tint in many exposures due to pale-green glass; locally pervasively red-coated along joints and partings (observed only at the Bald Hill quarry, geochemistry sites G38 and G39, Sec. 3, T15N R1E); matrix mostly very fine crystals (generally <0.25 mm) to glassy or aphanitic; phenocrysts in porphyritic flows mostly <5 mm; tabular and blocky, or platy jointed, locally brecciated. Rocks in most outcrops throughout the map area

Table 2. New Northcraft Formation radiometric ages from the map area. See appendices and data supplement for full results and sample details.

Sample	Age type	Map unit	Age
GD4	Detrital zircon maximum constraining age on tuffaceous sediment.	Evc _n	<38.4 ±0.5 Ma
GD5	⁴⁰ Ar/ ³⁹ Ar plagioclase plateau age on basalt.	Eva _n	42.62 ±0.12 Ma
GD6	⁴⁰ Ar/ ³⁹ Ar groundmass mini-plateau age on basalt.	Eva _n	43.59 ±0.12 Ma
GD7	⁴⁰ Ar/ ³⁹ Ar groundmass mini-plateau age on andesite.	Eva _n	43.51 ±0.08 Ma
GD8	⁴⁰ Ar/ ³⁹ Ar groundmass mini-plateau age on andesite.	Eva _n	43.63 ±0.08 Ma
GD9	⁴⁰ Ar/ ³⁹ Ar groundmass mini-plateau age on andesite.	Eva _n	44.08 ±0.08 Ma
GD10	⁴⁰ Ar/ ³⁹ Ar groundmass total fusion age on basaltic andesite.	Eva _n	45.80 ±0.07 Ma
GD11	⁴⁰ Ar/ ³⁹ Ar stacked age from two groundmass mini-plateau ages on gabbro	Eig _n	38.68 ±0.13 Ma

are weathered and break with a dull thud, but the fresher rock interiors tend to splinter. Less weathered andesitic flow rocks, such as at geochemistry site G27 on Baumgard Hill (Sec. 33, T16N R1E) tend to break conchoidally, with razor-sharp edges. Petrographic analysis reveals that the iron-rich minerals in unit Eva_n are mostly pyroxene and magnetite and rarely olivine, mostly in the groundmass but also in trace quantities as phenocrysts up to 0.5 mm. Alteration of olivine to transparent, reddish iddingsite is common. In andesitic and trachytic rocks, some very fine-grained, iron-rich minerals form laminar bands. Plagioclase is the predominant phenocryst phase in all porphyritic flows, with pyroxene being much more subordinate. Felsic groundmass constituents in unit Eva_n are crypto-crystalline to glassy. The more silicic compositions are more prone to breaking into shards or splinters. The cryptocrystalline to glassy groundmass in unit Eva_n indicates that the unit was mostly subaerially erupted, although some of the rock may be hypabyssal. Local features of note within the unit include: (1) An unusually coarse-grained porphyritic basalt at geochemistry site G10 along Johnson Creek (collocated with age sites GD 5 and 6, Sec. 30, T16N R1E) contains megacrysts of plagioclase up to 1.5 cm across, although most plagioclase in this rock is less than 5 mm; (2) A steeply east-dipping dike was observed with enclosing autoclastic lava breccias in the western limb of Crawford Mountain anticline, 0.56 mi northeast of Skookumchuck Reservoir (Sec. 18, T15N R1E); (3) Outcrop-scale transitions from tabular and blocky or platy jointed

to brecciated flow are locally exposed, for instance, in road cuts along Mulqueen Gap (Sec. 12, T15N, R01E). Such brecciation probably resulted from syndepositional, local changes in gas content, where loss of volatiles caused the lava to thoroughly fragment; (4) Along the southern section of Johnson Creek Road, lava flows display tabular and concentric jointing, and in one instance, an agglutinous mass at the bottom of an open semi-arcuate jointed lava flow reveals a lava tube (Sec. 6, T15N, R01E).

Evc_n **Volcanic ash and volcanoclastic deposits (middle to late Eocene)**—Andesitic volcanic ash, crystal lithic vitric lapilli-ash, block-and-ash flow tuffs, and lahars; locally includes interbedded andesite lava flows; light brown to tan to olive, with hackly weathering; groundmass earthy in luster and devitrified, with rare glass shards; lithic fragments typically subangular to angular, with broken crystals (<2 mm); moderately to poorly sorted. Unit Evc_n varies within tens of feet from unwelded, with samples breaking around the surfaces of embedded clasts, to sufficiently welded for sample surfaces to break embedded clasts and for road builders to require blasting. The unit includes poorly sorted, unwelded lapilli-ash tuff with large, non-juvenile lapilli, blocks of mostly andesitic compositions (see *Geochemistry*), and, locally, lahar deposits with unsorted, rounded clasts of all sizes. Geochemical analyses of whole-rock samples and clasts yielded virtually all andesitic compositions (see *Geochemistry*).

Unit Evc_n is widely exposed in the hills south of the Deschutes River. The upper

part of unit Evc_n is typically unwelded. The lower part of Evc_n contains both unwelded outcrops and partially welded rocks, often in close proximity. Descriptions are consistent with both hot lahars and ash-flow tuffs at different locations. Both groundmass and blocks are andesitic (for example, geochemistry samples G18 and G19, respectively, Sec. 31, T16N R1E) and can be interpreted as the pyroclastic facies of andesitic stratovolcanoes that experienced sporadic, late-stage(?), small-volume, silicic dome building as recorded by unit Evd_n. Exposures of unit Evc_n are mostly capped by andesitic lava flows on the upland surface between Miller and Baumgard Hills. These flows comprise a discontinuous cover from that surface southwest to the ridge top along Cross Section A–A', where the distribution of ridge-top lavas closely corresponds to aeromagnetic highs in Fig. M1A. The volcanoclastic rocks of unit Evc_n appear to generally rest on mostly andesitic to basaltic andesitic lavas widely exposed along the main valleys (Skookumchuck and Deschutes Rivers, Johnson Creek, and Mulqueen gap).

Evvn **Volcanic vent breccia (middle to late Eocene)**—Intermingled lapilli-ash tuff, block-and-ash tuff, bomb tuff (agglutinate), agglomerate, and agglutinous spatter of intermediate to silicic composition; dark colored, usually reddish-brown and commonly partly or completely weathered to clay, particularly north of Baumgard Hill. At geochemistry site G30–G31 on the western border of the map area (Sec. 1, T15N R1W), the breccia consists of angular blocks and large lapilli of black, porphyritic lava and dark gray, very finely crystalline to aphanitic vesicular lava clasts in a reddish brown matrix. Minor compositional variability between lava and agglutinate spatter at a single site is common; at Bald Hill (sec. 3, T15N, R01E), the lava is andesite (G38) while the vent breccia is trachyandesite (G39). The difference in total alkali content of less than one percent may, in this instance, be attributed to heightened secondary alteration of the more-porous breccia, which contain zeolites, an alkali-rich mineral group. Unit Evvn identifies eruptive vents that sourced lavas of basaltic-andesitic, andesitic, and trachyandesitic to trachydacitic composition.

Evd(n) **Dacite to rhyolite flows (middle to late Eocene)**—Lava flows of dacite to rhyolite; dark lavender gray and light tan, weathers

medium gray and yellowish tan; platy to blocky. Dull white, elongate feldspar phenocrysts 1–5 mm in length comprise up to 5 percent of the rock, surrounded by light-colored groundmass with an earthy luster; sparse black pyroxene crystals 1–2 mm in length comprise less than 1 percent of the rock. Mineralogic banding parallel to platy jointing is particularly pronounced at and near geochemistry site G16 (west of Baumgard Hill, Sec. 32, T16N R1E). The banding is attributed to layering of darker colored microcrystalline iron oxides, including pale red, lavender, and black varieties, and, as seen under the microscope, parallel alignment of plagioclase microlites.

Exposures of unit Evd_n west of Johnson Creek (geochemistry sites G20, G22, G25, and G26, Sec. 36, T15N R1W) are not accompanied by associated pyroclastic material.

Within the Vail quadrangle, these limited outcrops may represent late-stage(?), small-volume, silicic Northcraft Formation domes in a mostly andesitic stratovolcano complex.

Eign **Gabbro (middle to late Eocene)**—Medium–dark gray salt-and-pepper intrusive igneous rock; dense; coarsely crystalline; massive and relatively unjointed; based on petrography, comprised of about 75 percent plagioclase crystals that are usually less than 3 mm but range from less than 0.5 to 5 mm, also includes 20 percent pyroxene (<3 mm), 7 percent magnetite (<0.5 mm), and trace amounts of hornblende (<3 mm). Secondary zeolite coatings up to 2 mm thick form multi-centimeter-scale rosettes on rare partings. No glass was observed. The texture is intergranular (interlocking). Individual pyroxene crystals tend to be smaller than plagioclase crystals and tend to cluster in glomerocrystic groups near the larger plagioclase crystals. Fractures are rare to absent, so the rock breaks across crystal boundaries. On a TAS diagram, samples plot as andesite, but unit Eign is mapped as gabbro because it is intrusive and its pyroxene content greatly exceeds its hornblende content. This is consistent with mapping by Snavely and others (1958), who cited a mostly calcic feldspar (labradorite) content in support of their gabbroic classification. The crystal size of the gabbro suggests shallow intrusion, perhaps at a depth of roughly 1 km.

Unit Eign was observed only in and immediately around the Columbia Granite quarry above Skookumchuck Reservoir

along the southern edge of the map area (Secs. 11 and 14, T15N R1E). A new, approximately 38.7 Ma $^{40}\text{Ar}/^{39}\text{Ar}$ age on gabbro from the quarry (GD11; Tables 2, C1, and DS3G; Fig. C7) indicates that unit E_{gn} at this quarry is younger than Northcraft Formation exposures farther north in the map area. However, this age is consistent with Northcraft Formation exposures upsection of the quarry (see also discussion of *Intrusive Rocks* below), and Northcraft Formation ages farther south in the Washington Cascades (WGS unpublished $^{40}\text{Ar}/^{39}\text{Ar}$ ages, samples CB19-111rB, CB19-210r, CB20-T091, CB20-W064, CB20-W080).

Unit E_{gn} is queried in Cross Section A–A' because at that location the unit was not observed but was inferred to account for a northwest-elongate potential field anomaly (RI in Fig. M1a) measured in gravity and magnetic data. The anomaly suggests a reversely magnetized subsurface rock body that is consistent with the density and magnetic susceptibility of this unit. The northwest-elongate orientation of the intrusion is consistent with northeastward extension implied by our inference of northwest-striking normal faults farther northeast in the map area.

SEDIMENTARY ROCKS

Ensk **Skookumchuck Formation (middle to late Eocene) (cross-section only)**—Terrestrial to deltaic and shallow marine feldspatholithic sandstone and siltstone with coal beds. The unit is inferred based on Snively and others (1951, 1958), who indicate that it includes their "Upper Thompson" coal bed beneath this part of the Skookumchuck River valley and forms the northeastern limb of their Thompson Creek syncline, the axis of which they show at the southwestern end of our Cross Section A–A'. Along the unnamed, inferred fault across the unit, Snively and others (1958) reported that bedding dips southeast at up to 60 degrees in the hills just southeast of the Skookumchuck River valley. Unlike Snively and others, this map shows unit Ensk interfingering with Northcraft Formation, based on Polenz and others (2020). This unit encompasses a large, Eocene delta complex that ranges from terrestrial Skookumchuck Formation beds to laterally adjacent, coeval, deep-marine McIntosh Formation, both of which received much of their sediment from erosion of contemporaneous Northcraft Formation volcanism. New Northcraft Formation radiometric ages presented in this map (GD4 to GD11) are consistent with that contemporaneity, and the age range shown for the Skookumchuck Formation in the correlation diagram therefore includes a lower bounding 47.35 ± 0.21 Ma

age from the McIntosh Formation (Polenz and others, 2017).

DISCUSSION

Eocene Bedrock

The volcanic rocks in the map area are flanked to the west and southwest by Eocene sedimentary rocks mapped by Snively and others (1951, 1958) as the McIntosh and Skookumchuck Formations. Whereas Snively and others mapped the McIntosh Formation as mostly marine and older than Northcraft Formation and the Skookumchuck Formation as mostly terrestrial to marine-deltaic and younger than Northcraft Formation, Polenz and others (2020) concluded that the two sedimentary formations are generally coeval and interfingering as part of a large Eocene marine delta system, such as envisioned by Buckovic (1979) and Sadowski and others (2018).

Age control data suggest that Northcraft Formation volcanism spanned most of the time of deposition of the Eocene marine-deltaic sedimentary rocks west and southwest of the map area. Northcraft Formation volcanism had commenced in the map area by 45.8 ± 0.07 Ma (age site GD10, Table 2; Appendix Table C1 and Fig. C4; Table DS3D; see also *Whole Rock Geochemistry*) and continued in the map area through at least about 38 Ma, based on seven other ages from the map area (GD4–GD9, GD11; Table 2, Appendices B, C, and Tables DS2, DS3A–G), although a nearly 4 million year age gap separates the youngest two Northcraft Formation ages (GD4 and GD11) from the rest (GD5 to GD10). That gap is filled by unpublished $^{40}\text{Ar}/^{39}\text{Ar}$ ages from Northcraft Formation in the Cowlitz River basin about 8–30 miles south to southeast of the map area (A. Steely, written comm., Washington Geological Survey, 2021). Together, these ages indicate that Northcraft Formation volcanism was active across a wide swath of the southwest Washington Cascades for much (or all?) of the time of the Eocene delta deposition farther west. It is likely that the Northcraft Formation was a major sediment source for the McIntosh-Skookumchuck Eocene delta system throughout much or all of its deposition, an inference that is also consistent with abundant Eocene ages among the detrital zircon spectra from this Eocene delta.

REASSIGNMENT OF INTRUSIVE ROCKS AT THE "COLUMBIA GRANITE" QUARRY TO THE NORTHCRAFT FORMATION

This mapping reassigns intrusive rocks previously mapped as Tertiary gabbro (Snively and others, 1951, 1958; Schasse, 1987) or Oligocene–Miocene gabbro (Walsh and others, 1987) to the Northcraft Formation (unit E_{gn}). This reassignment rests on field relations, Northcraft-compatible geochemical composition (see *Whole Rock Geochemistry*), and new radiometric age control at the "Columbia Granite" quarry (Secs. 11 and 14, T15N R1E.).

Field relations indicate that the gabbro at the Columbia Granite quarry is older than the overlying volcanic and volcanoclastic rocks. Along the north face of the quarry, the base of a lava flow immediately atop the gabbro includes gabbro clasts that closely resemble the unconformably underlying gabbro (Fig. 1). Both here, and more distinctly farther east along the access road to the quarry, overlying lava flows (unit E_{va}) are exposed in

knife-edge contact atop the gabbro. The inclusion in the lava of gabbro clasts that resemble the underlying gabbro body suggests that the gabbro had been intruded and unroofed, and was being eroded prior to deposition of the upsection lava. Farther west at geochemistry site G50, we interpret several feet of orange and dark purplish gray, clayey material as paleosol weathered 2–4 ft into the underlying gabbro (Fig. 2). This suggests that the exhumed surface of the gabbro was locally exposed to surface weathering long enough to develop a substantial soil profile.

Geochemical traits of the gabbro (G51, G55), lava upsection of the gabbro (G54, unit Evc_N), and tuff extracted from volcaniclastic deposits at G50 above the gabbro (unit Evc_N; Fig. 2) suggest that all samples are Northcraft Formation (see *Whole Rock Geochemistry*).

The age of the gabbro at the Columbia Granite quarry is consistent with inclusion in the Northcraft Formation. A ⁴⁰Ar/³⁹Ar age from the gabbro establishes an approximately 38.68 ± 0.13 Ma age of intrusion (GD11, *Appendix C; Table DS3G*). That age is bracketed between older Northcraft Formation lavas elsewhere in the map area (GD5 to GD10) and younger Northcraft Formation volcaniclastic sediment (unit Evc_N) sampled directly above the gabbro. Detrital U/Pb analysis of zircons from a roughly 9 in.-thick tuffaceous clay layer, which rests on an apparent paleosol weathered into the gabbro, yielded a <38.4 ± 0.5 Ma age for deposition of the tuffaceous sediment (GD4) (Fig. 2). GD4 is reported as a maximum constraining age because the assemblage is detrital and the reported age is from the youngest single zircon in the sample. However, 50 of the 92 zircons together form a single, strong peak at the young end of the zircon age spectrum (Fig. B1C). The dominance of this peak at the young end of the zircon age spectrum suggests that the 38.4 ± 0.5 Ma age of the youngest zircon is close to the age of extrusion of tuff that was then reworked into the sampled sediment. The <38.4 ± 0.5 Ma age from the upsection tuffaceous sediment (GD4) is within error of the 38.68 ± 0.13 Ma age of the gabbro (GD11) and unpublished

Northcraft Formation ages farther south in the Washington Cascades (⁴⁰Ar/³⁹Ar ages: A. Steely, Washington Geological Survey, written comm., 2021). All available age control data are therefore consistent with Northcraft Formation association of both the gabbro (unit Eign) and the overlying tuffaceous sediment (unit Evc_N) and lava (unit Evc_N).

Taken together, the field relations, geochemical analyses, and ages described above indicate that the top of the gabbro was erosionally exhumed and locally exposed to surface weathering prior to deposition of overlying lavas (G54) and tuffaceous sediment (G50); they require the age of the gabbro to be revised to an Eocene age within error of other Northcraft Formation ages, including one directly upsection, and they justify inclusion of the gabbro and overlying volcanic and volcaniclastic deposits in the Northcraft Formation.

LATE PLEISTOCENE CONTINENTAL GLACIAL SEDIMENTS

Proglacial outwash in the map area, especially south of the ice limit, documents high-volume, high-energy meltwater flow. Well-rounded boulder gravel terraces and isolated larger boulders in the valleys of Johnson Creek (referred to as Stony Point channel by Bretz, 1913, and Walsh and Logan, 2005) and the Skookumchuck River document high-energy discharge routed through these valleys during the glacial maximum, when ice blocked all drainage pathways farther north (Bretz, 1913; Lea, 1984; Walsh and Logan, 2005). The gabbro lithology of some outwash boulders (see photo on cover) downstream of the Columbia quarry (from which the gabbro is derived) strongly suggests that high-energy discharges also entered the Skookumchuck River valley via the more elevated, narrow Mulqueen gap that is upstream of the Columbia quarry. Neither Bretz (1913) nor Lea (1984) nor we found outwash in Mulqueen gap. We agree with Lea (1984) that the narrowness of Mulqueen gap may have limited outwash deposition, and we suggest that large landslides in Mulqueen

gap and the Skookumchuck River valley upstream of Skookumchuck Reservoir led to postglacial valley floor aggradation that now obscures any outwash gravel. Relatively abundant, denuded bedrock cliffs in all three valleys (Mulqueen gap, Skookumchuck, and Johnson Creek) also support the inference of high-volume discharges.

The outwash terraces in the southwestern quarter of the



Figure 1. Gabbro inclusions in Northcraft lava flow. Ovoid forms around hammer are gabbro clast inclusions in the basal few ft of andesitic Northcraft Formation lava (unit Evc_N) along the northern high-wall of the Columbia Granite Quarry (Sec. 11, T15N, R01E). The gabbro clasts closely resemble, and appear to be detritus derived from, unit Eign, which unconformably underlies the lava along a knife-edge contact just below the exposed outcrop.

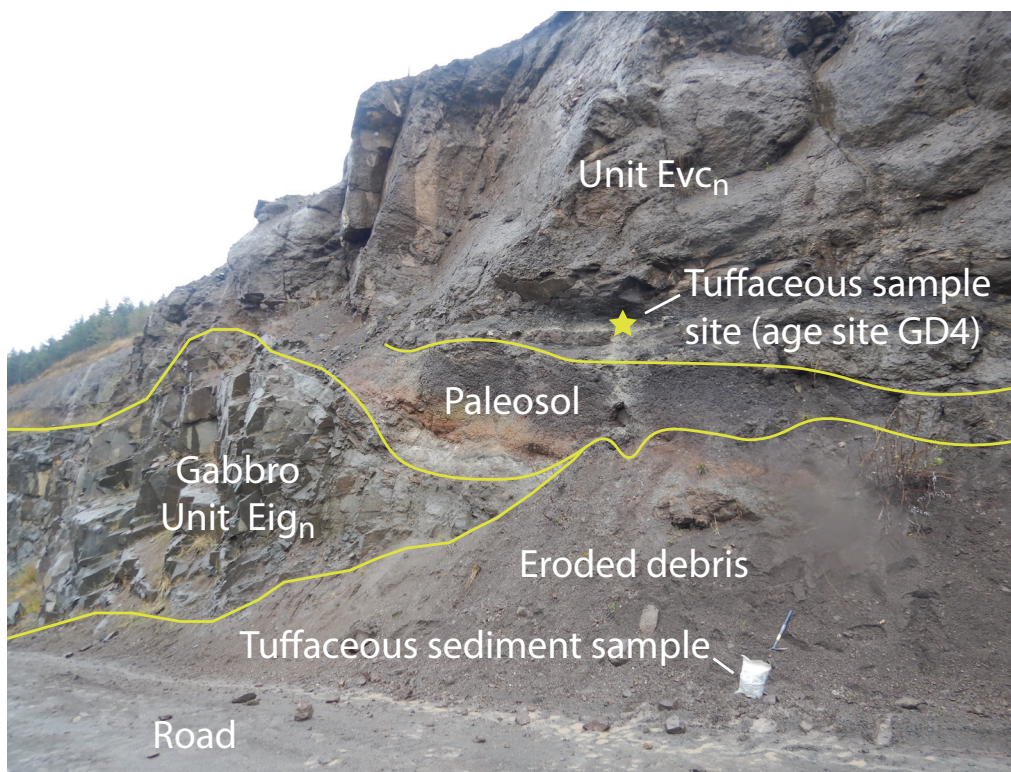


Figure 2. Northern highwall of the Columbia Granite Quarry, Sec. 11, T15N R01E. Detrital U/Pb sample site with gabbro from the Columbia Granite quarry in lower left (unit Eig_n), capped by a paleosol (orange and dark purplish gray in center of image). U/Pb sample site GD4, collocated with geochemistry site G50, is marked by the thin, horizontal pale yellow layer across the upper center of the image. The upper half of the image shows pyroclastics of unit Evc_n.

Tenalquot Prairie quadrangle occupy an ice-free ‘interlobe terrain’ between the Olympia and Yelm lobes at the southern margin of the Vashon-age Cordilleran ice sheet (Bretz, 1913; Noble and Wallace, 1966; Walsh and Logan, 2005). Unit Qgim (flanking unit Qgog at Tenalquot Prairie from the east, west, and north), documents the terminal positions of the Olympia and Yelm lobe ice fronts at the end of the Vashon ice advance into the map area. Although these ice fronts may have shifted earlier during the ice incursion, several points suggest that Tenalquot Prairie remained ice free throughout the Vashon ice incursion:

1. The terraces of unit Qgog at Tenalquot Prairie were fed by channels that abruptly emerge amid an adjacent moraine, and the terraces reach elevations similar to the highest parts of the moraine; only ice could have supplied meltwater to these elevations. This supports the presence of ice to the east and west during deposition of the outwash terraces.
2. A paucity of kettles amid unit Qgog at Tenalquot Prairie suggests that the prairie remained ice-free because adjacent melt-out deposits from stagnant ice are invariably heavily kettled.
3. Pre-Vashon Drift is exposed near the south end of Tenalquot Prairie (Sec. 8, T16N R1E). These strongly weathered and soft, clayey sediments would likely have been scraped off or buried by a Vashon ice advance.
4. Vashon sediment south of Tenalquot Prairie is either outwash (and therefore not directly ice-deposited), or questionable and sparse.
5. The apparent Vashon ice limit (maximum ice elevation) along the north-facing mountain front south of the Skookumchuck River is much lower south of Tenalquot

Prairie than it is farther east (Bretz, 1913; Lea, 1984; this study) or west (Bretz, 1913; Lea, 1984; Walsh and Logan, 2005; Polenz and others, 2018). This suggests that Vashon ice may have never advanced south across Tenalquot Prairie (consistent with the Vashon ice limit line in fig. 1 of Walsh and Logan, 2005).

6. Pre-Vashon ice south of Tenalquot Prairie appears to have advanced to about 3 miles south of the Deschutes River, where no Vashon ice deposits have been documented. The local divergence of maximum ice extents suggests that Vashon and pre-Vashon ice advances encountered somewhat different paleogeographic conditions en route south across the Puget Lowland.

Several features in the map area illustrate the progression of events during deglaciation at the southern ice margin. The largest, most elevated outwash terrace at Tenalquot Prairie is elevated above (and therefore older than) all those identified west of the map area by Walsh and Logan (2005). This is consistent with the above inference that Tenalquot Prairie formed an ice-free interlobe terrain while ice covered areas farther east and west. West-flowing meltwater from the Yelm ice lobe later beheaded the northern end of the most elevated terraces while constructing lower terraces mostly in Secs. 28–30, T17N R1E. These cross-cutting relations indicate that earlier drainage to the southwest was sandwiched between the Yelm ice lobe on the east and the Olympia lobe on the west, whereas later, west-northwest-directed drainage was no longer confined by Olympia lobe ice to the northwest. This implies that the Yelm lobe ice margin remained stable while the south end of the Olympia lobe had begun to disintegrate.

The distribution and character of map units in and near the interlobe terrain help illustrate the progression from early,

southbound meltwater flow to later, northwest-bound flow fed by Yelm lobe ice into an ice-dammed lake that covered much or all of the northwestern quarter of the Tenalquot Prairie quadrangle. The elevated, early outwash terraces that document southwest-flowing meltwater in the interlobe terrain are largely free of kettles, suggesting that the outwash was deposited on ice-free ground. In contrast, outwash terraces farther west are kettled. Their deposition therefore involved burial of ice, and since the meltwater came from the same source area as that which deposited the kettle-free interlobe terrain outwash, it seems unlikely that these kettles resulted from ice swept up by the meltwater; more likely, the meltwater carved channel surfaces into the wasting Olympia lobe ice front while depositing outwash partly atop residual ice. The more ice persisted beneath the outwash, the more kettles developed—which points to the main distinction between the moderately kettled unit Qgoi and pervasively kettled units Qgim and Qgimo. In unit Qgoi, outwash surfaces are largely intact and conceal the underlying moraine. In units Qgim and Qgimo, outwash surfaces are barely recognizable and so heavily disrupted by kettle collapse that the unit commonly reveals exposures of the underlying end moraine deposits.

The transition from deposition of the elevated early unit Qgog terraces to the heavily kettled units Qgim and Qgimo coincides with a shift from south-flowing meltwater to initially southwest-flowing meltwater, and eventually, northwest-flowing drainage. The uppermost half mile of the youngest, west- to northwest-sloping terraces is carved into the most elevated western fringe of the Yelm lobe moraine (unit Qgim) east of clast count site C6 (ec. 28, T17N R1E). The source of the water at the eastern end of the channels lies in a part of the Yelm lobe moraine that is systematically about 20–50 ft lower in elevation than the western edge of the moraine, suggesting that the Yelm lobe either retreated and re-advanced in this area, or retreated in steps. Either way, the Yelm lobe remained more elevated and seemingly more intact than the Olympia lobe, because meltwater from the Yelm lobe cut into and deposited outwash amid the Olympia lobe moraine, thereby appreciably modifying both the topography and the character of the surficial deposits in the Olympia lobe moraine.

An apparent lake delta at about 400 ft elevation at the northwest end of Tenalquot Prairie (significant site S4, Sec. 19, T17N R1E) marks a transition to moraine covered with lake sediment. Below the 400 ft delta top elevation, the chaotic end moraine landforms are slightly smoothed and rounded by a surficial drape of lacustrine sand in unit Qgimos. North of unit Qgimos (and therefore north of the Olympia lobe end moraine), sand-covered lowland surfaces of unit Qgos continue to suggest a lake bottom surface between about 200 and 270 ft elevation. This suggests that the Olympia lobe had not only stopped advancing at its southern tip, but had more generally stalled and begun to melt into ice-marginal lakes and meltwater streams. Yet the lowland surface of unit Qgos presents an enigma (previously hinted at by Walsh and Logan, 2005). The deeply kettled outwash around Lake Saint Clair across the northern map edge indicates several hundred feet of recessional outwash deposition in that area (Walsh and Pitre, 2013). East, south, and west of Lake Saint Clair, broad, flat surfaces appear to be part of large channels that

slope gently to the west, thus adding evidence that voluminous recessional meltwater flows formed the lowland surfaces beneath unit Qgos in the northwestern part of the Tenalquot Prairie quadrangle. (These channels are well-marked in fig. 1 of Walsh and Logan, 2005, as pathways Qgon2, Qgon3, Qgon4 and farther north as Qgos.) How such large, recessional outwash channels at lower elevations were formed prior to ice-dammed lake inundation to 400 ft remains unexplained.

WHOLE ROCK GEOCHEMISTRY

Whole rock chemical compositions were determined for 59 igneous samples (Tables DS3A, B), all interpreted to be from the Northcraft Formation. Based primarily on petrography and field relations, these samples are divided into gabbros (n=2), mafic to intermediate lavas (n=44), felsic lavas (n=5), tuffs (n=6), and vent facies lavas (n=2). However, aside from the expected elemental differences that accompany variation in silica content, the samples exhibit geochemical similarities that warrant their classification as a single formation.

The samples range from basalt to rhyolite (51.2–70.3 wt. % SiO₂; 5.3–0.5 wt. % MgO) but the majority (>80%) classify as basaltic andesite or andesite (Fig. 3). The suite is bimodal, with dacite and rhyolite being separated from the other lavas by a ~6 wt. % SiO₂ gap. Tuffs are distinguished by low Na₂O and CaO, and high Loss on Ignition (LOI), likely resulting from alteration, but gabbro, vent facies rocks, and mafic to intermediate lavas overlap in composition (Fig. 3). All samples classify as subalkaline (Fig. 3) and most plot as calc-alkaline on an AFM diagram (Fig. 4) or SiO₂-K₂O diagrams, but as tholeiitic on an FeO/MgO-SiO₂ diagram (Fig. 5). The contrasting classifications provided by Figures B and C suggest the Northcraft Formation is transitional between tholeiitic and calc-alkaline. In general, concentrations of compatible elements (for example, MgO, Sr, Cr) are lower, and those of incompatible elements (for example, K₂O, Rb, Ba, Hf) are higher in the felsic lavas. All samples are moderately light rare earth element-enriched (average (La/Yb)_N = 6.9).

Calc-alkaline affinities, a broad range of SiO₂ contents, high field strength element (Ta, Nb) depletions on a mid-ocean ridge basalt (MORB)-normalized spidergram (Fig. 6), and elevated Ba/Nb (average = 16) are diagnostic traits of subduction-related magmatism and indicate that the Northcraft Formation is an early expression of the Cascade arc. The earliest Northcraft age obtained in this study (45.80 ± 0.07 Ma on TPVm021) is within error of the 45.97 ± 0.23 Ma age obtained on an isolated basalt exposure ~25 miles to the west in the Littlerock quadrangle (Polenz and others, 2017). However, the two samples are significantly different in composition (Table 3), with the Littlerock basalt having traits of Siletzia lavas. Based on these chemical and age data, the onset of Cascade arc magmatism overlapped in time with the waning stages of Siletzia volcanism.

DESCRIPTION OF STRUCTURES

The six northwest-striking faults and two fault-parallel folds shown on this map are tentatively inferred (and all queried), primarily to accommodate constraints revealed by two south-west–north-east-oriented 2D models of gravity and magnetic

TAS (Le Bas and others, 1986)

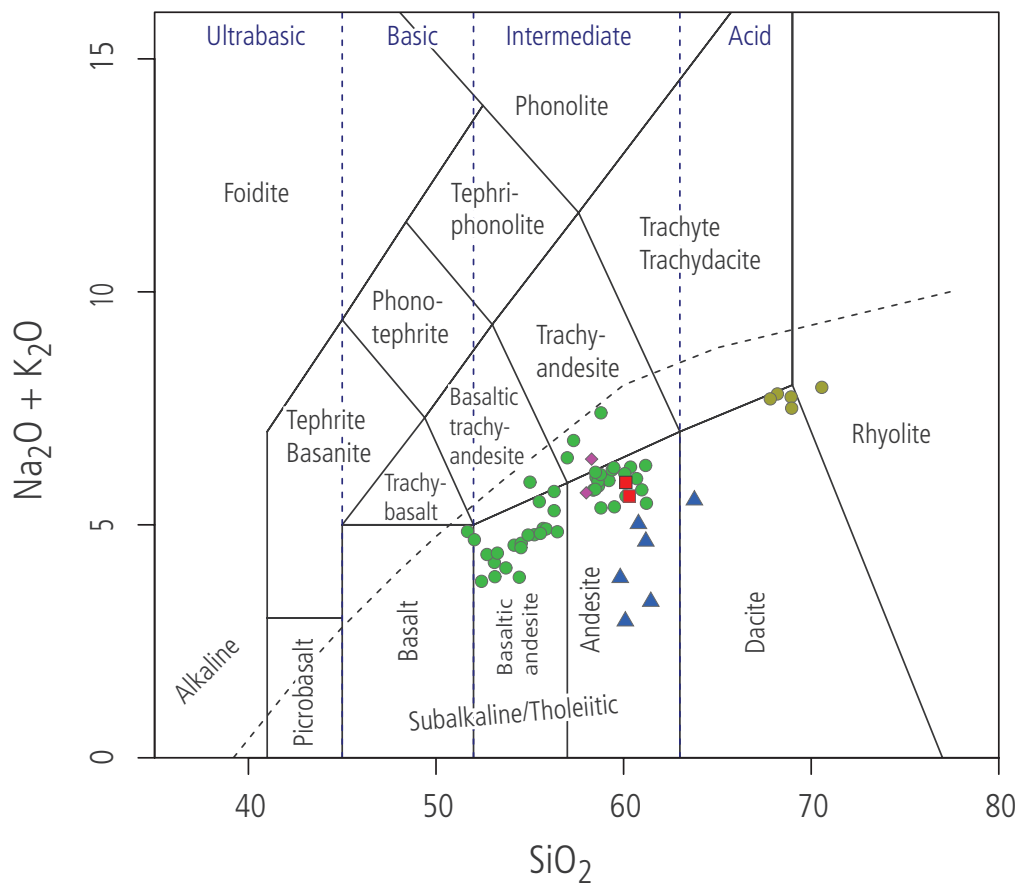


Figure 3. Total alkalis versus silica plot (Le Bas and others, 1986) showing that Northcraft samples are sub-alkaline and predominantly basaltic andesites and andesites. Note also the compositional gap that separates most lavas from the dacites and rhyolites. Rock types are gabbro (red squares), mafic to intermediate lavas (green circles), felsic lavas (yellow circles), tuffs (blue triangles), and vent facies lavas (purple diamonds).

AFM plot (Irvine and Baragar, 1971)

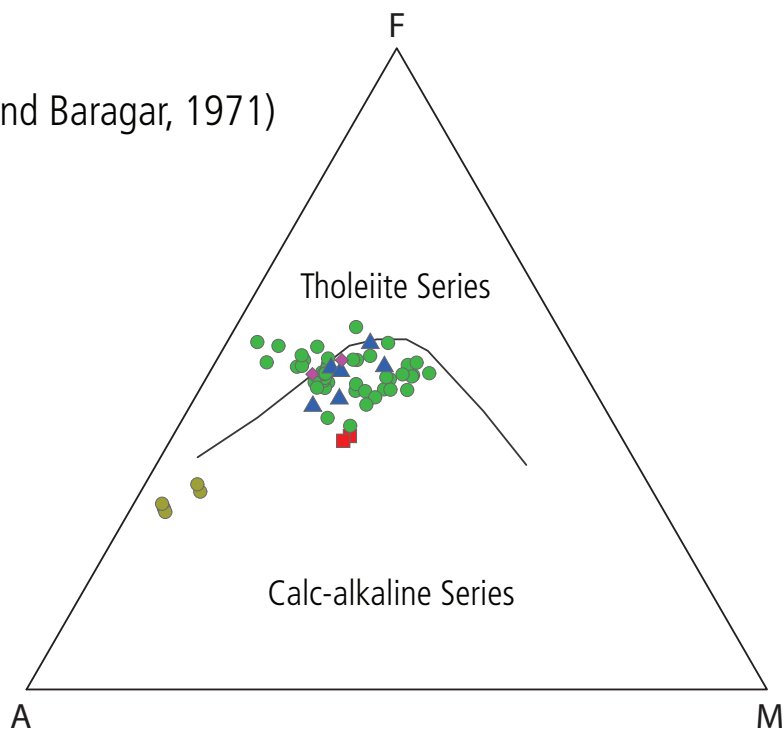


Figure 4. AFM diagram (Irvine and Baragar, 1971) showing that the majority of Northcraft samples classify as calc-alkaline by this method. Symbols are the same as in Figure 3.

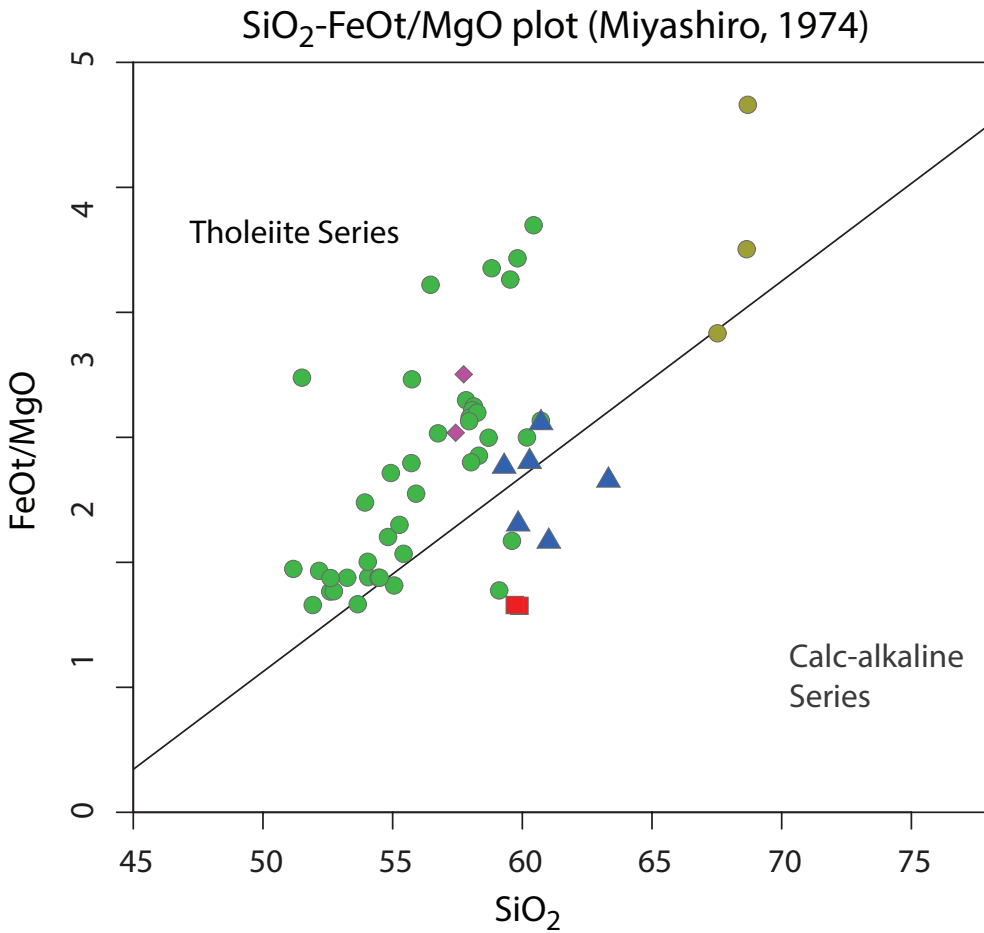


Figure 5. SiO₂-FeO/MgO plot (Miyashiro, 1974) indicating that by this classification method most Northcraft samples are tholeiitic. Symbols are the same as in Figure 3.

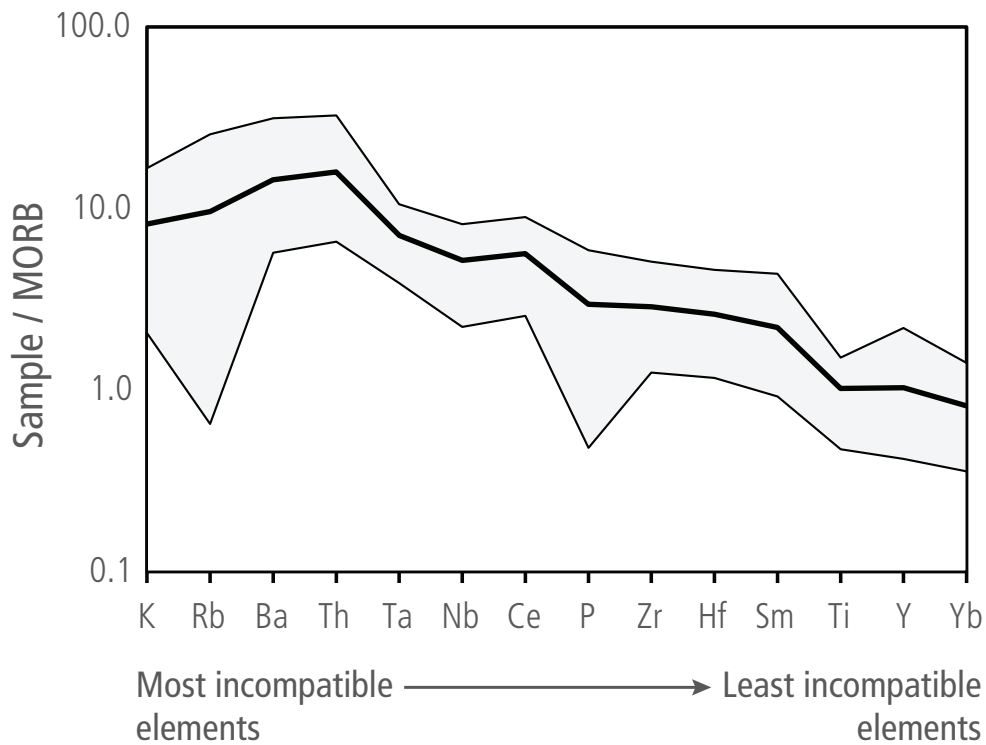


Figure 6. MORB-normalized spider diagram showing K-Rb-Ba-Th enrichments and Ta-Nb depletions characteristic of subduction-related magmas. Shaded region outlines the range for all 59 Northcraft samples. The thick black line in the center marks the mean values for all samples. Depletions in P and Ti reflect fractionation of apatite and ilmenite in some samples. Depletion in Rb is likely an alteration effect. Data normalized to MORB values of Sun and McDonough (1989).

Table 3. Comparison of chemical traits of rock from Littlerock quadrangle unit Evb (Polenz and others, 2017) lava versus Northcraft Formation (this study).

	SiO ₂ (wt. %)	K ₂ O (wt. %)	Ba (ppm)	Rb (ppm)	(La/Yb) _N	Ba/Nb
Littlerock unit Evb	48.8–51.6	0.06–0.23	17–61	1.0–1.8	1.4–3.2	2.3–5.1
Northcraft (averages)	58.0	1.23	287	19.3	6.8	16.3

potential-field anomalies near Cross Section A–A'. One of these modeling profiles is shown in Fig. M1B.

The westernmost fault is adapted from Snively and others (1951, 1958), who appear to have mapped it at least partly based on coal mining-related observations south of the map area. Our potential-field modeling, particularly the gravity modeling at feature WF in Fig. M1A, shows a clear, northeast-up boundary along the fault, and we therefore follow Snively and others (1951, 1958) in showing a fault. Whereas Snively and others (1958) nearby cross section B–B' shows a southwest-dipping normal fault, the steepness of the associated gravity gradient fits better with a more vertical geometry. The fault is flanked on the northeast by the fault-parallel Crawford Mountain anticline, which we extended southeast across the map area because it helps explain the distribution of observed field exposures of volcanic rocks on the northern side of the Skookumchuck River valley. This anticline and several more approximately fault-parallel folds that Snively and others (1958) mapped southwest of the map area imply a corrugated fold pattern that favors northeast–southwest compression across the fault. We therefore coded the fault as high angle rather than normal, but our evidence seems less than compelling. It is consistent with a transpressive setting suggested by several more northwest-striking faults (and ongoing plate motions) southwest of our map area (Snively and others, 1958; Polenz and others, 2018, 2019, 2020; Sadowski and others, 2018, 2019; Anderson and others, 2019). In addition to supporting the anticline, the potential-fields map and modeling also reveal a fault-parallel intrusion of igneous rock northeast of the fault, which favors northeast–southwest extension across the fault at the time of intrusion (see also discussion below; unit E_{ign} in Cross Section A–A'; magnetic low labeled RI in Fig. M1A). This could be evidence that this fault was active at a different time than the normal faults farther northeast in the map area.

The remaining five faults farther northeast in the map area, though roughly parallel to the first fault, are all shown as normal with northeast-down offset. We speculate that the northeast–southwest extension accommodated by all these faults is related to Eocene(?) development of the Tacoma basin, bounded principally by a northeast-down, normal Olympia fault, which has a steep and high-amplitude gravity gradient (OF in Fig. M1A). We infer that the Olympia fault is a normal fault with a northeastern main strand (the northeasternmost fault shown on the map and on Cross Section A–A') and two smaller strands farther southwest (all labeled as Olympia fault). The geophysical data could support vertical or reverse offset for these faults (OSS in Fig. M1A), but a simpler fault structure at depth results from normal faults. Regardless of dip, we are confident that the Olympia structure is a fault because all attempts to model the potential-fields without fault-bounded east-side-down displacements failed. It is less clear if the two faults at the center

of Cross Section A–A' (CF in Fig. M1A) are also part of the same larger structure, but their similar orientation and sense of offset suggests that they developed in response to the same stress field. These two faults are inferred because our potential-field mapping suggests their presence, the modeling suggests offset magnitude, and they help us balance unit thicknesses across the west half of Cross Section A–A'. We show all five faults as inferred or concealed because we observed no evidence for surface rupture. We show the two southwestern strands of the Olympia fault as terminating about 1.3 miles northwest of Cross Section A–A' due to low gravity data density in this area. This effectively eliminates the ability to detect the very small amplitude gradient changes that revealed fault displacement along our model profile line, where gravity measurements were spaced at only 820 ft (250 m) intervals. We also show the southwesternmost of the three strands terminating about a mile southeast of Cross Section A–A' because our southernmost model line suggests only two strands slightly farther southeast (Fig. M1B).

Simultaneous modeling of gravity and magnetic potential fields (Fig. M1B) indicates that moderately dense, strongly magnetic igneous rocks exist in the shallow subsurface of the Tacoma Basin in and near the map area (interpreted as unit E_{va} in Cross Section A–A'; TBV in Fig. M1A). These igneous rocks appear to greatly thicken to several thousand feet in the Tacoma basin northeast of the Olympia fault and seemingly overlie several thousand feet of less magnetic sedimentary or volcanoclastic rocks (below the base of Cross Section A–A') that in turn overlie dense, strongly magnetic basement rocks (below the base of Cross Section A–A'). The potential-fields models permit only about 1,000–2,000 ft of sediment or volcanoclastic rock accumulation above the thick, magnetic volcanic rocks of unit E_{va} in Cross Section A–A'. In addition, introducing a step offset at the location of the Olympia fault on the top of the magnetic volcanics would produce a strong mismatch with the aeromagnetic anomaly. We know of no post-Northcraft Formation volcanism in or sufficiently near the map area to fill this part of the Tacoma basin with such a thickness of volcanic rocks, and we therefore tentatively assign the shallow igneous rocks to Northcraft Formation andesitic lavas, which, based on our tests of rock density and magnetic susceptibility, fit the rock properties of our best-fit model. If correct, this assignment implies that (1) the Olympia fault contributed to forming this part of the Tacoma Basin during and (or) before deposition of the Northcraft Formation—which in this map area has so far yielded only Eocene-age data, and (2) substantial east-down offset along the Olympia fault ended no later than deposition of the Northcraft Formation.

The northeast–southwest extensional character of the Olympia fault is also consistent with the stress field suggested by a 4-mile-long by 1-mile-wide, fault-parallel intrusion that we

propose based on a magnetic high across the eastern map edge immediately east of the Olympia fault (OFI in Fig. M1A). Our modeling is consistent with such a narrow intrusion consisting of rocks with properties similar to andesite at depths below 2,500 ft below msl (below the base of Cross Section A–A'). A similarly oriented magnetic low (and compatible gravity patterns) along the above-mentioned compressive fault across the southwest corner of the map (Fig. M1) is best fit by a magnetically reversed intrusion with a density and magnetic susceptibility similar to gabbro. That intrusion is therefore tentatively shown as unit E_{ign} in Cross Section A–A'.

SUGGESTIONS FOR FURTHER STUDY

- The dacitic member of the Northcraft Formation (unit Ev_{dn}) lacks radiometric ages. One or more ages from this unit could ascertain if the dacitic volcanism was coeval with the other Northcraft Formation volcanism in and near the map area.
- Multiple well records around the southern end of Tenalquot Prairie (including W1 and W8) report sandstone in the shallow subsurface. Opportunistic monitoring of new excavations and borings, and collection and analysis of sedimentary rock samples from such operations could identify whether this sandstone is part of the Eocene marine delta deposits (Snively and others, 1958) or the Miocene Mashel Formation. The identity and age of the unit holds implications for the timing of northeast-down displacement on the Olympia fault (with regional significance for assessment of geologic hazards).
- What is the distribution of Mima mounds in the map area, how did Mima mounds form in the map area, especially where mounds don't rest on flat gravel surfaces, and how does their distribution within the map area (and beyond) relate to underlying geologic units?
- The abundant kettles in the map area, especially within unit Q_{gim}, likely offer a rare opportunity to better constrain (probably by coring and ¹⁴C dating of peat) the time of the Vashon glacial maximum and onset of recession. Improved assessment of the timing of the Vashon glacial maximum and onset of glacial recession directly affects calculations of post-glacial fault activity levels throughout the Puget Lowland.
- In the northwestern quarter of the Tenalquot Prairie quadrangle, the apparent record of meltwater flows and ice-dammed lake landforms and sediments presents a riddle (see *Late Pleistocene Continental Glacial Sediments*). Detailed mapping of lake deposits, the extent and thickness of recessional outwash beneath the lake sediment, and the distribution of till and older, compact sediments beneath the recessional lacustrine and fluvial sediment may be needed both within and beyond the map area to resolve the paradox of broad, gravel-floored recessional outwash at a low elevation covered with recessional lake sands to a much higher elevation (significant site S4 suggests about 400 ft).
- The Vashon ice limit in the map area is generally clear, but it could benefit from additional, detailed mapping west and

north of the northern end of Johnson Creek valley, where unit Q_{gim} is queried, west thereof in the Bucoda quadrangle, and along the north-facing hillslope in the eastern third of the map area. Additional study of pre-Vashon Drift is also needed to quantify the age(s) and number of pre-Vashon incursions of Cordilleran ice into the map area.

ACKNOWLEDGMENTS

We thank: Kevin Hansen (Thurston County) and Chris Pitre (Coho Consulting) for assistance with selected water well data and hydrogeologic insights; Tim Walsh, Pat Pringle, and Josh Logan (all WGS retired) for fielding questions about prior mapping and other issues; all WGS active staff for their suggestions, edits and guidance; Weyerhaeuser, Port Blakely Tree Farms, Joint Base Lewis–McChord, and countless other landowners for land access, local knowledge, historical context, well records, and other information.

Author roles

Field work, overall geological interpretations, and write-up: Michael Polenz and Frank Hladky; Geochemical interpretation: Jeffrey Tepper; Gravity data collection: Megan Anderson and Alex Dolcimascolo; Potential fields modeling: Megan Anderson and Alison Horst; ⁴⁰Ar/³⁹Ar age analyses: Daniel P. Miggins; Landsat data analysis: Gabriel Legorreta Paulín; GIS: Michael Polenz.

REFERENCES

- Anderson, Megan; Lau, Todd; von Dassow, Wesley; Reedy, Tabor; Sadowski, Andrew; Horst, Alison; Lockett, Alex; Becerra, Rebeca; Toth, Conner; Steely, Alex; Polenz, Michael, 2019, The Doty fault: What is its place in modern crustal deformation of southwest Washington? [abstract]: American Geophysical Union Fall Meeting, Abstract T33D-0404.
- Anderson, Megan; Lau, Todd; von Dassow, Wes; Reedy, Tabor; Staisch, Lydia; Cakir, Recep; Sadowski, Andrew; Polenz, Michael; Becerra, Rebeca; Toth, Conner; Steely, Alex; Walsh, Tim; Norman, Dave; Sherrod, Brian, 2018, The Doty fault network: 3D regional deformation applied to seismic hazard characterization in the forearc of Washington State [abstract]: American Geophysical Union Fall Meeting, Abstract T13I-0356.
- Auclair, Marie; Lamothe, M.; Huot, S., 2003, Measurement of anomalous fading for feldspar IRSL using SAR: Radiation Measurements, v. 37, no. 4–5, p. 487–492. [https://doi.org/10.1016/S1350-4487(03)00018-0]
- Black, L. P.; Kamo, S. L.; Allen, C. M.; Davis, D. W.; Aleinikoff, J. N.; Valley, J. W.; Mundil, Roland; Campbell, I. H.; Korsch, R. J.; Williams, I. S.; Foudoulis, Chris, 2004, Improved ²⁰⁶Pb/²³⁸U microprobe geochronology by the monitoring of a trace-element-related matrix effect; SHRIMP, ID-TIMS, ELA-ICP-MS and oxygen isotope documentation for a series of zircon standards: Chemical Geology, v. 205, no. 1–2, p. 115–140. [https://doi.org/10.1016/j.chemgeo.2004.01.003]
- Blakely, R. J.; Sherrod, B. L.; Hughes, J. F.; Anderson, M. L.; Wells, R. E.; Weaver, C. S., 2009, Saddle Mountain fault deformation zone, Olympic Peninsula, Washington: Western boundary of the Seattle uplift: Geosphere, v. 5, no. 2, p. 105–125. [https://doi.org/10.1130/GES00196.1]

- Blakely, R. J.; Sherrod, B. L.; Weaver, C. S., 2020, High-resolution aeromagnetic survey of the Centralia area, southwest Washington: U.S. Geological Survey data release. [https://doi.org/10.5066/P9T4UC6W]
- Blakely, R. J.; Wells, R. E.; Weaver, C. S., 1999, Puget Sound aeromagnetic maps and data, Open-File Report 99-0514, U.S. Geological Survey.
- Booth, D. B.; Troost, K. G.; Clague, J. J.; Waitt, R. B., 2004, The Cordilleran ice sheet. In Gillespie, A. R.; Porter, S. C.; Atwater, B. F., editors, *The Quaternary period in the United States*: Elsevier, v. 1, p. 17–43. [https://doi.org/10.1016/S1571-0866(03)01002-9]
- Bretz, J. H., 1911, The terminal moraine of the Puget Sound glacier: *Journal of Geology*, v. 19, no. 2, p. 161–174. [https://doi.org/10.1086/621826]
- Bretz, J. H., 1913, Glaciation of the Puget Sound region: Washington Geological Survey Bulletin 8, 244 p., 3 plates. [http://www.dnr.wa.gov/publications/ger_b8_glaciation_pugetsound.pdf]
- Brocher, T. M.; Parsons, Tom; Blakely, R. J.; Christensen, N. I.; Fisher, M. A.; Wells, R. E., 2001, Upper crustal structure in Puget Lowland, Washington: Results from the 1998 Seismic Hazards Investigations in Puget Sound: *Journal of Geophysical Research*, v. 106, no. B7, p. 13541–13564. [https://doi.org/10.1029/2001JB000154]
- Buckovic, W. A., 1979, The Eocene deltaic system of west-central Washington. In Armentrout, J. M.; Cole, M. R.; Ter Best, Harry, Jr., editors, *Cenozoic paleogeography of the western United States*: Society of Economic Paleontologists and Mineralogists Pacific Section, Pacific Coast Paleogeography Symposium 3, p. 147–163.
- Chang, Zhaoshan; Vervoort, J. D.; McClelland, W. C.; Knaack, Charles, 2006, U-Pb dating of zircon by LA-ICP-MS: *Geochemistry, Geophysics, Geosystems*, v. 7, no. 5, 14 p. [https://doi.org/10.1029/2005GC001100]
- Clement, C. R.; Pratt, T. L.; Holmes, M. L.; Sherrod, B. L., 2010, High-resolution seismic reflection imaging of growth folding and shallow faults beneath the southern Puget Lowland, Washington State: *Bulletin of the Seismological Society of America*, v. 100, no. 4, p. 1710–1723. [https://doi.org/10.1785/0120080306]
- Crandell, D. R., 1963, Surficial geology and geomorphology of the Lake Tapps quadrangle, Washington: U.S. Geological Survey Professional Paper 388-A, 84 p., 2 plates. [https://pubs.usgs.gov/pp/0388a/report.pdf]
- Crandell, D. R.; Miller, R. D., 1974, Quaternary stratigraphy and extent of glaciation in the Mount Rainier region, Washington: U.S. Geological Survey Professional Paper 847, 59 p., 2 plates. [https://doi.org/10.3133/pp847]
- Daneš, Z. F.; Bonno, M. M.; Brau, J. E.; Gilham, W. D.; Hoffman, T. F.; Johansen, D.; Jones, M. H.; Malfait, Bruce; Masten, J.; Teague, G. O., 1965, Geophysical investigation of the southern Puget Sound area, Washington: *Journal of Geophysical Research*, v. 70, no. 22, p. 5573–5580. [https://doi.org/10.1029/JZ070i022p05573]
- Drost, B. W.; Ely, D. M.; Lum, W. E., II, 1999, Conceptual model and numerical simulation of the ground-water-flow system in the unconsolidated sediments of Thurston County, Washington: U.S. Geological Survey Water-Resources Investigations Report 99-4165, 254 p. [https://doi.org/10.3133/wri994165]
- Eddy, M. P.; Bowring, S. A.; Umhoefer, P. J.; Miller, R. B.; McLean, N. M.; Donaghy, E. E., 2016, High-resolution temporal and stratigraphic record of Siletzia's accretion and triple junction migration from nonmarine sedimentary basins in central and western Washington: *Geological Society of America Bulletin*, v. 128, no. 3–4, p. 425–441. [https://doi.org/10.1130/B31335.1]
- Eddy, M. P.; Clark, K. P.; Polenz, Michael, 2017, Age and volcanic stratigraphy of the Eocene Siletzia oceanic plateau in Washington and on Vancouver Island: *Lithosphere*, v. 9, no. 4, p. 652–664. [https://doi.org/10.1130/L650.1]
- Finn, C. A., 1990, Geophysical constraints on Washington convergent margin structure: *Journal of Geophysical Research*, v. 95, no. B12, p. 19533–19546. [https://doi.org/10.1029/JB095iB12p19533]
- Gabet, E. J.; Horwath Burnham, J. L.; Perron, J. T., 2016, Critiques of the seismic hypothesis and the vegetation stabilization hypothesis for the formation of Mima mounds along the western coast of the U.S.: *Geomorphology*, v. 269, p. 40–42. [https://doi.org/10.1016/j.geomorph.2016.06.032]
- Galbraith, R. F.; Roberts, R. G.; Laslett, G. M.; Yoshida, H.; Olley, J. M., 2007, Optical dating of single and multiple grains of quartz from Jinnium Rock Shelter, northern Australia: Part 1, Experimental design and statistical models: *Archaeometry*, v. 41, no. 2, p. 339–364. [https://doi.org/10.1111/j.1475-4754.1999.tb00987.x]
- Gilmore, Gordon, 2008, *Practical Gamma-ray Spectrometry*, 2nd Edition: John Wiley & Sons, Ltd., 387 p.
- Gower, H. D.; Yount, J. C.; Crosson, R. S., 1985, Seismotectonic map of the Puget Sound region, Washington: U.S. Geological Survey Miscellaneous Investigations Series Map I-1613, 1 sheet, scale 1:250,000, with 15 p. text. [https://doi.org/10.3133/i1613]
- Hagen, R. A., 1987, The geology and petrology of the Northcraft Formation, Lewis County, Washington: University of Oregon Master of Science thesis, 252 p., 1 plate.
- Horwath Burnham, J. L.; Johnson, D. L., editors, 2012, Mima Mounds: The case for polygenesis and bioturbation: *Geological Society of America Special Paper 490*, 205 p. [https://doi.org/10.1130/SPE490]
- Huntley, D. J.; Lamothe, M., 2001, Ubiquity of anomalous fading in K-feldspars and the measurement and correction for it in optical dating: *Canadian Journal of Earth Sciences*, v. 38, no. 7, p. 1093–1106. [https://doi.org/10.1139/e01-013]
- Huot, S.; Lamothe, M., 2003, Variability of infrared stimulated luminescence properties from fractured feldspar grains: *Radiation Measurements*, v. 37, no. 4–5, p. 499–503. [https://doi.org/10.1016/S1350-4487(03)00014-3]
- Irvine, T. N.; Baragar, W. R. A., 1971, A guide to the chemical classification of the common volcanic rocks: *Canadian Journal of Earth Sciences*, v. 8, no. 5, p. 523–548. [https://doi.org/10.1139/e71-055]
- Koppers, A. A. P.; Staudigel, H.; Wijbrans, J. R., 2000, Dating crystalline groundmass separates of altered Cretaceous seamount basalts by the $^{40}\text{Ar}/^{39}\text{Ar}$ incremental heating technique, *Chemical Geology*, vol. 166, no. 1–2, p. 139–158. [https://doi.org/10.1016/S0009-2541(99)00188-6]
- Koppers, A. A. P., 2002, ArArCALC—Software for $^{40}\text{Ar}/^{39}\text{Ar}$ age calculations: *Computers & Geosciences*, v. 28, no. 5, p. 605–619. [https://doi.org/10.1016/S0098-3004(01)00095-4]
- Koppers, A. A. P.; Staudigel, Hubert; Pringle, M. S.; Wijbrans, J. R., 2003, Short-lived and discontinuous intraplate volcanism in the South Pacific: Hot spots or extensional volcanism?: *Geochemistry, Geophysics, Geosystems*, v. 4, no. 10, 49 p. [https://doi.org/10.1029/2003GC000533]
- Kuiper, K. F.; Deino, Alan; Hilgen, F. J.; Krijgsman, Wout; Renne, P. R.; Wijbrans, J. R., 2008, Synchronizing rock clocks of Earth history: *Science*, v. 320, no. 5875, p. 500–504. [https://doi.org/10.1126/science.1154339]
- Lanphere, M. A.; Baadsgaard, H., 2001, Precise K–Ar, $^{40}\text{Ar}/^{39}\text{Ar}$, Rb–Sr and U/Pb mineral ages from the 27.5 Ma Fish Canyon Tuff reference standard: *Chemical Geology*, v. 175, no. 3–4, p. 653–671. [https://doi.org/10.1016/S0009-2541(00)00291-6]
- Lau, Todd; Anderson, Megan; Polenz, Michael; Sadowski, Andrew; Becerra, Rebeca; Toth, Conner; Cakir, Recep; von Dassow, Wesley; Reedy, Tabor, 2018, Integrated geophysical investigation and 3D fault characterization of the Rochester and Adna 7.5-minute quadrangles, Thurston and Lewis Counties, Washington [abstract]: American Geophysical Union Fall Meeting, Abstract T131-0355.

- Lea, P. D., 1984, Pleistocene glaciation at the southern margin of the Puget lobe, western Washington: University of Washington Master of Science thesis, 96 p., 3 plates.
- Le Bas, M. J.; Le Maitre, R. W.; Streckeisen, A. L.; Zanettin, Bruno, 1986, A chemical classification of volcanic rocks based on the total alkali-silica diagram: *Journal of Petrology*, v. 27, no. 3, p. 745–750. [https://doi.org/10.1093/petrology/27.3.745]
- Lee, J.-Y.; Marti, Kurt; Severinghaus, J. P.; Kawamura, Kenji; Yoo, H.-S.; Lee, J. B.; Kim, J. S., 2006, A redetermination of the isotopic abundances of atmospheric Ar: *Geochimica et Cosmochimica Acta*, v. 70, no. 17, p. 4507–4512. [https://doi.org/10.1016/j.gca.2006.06.1563]
- Lesemann, J.-E.; Brennand, T. A.; Lian, O. B.; Sandorn, Paul, 2013, A refined understanding of the paleoenvironmental history recorded at the Okanagan Centre section, an MIS 4 stratotype, south-central British Columbia, Canada: *Journal of Quaternary Science*, v. 28, no. 8, p. 729–747. [https://doi.org/10.1002/jqs.2665]
- Logan, R. L.; Walsh, T. J., 2009, Mima Mounds formation and their implications for climate change [abstract]: Northwest Scientific Association Annual Meeting.
- Logan, R. L.; Walsh, T. J.; Stanton, B. W.; Sarikhan, I. Y., 2009, Geologic map of the Maytown 7.5-minute quadrangle, Thurston County, Washington: Washington Division of Geology and Earth Resources Geologic Map GM-72, 1 sheet, scale 1:24,000. [http://www.dnr.wa.gov/Publications/ger_gm72_geol_map_maytown_24k.pdf]
- Ludwig, K.R., 2012, User's Manual for Isoplot 3.75: A geochronological toolkit for Microsoft Excel: Spec. Publ., no. 5, Berkeley Geochronological Center, Berkeley, California, 75 p.
- Magsino, Sammantha; Sanger, Elizabeth; Walsh, T. J.; Palmer, S. P.; Blakely, R. J., 2003, The Olympia structure: Ramp or discontinuity? New gravity data provide more information [abstract]: Geological Society of America Abstracts with Programs, v. 35, no. 6, p. 479.
- McBirney, A. R., 1978, Volcanic evolution of the Cascade Range: Earth and Planetary Sciences Annual Reviews, v. 6, p. 437–456. [https://doi.org/10.1146/annurev.ea.06.050178.002253]
- McCaffrey, Robert; King, R. W.; Payne, S. J.; Lancaster, Matthew, 2013, Active tectonics of northwestern U. S. inferred from GPS-derived surface velocities: *Journal of Geophysical Research Solid Earth*, v. 118, no. 2, p. 709–723. [https://doi.org/10.1029/2012JB009473]
- Min, K.; Mundil, R.; Renne, P. R.; Ludwig, K. R., 2000, A test for systematic errors in $^{40}\text{Ar}/^{39}\text{Ar}$ geochronology through comparison with U/Pb analysis of a 1.1-Ga rhyolite: *Geochimica et Cosmochimica Acta*, v. 64, no. 1, p. 73–98. [https://doi.org/10.1016/S0016-7037(99)00204-5]
- Miyashiro, Akiho, 1974, Volcanic rock series in island arcs and active continental margins: *American Journal of Science*, v. 274, no. 4, p. 321–355. [https://doi.org/10.2475/ajs.274.4.321]
- Morrison, R. B., 1991, Introduction. In Morrison, R. B., editor, Quaternary nonglacial geology: Conterminous U.S.: Geological Society of America, v. K-2, p. 1–12. [https://doi.org/10.1130/DNAG-GNA-K2.1]
- Mundorff, M. J.; Weigle, J. M.; Holmberg, G. D., 1955, Ground water in the Yelm area, Thurston and Pierce Counties, Washington: U.S. Geological Survey Circular 356, 58 p., 2 plates. [https://doi.org/10.3133/cir356]
- Murray, A. S.; Wintle, A. G., 2000, Luminescence dating of quartz using an improved single-aliquot regenerative-dose protocol: *Radiation Measurements*, v. 32, no. 1, p. 57–73. [https://doi.org/10.1016/S1350-4487(99)00253-X]
- Nelson, A. R.; Personius, S. F.; Sherrod, B. L.; Buck, Jason; Bradley, L.-A.; Henley, Gary, II; Liberty, L. M.; Kelsey, H. M.; Witter, R. C.; Koehler, R. D.; Schermer, E. R.; Nemser, E. S.; Cladouhos, T. T., 2008, Field and laboratory data from an earthquake history study of scarps in the hanging wall of the Tacoma fault, Mason and Pierce Counties, Washington: U.S. Geological Survey Scientific Investigations Map 3060, 3 sheets. [http://pubs.usgs.gov/sim/3060/].
- Noble, J. B.; Wallace, E. F., 1966, Geology and ground-water resources of Thurston County, Washington, Volume 2: Washington Division of Water Resources Water Supply Bulletin 10, 141 p., 5 plates. [https://apps.ecology.wa.gov/publications/SummaryPages/WSB10b.html]
- Odum, J. K.; Stephenson, W. J.; Pratt, T. L.; Blakely, R. J., 2016, Shallow geophysical imaging of the Olympia anomaly: An enigmatic structure in the southern Puget Lowland, Washington State: *Geosphere*, v. 12, no. 5, p. 1617–1632. [https://doi.org/10.1130/GES01248.1]
- Paces, J. B.; Miller, J. D., Jr., 1993, Precise U-Pb ages of Duluth Complex and related mafic intrusions, northeastern Minnesota: Geochronological insights to physical, petrogenetic, paleomagnetic, and tectonomagmatic processes associated with the 1.1 Ga Midcontinent Rift System: *Journal of Geophysical Research: Solid Earth*, v. 98, no. B8, p. 13997–14013. [https://doi.org/10.1029/93JB01159]
- Palmer, S. P.; Magsino, S. L.; Bilderback, E. L.; Poelstra, J. L.; Folger, D. S.; Niggemann, R. A., 2004, Liquefaction susceptibility and site class maps of Washington State, by county: Washington Division of Geology and Earth Resources Open File Report 2004-20, 1 DVD (78 plates, 45 p. text). [https://fortress.wa.gov/dnr/geologydata/liquefaction_maps/ofr2004-20_report.pdf]
- Palmer, S. P.; Walsh, T. J.; Gerstel, W. J., 1999, Geologic folio of the Olympia–Lacey–Tumwater urban area, Washington: Liquefaction susceptibility map: Washington Division of Geology and Earth Resources Geologic Map GM-47, 1 sheet, scale 1:48,000, with 16 p. text. [http://www.dnr.wa.gov/publications/ger_gm47_geol_folio_olympia_tumwater_lacey_48k.pdf]
- Parker, B. L.; Goldstein, B. S.; Futornick, Z. O.; Pringle, P. T., 2008, Sedimentological evidence for an enriched glacial outburst flood in Thurston County, Washington [abstract]: Geological Society of America Abstracts with Programs, v. 40, no. 1, p. 70.
- Paton, Chad; Hellstrom, John; Paul, Bence; Woodhead, Jon; Hergt, Janet, 2011, Iolite: Freeware for the visualisation and processing of mass spectrometric data: *Journal of Analytical Atomic Spectrometry*, v. 26, no. 12, p. 2508–2518. [https://doi.org/10.1039/C1JA10172B]
- Pena, L. D.; Goldstein, S. L., 2014, Thermohaline circulation crisis and impacts during the mid-Pleistocene transition: *Science*, v. 345, no. 6194, p. 318–322. [https://doi.org/10.1126/science.1249770]
- Phillips, W. M.; Walsh, T. J.; Hagen, R. A., 1989, Eocene transition from oceanic to arc volcanism, southwest Washington. In Muffler, L. J. P.; Weaver, C. S.; Blackwell, D. D., editors, Proceedings of workshop XLIV—Geological, geophysical, and tectonic setting of the Cascade Range: U.S. Geological Survey Open-File Report 89-178, p. 199–256. [https://doi.org/10.3133/ofr89178]
- Pierce County, 2011, Pierce 2011 project, Pierce County Washington lidar, collected between 4/23/2011 and 9/3/2011 by Watershed Sciences Inc., 3-ft resolution, accessed June 2020, [http://lidarportal.dnr.wa.gov/], metadata available on portal [ger_pierce_2011_lidar_report.pdf].
- Polenz, Michael; Allen, M. D.; Legorreta Paulín, Gabriel; Eungard, D. W.; Cakir, Recep; Scott, S. P.; Mahan, S. A., 2016, Geologic map of the Shelton Valley 7.5-minute quadrangle, Mason County, Washington: Washington Division of Geology and Earth Resources Map Series 2016-02, 1 sheet, scale 1:24,000, 45 p. text. [http://www.dnr.wa.gov/publications/ger_ms2016-2_geol_map_shelton_valley_24k.zip]
- Polenz, Michael; Favia, J. G.; Hubert, I. J.; Legorreta Paulín, Gabriel; Cakir, Recep, 2015, Geologic map of the Port Ludlow and southern half of the Hansville 7.5-minute quadrangles, Kitsap and Jefferson Counties, Washington: Washington Division of Geology and Earth Resources Map Series 2015-02, 1 sheet, scale 1:24,000, 40 p. text. [http://www.dnr.wa.gov/publications/ger_ms2015-02_geol_map_port_ludlow_hansville_24k.zip]

- Polenz, Michael; Ostrom, B. A.; Lau, T. R.; Sadowski, A. J.; Blanks-Bennett, A. L.; Cakir, Recep; Tepper, J. H.; Legoretta Paulín, Gabriel; Nesbitt, Elizabeth; DuFrane, S. A., 2018, Geologic map of the Violet Prairie 7.5-minute quadrangle, Thurston and Lewis Counties, Washington: Washington Geological Survey Map Series 2018-04, 1 sheet, scale 1:24,000, 41 p. text. [http://www.dnr.wa.gov/publications/ger_ms2018-04_geol_map_violet_prairie_24k.zip]
- Polenz, Michael; Petro, G. T.; Contreras, T. A.; Stone, K. A.; Legorreta Paulín, Gabriel; Cakir, Recep, 2013, Geologic map of the Seabeck and Poulsbo 7.5-minute quadrangles, Kitsap and Jefferson Counties, Washington: Washington Division of Geology and Earth Resources Map Series 2013-02, 1 sheet, scale 1:24,000, with 39 p. text. [http://www.dnr.wa.gov/Publications/ger_ms2013-02_geol_map_seabeck-poulsbo_24k.zip]
- Polenz, Michael; Toth, C. H.; Samson, Catherine; Sadowski, A. J.; Becerra, R. I.; Lau, T. R.; Anderson, M. L.; Nesbitt, E. A.; Tepper, J. H.; DuFrane, S. A.; Legorreta Paulín, Gabriel, 2019, Geologic map of the Rochester 7.5-minute quadrangle, Thurston and Lewis Counties, Washington: Washington Geological Survey Map Series 2019-02, 1 sheet, scale 1:24,000. [http://www.dnr.wa.gov/publications/ger_ms2019-02_geol_map_rochester_24k.zip]
- Polenz, Michael; Samson, Catherine; Reedy, Tabor; von Dassow, Wesley; Duckworth, C. W.; Lau, T. R.; Anderson, M. L.; Nesbitt, E. A.; Tepper, J. H.; DuFrane, S. A.; Legoretta Paulín, Gabriel, 2020, Geologic map of the Oakville and Rainbow Falls 7.5-minute quadrangles, Lewis, Thurston, and Grays Harbor Counties, Washington: Washington Geological Survey Map Series 2020-02, 1 sheet, scale 1:24,000, 19 p. text. [http://www.dnr.wa.gov/publications/ger_ms2020-02_geol_map_oakville_rainbow_falls_24k.zip]
- Polenz, Michael; Vermeer, J. L.; Legorreta Paulín, Gabriel; Tepper, J. H.; Mahan, S. A.; Cakir, Recep, 2017, Geologic map of the Littlerock 7.5-minute quadrangle, Thurston County, Washington: Washington Geological Survey Map Series 2017-01, 1 sheet, scale 1:24,000, 36 p. text. [http://www.dnr.wa.gov/publications/ger_ms2017-01_geol_map_littlerock_24k.zip]
- Porter, S. C.; Swanson, T. W., 1998, Radiocarbon age constraints on rates of advance and retreat of the Puget lobe of the Cordilleran ice sheet during the last glaciation: *Quaternary Research*, v. 50, no. 3, p. 205–213. [<https://doi.org/10.1006/qres.1998.2004>]
- Pratt, T. L.; Johnson, S. Y.; Potter, C. J.; Stephenson, W. J.; Finn, C. A., 1997, Seismic reflection images beneath Puget Sound, western Washington State: The Puget Lowland thrust sheet hypothesis: *Journal of Geophysical Research*, v. 102, no. B12, p. 27469–27489. [<https://doi.org/10.1029/97JB01830>]
- Pringle, P. T.; Goldstein, B. S., 2002, Deposits, erosional features, and flow characteristics of the late-glacial Tanwax Creek–Ohop Creek Valley flood—A likely source for sediments composing the Mima Mounds, Puget Lowland, Washington [abstract]: *Geological Society of America Abstracts with Programs*, v. 34, no. 5, p. A-89.
- Puget Sound Lidar Consortium, 1999–2005, Puget Lowlands 2005 project, Amalgamation of many early lidar projects in the Puget Sound region, collected between 1999 and 2005 by various vendors, 6-ft resolution, accessed June 2020, [<http://lidarportal.dnr.wa.gov/>], metadata available on portal [ger_puget_lowlands_2005_lidar_report.pdf].
- Puget Sound Lidar Consortium, 2012, Grays Harbor 2012 project, Chehalis River Watershed Washington lidar, collected between 1/28/2012 and 4/07/2012 by Watershed Sciences Inc., 3-ft resolution, accessed June 2020, [<http://lidarportal.dnr.wa.gov/>], metadata available on portal [ger_grays_harbor_2012_lidar_report.pdf].
- Sadowski, A. J.; Becerra, R. I.; Toth, C. H.; Polenz, Michael; Anderson, M. L.; Lau, T. R.; Nesbitt, E. A.; Tepper, J. H.; DuFrane, S. A., 2019, Geologic map of the Adna 7.5-minute quadrangle, Lewis County, Washington: Washington Geological Survey Map Series 2019-01, 1 sheet, scale 1:24,000. [http://www.dnr.wa.gov/publications/ger_ms2019-01_geol_map_adna_24k.zip]
- Sadowski, A. J.; Keller, W. E.; Polenz, Michael; Lau, T. R.; Cakir, Recep; Nesbitt, Elizabeth; Tepper, J. H.; DuFrane, S. A.; Legoretta Paulín, Gabriel, 2018, Geologic map of the Centralia 7.5-minute quadrangle, Lewis County, Washington: Washington Geological Survey Map Series 2018-05, 1 sheet, scale 1:24,000, 43 p. text. [http://www.dnr.wa.gov/publications/ger_ms2018-05_geol_map_centralia_24k.zip]
- Schasse, H. W., compiler, 1987, Geologic map of the Centralia quadrangle, Washington: Washington Division of Geology and Earth Resources Open File Report 87-11, 28 p., 1 plate, scale 1:100,000. [http://www.dnr.wa.gov/Publications/ger_ofr87-11_geol_map_centralia_100k.zip]
- Scott, K. M.; Vallance, J. W.; Pringle, P. T., 1995, Sedimentology, behavior, and hazards of debris flows at Mount Rainier, Washington: U.S. Geological Survey Professional Paper 1547, 56 p., 1 plate. [<https://doi.org/10.3133/pp1547>]
- Sherrod, B. L., 2001, Evidence for earthquake-induced subsidence about 1100 yr ago in coastal marshes of southern Puget Sound, Washington: *Geological Society of America Bulletin*, v. 113, no. 10, p. 1299–1311. [[https://doi.org/10.1130/0016-7606\(2001\)113<1299:EFEISA>2.0.CO;2](https://doi.org/10.1130/0016-7606(2001)113<1299:EFEISA>2.0.CO;2)]
- Sláma, Jiří; Košler, Jan; Condon, D. J.; Crowley, J. L.; Gerdes, Axel; Hanchar, J. M.; Horstwood, M. S. A.; Morris, G. A.; Nasdala, Lutz; Norberg, Nicholas; Schaltegger, Urs; Schoene, Blair; Tubrett, M. N.; Whitehouse, M. J., 2018, Plešovice zircon—A new natural reference material for U-Pb and Hf isotopic microanalysis: *Chemical Geology*, v. 249, no. 1–2, p. 1–35. [<https://doi.org/10.1016/j.chemgeo.2007.11.005>]
- Snavely, P. D., Jr.; Brown, R. D., Jr.; Roberts, A. E.; Rau, W. W.; Schopf, J. M., 1958, Geology and coal resources of the Centralia–Chehalis district, Washington, with a section on microscopical character of the Centralia–Chehalis coal: U.S. Geological Survey Bulletin 1053, 159 p., 6 plates. [<https://doi.org/10.3133/b1053>]
- Snavely, P. D., Jr.; Rau, W. W.; Hoover, Linn, Jr.; Roberts, A. E., 1959, McIntosh Formation, Centralia–Chehalis coal district, Washington. In Washington Division of Mines and Geology, Tertiary stratigraphic papers, southwestern Washington: Washington Division of Mines and Geology Reprint 3, 10 p. [http://www.dnr.wa.gov/publications/ger_reprint3_strat_papers_sw_wa.pdf]
- Snavely, P. D., Jr.; Roberts, A. E.; Hoover, Linn, Jr.; Pease, M. H., Jr., 1951, Geology of the eastern part of the Centralia–Chehalis coal district, Lewis and Thurston Counties, Washington: U.S. Geological Survey Coal Investigations Map C8, 2 sheets, scale 1:31,680. [<https://doi.org/10.3133/coal8>]
- Stanley, W. D.; Fuis, G. S.; Mooney, W. D., 1989, Details of crustal structure in the Cascade Range and surrounding regions from seismic and magnetotelluric data. In Muffler, L. J. P.; Weaver, C. S.; Blackwell, D. D., editors, *Proceedings of workshop XLIV—Geological, geophysical, and tectonic setting of the Cascade Range*: U.S. Geological Survey Open-File Report 89-178, p. 31–73. [<http://pubs.er.usgs.gov/publication/ofr89178>]
- Steiger, R. H.; Jaeger, E., 1977, Subcommittee on geochronology: Convention on the use of decay constant in geo- and cosmochronology: *Earth and Planetary Science Letters*, v. 36, no. 3, p. 359–362. [[https://doi.org/10.1016/0012-821X\(77\)90060-7](https://doi.org/10.1016/0012-821X(77)90060-7)]
- Sun, S.-s.; McDonough, W. F., 1989, Chemical and isotopic systematics of oceanic basalts: Implications for mantle composition and processes. In Saunders, A. D.; Norry, M. J., editors, *Magmatism in the ocean Basins*: Geological Society of London Special Publication 42, p. 313–345. [<https://doi.org/10.1144/GSL.SP.1989.042.01.19>]
- Taylor, J. R., 1997, An introduction to error analysis: The study of uncertainties in physical measurements, second edition: University Science Books, 327 p.

- Thomas, S. D.; Clark, Alexis; Brown, Phil, 2007, Future groundwater supplies for three municipalities in the McAllister & Yelm sub-basins of Thurston County, Washington [abstract]: Washington Hydrogeology Symposium, p. 60. [<http://depts.washington.edu/uwconf/wahgs/abstracts2007.pdf>]
- Thurston County Geodata Center, 2011, Thurston 2011 project, Thurston County lidar, collected between 6/2011 - 7/2011 by Fugro EarthData Inc, 3-ft resolution, accessed June 2020, [<http://lidarportal.dnr.wa.gov/>], metadata available on portal [ger_thurston_2011_lidar_report.pdf].
- Troost, K. G., 2016, Chronology, lithology and paleoenvironmental interpretations of the penultimate ice-sheet advance into the Puget Lowland, Washington State: University of Washington Doctor of Philosophy thesis, 239 p.
- Troost, K. G.; Booth, D. B., 2008, Geology of Seattle and the Seattle area, Washington. In Baum, R. L.; Godt, J. W.; Highland, L. M., editors, Landslides and engineering geology of the Seattle, Washington area: Geological Society of America Reviews in Engineering Geology XX, p. 1–36. [[https://doi.org/10.1130/2008.4020\(01\)](https://doi.org/10.1130/2008.4020(01))]
- Upham, Warren, 1904, Glacial and modified drift in and near Seattle, Tacoma, and Olympia: The American Geologist, a Monthly Journal of Geology and Allied Sciences, v. 34, no. 4, p. 203–214.
- U.S. Geological Survey, 2016, SWWA foothills 2017 project, Western Washington 3DEP lidar, collected between Mar. 17 and Sept. 30, 2016 by Quantum Spatial Inc., 3-ft resolution, accessed June 2020, [<http://lidarportal.dnr.wa.gov/>], metadata available on portal [ger_swwa_foothills_2017_lidar_report.pdf].
- U.S. Geological Survey Geologic Names Committee, 2010, Divisions of geologic time—Major chronostratigraphic and geochronologic units: U.S. Geological Survey Fact Sheet 2010-3059, 2 p. [<http://pubs.usgs.gov/fs/2010/3059/>]
- Van Wagoner, T. M.; Crosson, R. S.; Creager, K. C.; Medema, G. F.; Preston, L. A.; Symons, N. P.; Brocher, T. M., 2002, Crustal structure and relocated earthquakes in the Puget Lowland, Washington, from high-resolution seismic tomography: Journal of Geophysical Research: Solid Earth, v. 107, no. B12, p. ESE 22-1–22-23. [<https://doi.org/10.1029/2001JB000710>]
- Walker, J. D.; Geissman, J. W., compilers, 2009, Geologic time scale: Geological Society of America, 1 p. [<https://doi.org/10.1130/2009.CTS004R2C>]
- Wallace, E. F.; Molenaar, Dee, 1961, Geology and ground-water resources of Thurston County, Washington, Volume 1: Washington Division of Water Resources Water Supply Bulletin 10, v. 1, 254 p., 2 plates. [<https://apps.ecology.wa.gov/publications/SummaryPages/WSB10a.html>]
- Walsh, T. J.; Korosec, M. A.; Phillips, W. M.; Logan, R. L.; Schasse, H. W., 1987, Geologic map of Washington—Southwest quadrant: Washington Division of Geology and Earth Resources Geologic Map GM-34, 2 sheets, scale 1:250,000, with 28 p. text. [http://www.dnr.wa.gov/publications/ger_gm34_geol_map_sw_wa_250k.pdf]
- Walsh, T. J.; Logan, R. L., 2005, Geologic map of the East Olympia 7.5-minute quadrangle, Thurston County, Washington: Washington Division of Geology and Earth Resources Geologic Map GM-56, 1 sheet, scale 1:24,000. [http://www.dnr.wa.gov/Publications/ger_gm56_geol_map_eastolympia_24k.pdf]
- Walsh, Timothy J.; Logan, Robert L.; Polenz, Michael; Schasse, Henry W., 2003a, Geologic map of the Nisqually 7.5-minute quadrangle, Thurston and Pierce Counties, Washington: Washington Division of Geology and Earth Resources Open File Report 2003-10, 1 sheet, scale 1:24,000. [<http://www.dnr.wa.gov/geology/pdf/ofr03-10.pdf>]
- Walsh, Tim; Pitre, Chris, 2013, Prolific Aquifers in South Puget Sound: 9th Washington Hydrogeology Symposium Field Trip Guide #1, 1 v.
- Walsh, T. J.; Polenz, Michael; Logan, R. L.; Lanphere, M. A.; Sisson, T. W., 2003b, Pleistocene tephrostratigraphy and paleogeography of southern Puget Sound near Olympia, Washington. In Swanson, T. W., editor, Western Cordillera and adjacent areas: Geological Society of America Field Guide, v. 4, p. 225–236. [<https://doi.org/10.1130/0-8137-0004-3.225>]
- Walters, K. L.; Kimmel, G. E., 1968, Groundwater occurrence and stratigraphy of unconsolidated deposits, central Pierce County, Washington: Washington Department of Water Resources Water-Supply Bulletin 22, 428 p., 3 plates.
- Washburn, A. L., 1988, Mima mounds—An evaluation of proposed origins with special reference to the Puget Lowland: Washington Division of Geology and Earth Resources Report of Investigations 29, 53 p. [http://www.dnr.wa.gov/publications/ger_ri29_mima_mounds.pdf]
- Wells, Ray; Bukry, David; Friedman, Richard; Pyle, Doug; Duncan, Robert; Haeussler, Peter; Wooden, Joe, 2014, Geologic history of Siletzia, a large igneous province in the Oregon and Washington Coast Range: Correlation to the geomagnetic polarity time scale and implications for a long-lived Yellowstone hotspot: Geosphere, v. 10, no. 4, p. 692–719. [<https://doi.org/10.1130/GES01018.1>]
- Wells, R. E.; McCaffrey, Robert, 2013, Steady rotation of the Cascade arc: Geology, v. 41, no. 9, p. 1027–1030. [<https://doi.org/10.1130/G34514.1>]
- Wiedenbeck, M.; Allé, P.; Corfu, F.; Griffin, W. L.; Meier, M.; Oberli, F.; Von Quadt, A.; Roddick, J. C.; Spiegel, W., 1995, Three natural zircon standards for U-Th-Pb, Lu-Hf, trace element and REE analyses: Geostandards Newsletters, v. 19, no. 1, p. 1–23. [<https://doi.org/10.1111/j.1751-908X.1995.tb00147.x>]
- Williams, I. S., 1998, U-Th-Pb geochronology by ion microprobe: In McKibben, M. A.; Shanks, W. C., III; Ridley, W. I., editors, Applications of microanalytical techniques to understanding mineralizing processes: Reviews in Economic Geology, v. 7, p. 1–35. [<https://doi.org/10.5382/Rev.07.01>]
- Wirth, E. A.; Vidale, J. E.; Frankel, A. D.; Pratt, T. L.; Marafi, N. A.; Thompson, Mika; Stephenson, W. J., 2019, Source-dependent amplification of earthquake ground motions in deep sedimentary basins: Geophysical Research Letters, v. 46, no. 12, p. 6443–6450. [<https://doi.org/10.1029/2019GL082474>]
- York, Derek, 1968, Least squares fitting of a straight line with correlated errors, Earth and Planetary Science Letters, v. 5, p. 320–324. [[https://doi.org/10.1016/S0012-821X\(68\)80059-7](https://doi.org/10.1016/S0012-821X(68)80059-7)]

Appendix A. New Luminescence Age Estimate

LUMINESCENCE ANALYSIS METHODS

Infrared stimulated luminescence (IRSL) dating for sample TPVm023b. Sample preparation and measurements were executed at the Illinois State Geological Survey. All operations were executed in a subdued orange light environment. The age was obtained with K-feldspar minerals (125–150 μm), on small aliquots. The age was corrected for anomalous fading. In addition, the sample is partially bleached; thus, the final age is derived from the minimum age model. For the equivalent dose (De) measurements, we relied on an automated Lexsyg Smart system equipped with a set of infrared (850-nm) LEDs for light stimulation. IRSL measurements were carried out with a single-aliquot regenerative dose (SAR) protocol (Murray and Wintle, 2000; Huot and Lamothe, 2003). Anomalous fading measurements were performed on the same aliquot previously used for equivalent dose measurements. Following De measurements, the aliquots were taken outside the luminescence system, for sunlight bleaching (2 days), before passing over the anomalous fading sequence of measurements. Fading measurements (Auclair and others, 2003) employed the same SAR parameters. Each aliquot was corrected using the Huntley and Lamothe (2001) fading correction model. The age distribution (derived from 16 independent aliquots) shows considerable scatter. The optimum burial age was derived from the application of the minimum age model (Galbraith and others, 1999). We chose to add an additional uncertainty (sb; 10%), in quadrature, to each individual aliquot before inserting the aliquots into the minimum age model to account for intrinsic and extrinsic uncertainties that cannot be properly quantified. To obtain the dose rate, sediments from the external portion of each sampling tube were dried, and a representative portion was encapsulated in thin disk-shaped containers (~20 g) and sealed with 2 layers of epoxy gel. A minimum waiting time of 21 days after sealing is recommended to restore the radioactive equilibrium of radon-222 daughter products (Gilmore, 2008). The specific activities (Bq/kg) were measured with a broad-energy high-purity germanium detector (BEGe), in a planar configuration, shielded by 15 cm of lead. Efficiency calibration of the detector was obtained with a set of six certified standards (IAEA-RGU-1, IAEA-RGTh-1, IAEA-RGK-1, IAEA-385, NIST 4350b, and NIST 4355).

Table A1. Optically Stimulated Luminescence (OSL) and Infrared Stimulated Luminescence results from age site GD3.

U-Pb site ID (sample ID) (geologic unit)		Sand lens in ancestral Nisqually River pebble gravel, sampled by Michael Polenz and Frank Hladky on Sept. 17, 2020 from 10–14 ft below terrace surface, just below readily apparent surface weathering profile. A sand fraction petrographic point count (n=50 each) revealed 58% perthitic K-feldspar, 20% plagioclase, 20% iron oxides and lithics, 30% quartz, 20% black opaques, 10% femic minerals. Luminescence analysis by Sebastien Huot (ISGS).
GD3 (TPVm023b) (Qpc)		
TRS	sec. 11, T15N R01E	
Lat/long. (degrees)	46.98782 -122.64257	
Elev. (ft)	255	
Result Type		Age (Ka) ± 2σ
Optically Stimulated Luminescence Result		42 ± 9 (from quartz; unreliable age, due to undesirable luminescence characteristics)
Infrared Stimulated Luminescence Result		26 ± 5 (K-feldspar, corrected for anomalous fading; minimum age model)
Luminescence Consensus Age Statement		26 ±5

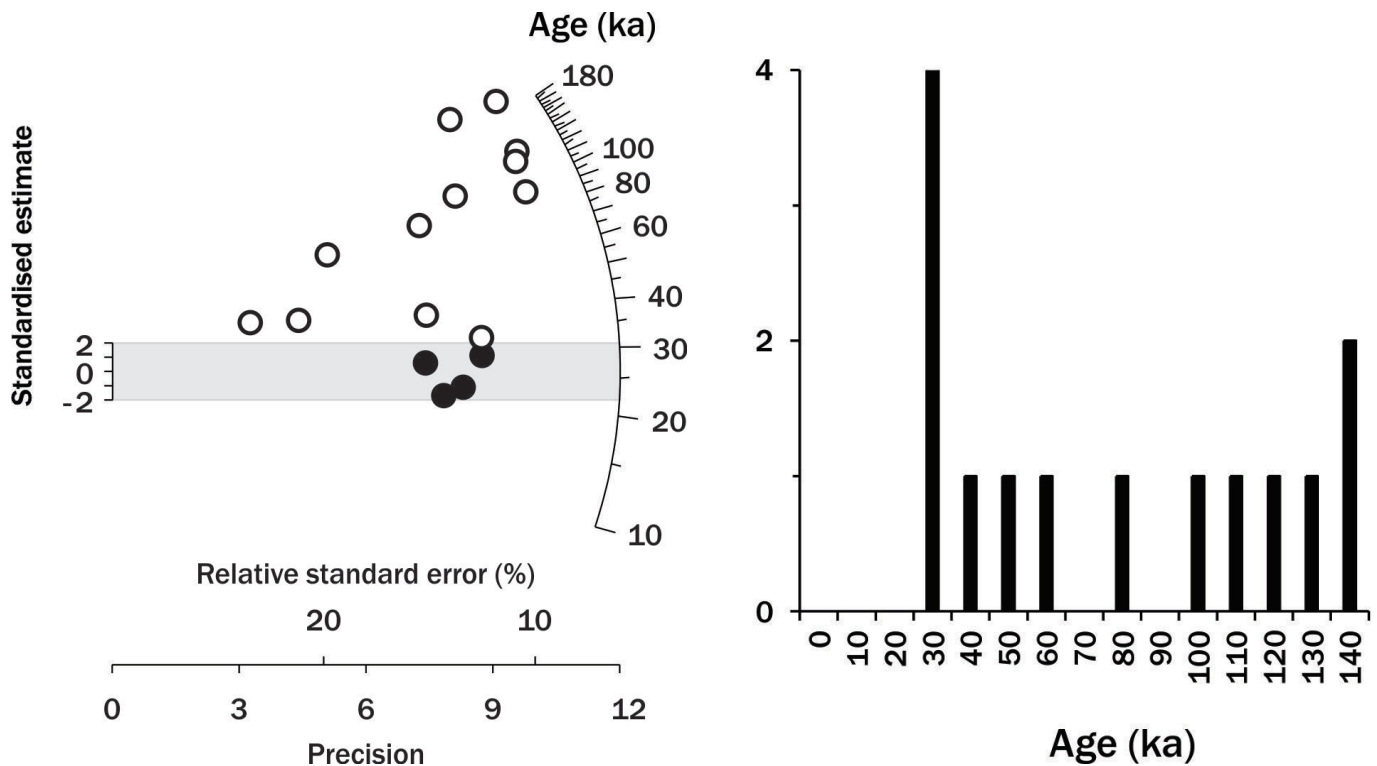


Fig A1A. Age distributions as a radial plot and histogram for all samples. Each circle on the radial plot represents the age and uncertainty for a single aliquot. The age is read on the arc axis, by drawing a straight line from (0, 0), passing through a circle and intersecting the radial axis (log scale). The (0, 0) coordinate corresponds to a 0 standardised estimate (y-axis) and 0 precision (x-axis). The uncertainty is read on the horizontal axis, by drawing a perpendicular line reaching a circle. Hence, two aliquots, having the same age, but with different uncertainty, will lay on the same straight line (from (0, 0) to the radial axis). The aliquot with the smaller uncertainty (higher precision) will be closer to the arc. Values (filled circles) within the light gray shaded band are consistent (at 2σ) with the weighted mean (Central Age Model). A cluster of aliquots within this shaded band expresses confidence that we have a population of grains consistent with a single age.

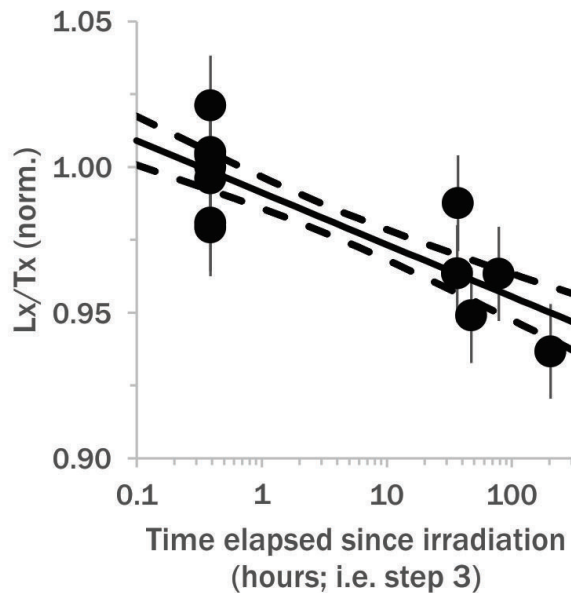


Fig A1B. Anomalous fading measurement for a representative aliquot. Repeated measurement cycles are made, on the same aliquot, with different delays between the irradiation and the IRSL measurement. The slope is proportional to the fading rate, used in the fading correction model. The two dashed lines represent the 1σ error envelopes. Note the logarithmic time axis.

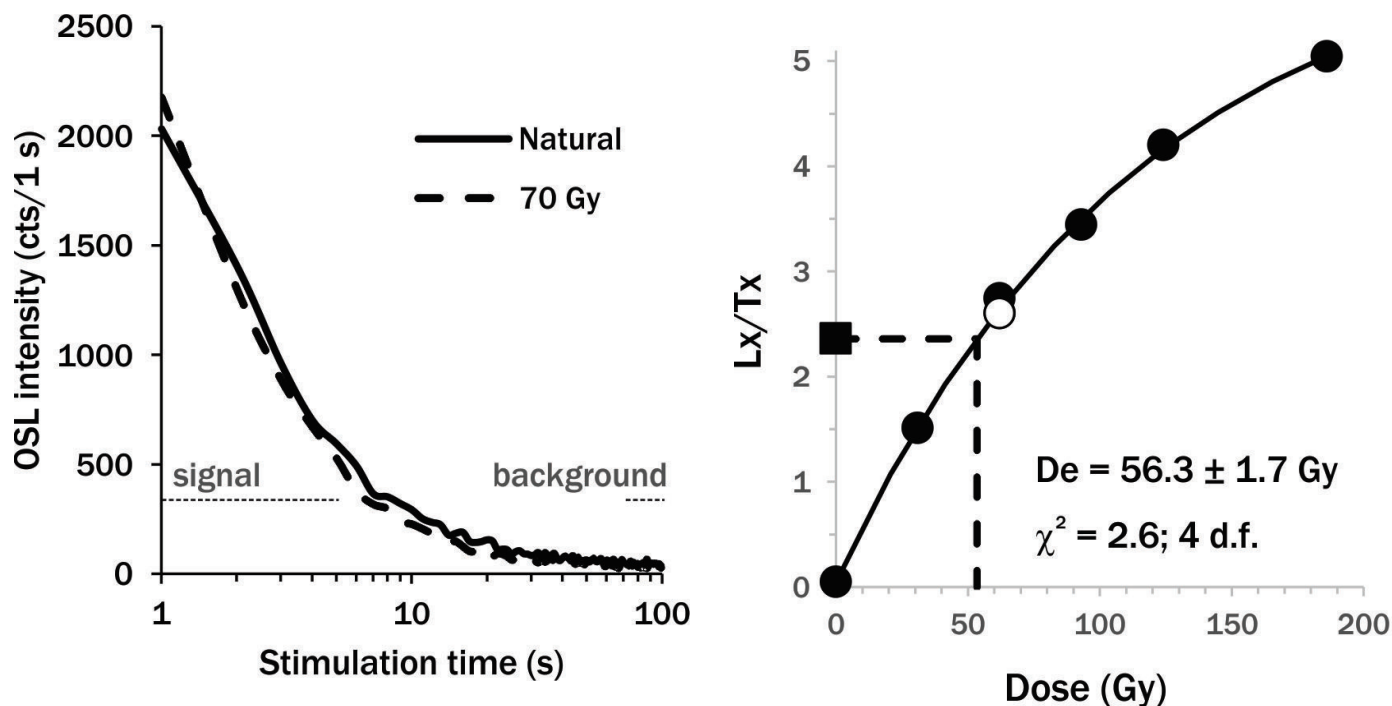


Fig A1C. Left: Typical IRSL decay curve for a naturally dosed aliquot (solid curve) or laboratory-induced dose (dashed curve, in Gy). The area under the curve is proportional to the dose of radiation stored within the mineral. **Right:** Luminescence dose response curve for the same aliquots shown in the other figures. Each point corresponds to the IRSL (Lx) of a natural (red square) or laboratory-induced dose (filled circles), normalized by the luminescence response to a fixed test dose (Tx). A repeat measurement (the recycling test; open circles) was performed at the end. The equivalent dose is obtained by interpolation. For the aliquots shown here, the observed measurements scatter well around the predicted best-fit curve.

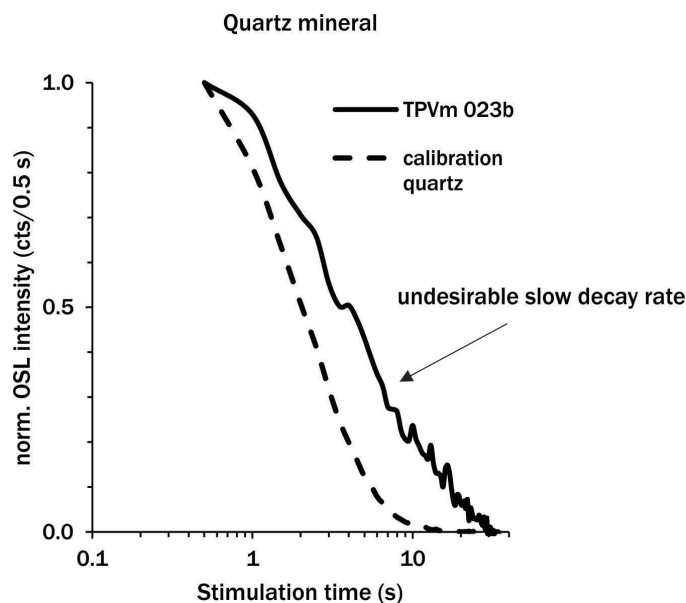


Fig A1D. Typical OSL decay curve for a naturally dosed aliquot (solid curve) or from a near-perfect quartz mineral (dashed curve, in Gy). The area under the curve is proportional to the dose of radiation stored within the mineral. In order to yield an accurate OSL age, the luminescence signal must follow a shape that closely matches that of a calibration quartz. Here, the decay rate is much slower. Measured on the Lexsyg Smart System with green LED.

Appendix B. New Detrital U/Pb Age Estimate

Zircon U-Pb ages from GD4 (TPVm201a) were measured at the Radiogenic Isotope and Geochronology Lab (RIGL) at Washington State University using an Analyte G2 193 excimer laser ablation system coupled with a Thermo-Finnigan Element 2 single-collector, inductively coupled, plasma mass spectrometer. The laser parameters were 25 μm in diameter spot size, 10 Hz repetition rate and $\sim 5.0 \text{ J/cm}^2$. For the U-Pb measurement, we mostly followed the method of Chang and others (2006), except for the use of the 193 nm laser system instead of a 213 nm laser. A 10-second blank measurement of the He and Ar carrier gases (Laser off) before each round of analyses was followed by 250 scans across masses ^{202}Hg , $^{204}\text{Pb}+\text{Hg}$, ^{206}Pb , ^{207}Pb , ^{208}Pb , ^{232}Th , ^{235}U , and ^{238}U during ~ 30 second laser ablation period. Analyses of zircon unknowns, standards and quality control zircon grains were interspersed with analyses of external calibration standards, typically with 10–12 unknowns bracketed by multiple analyses of two different zircon standards (Plešovice and FC-1). The Plešovice standard (337 Ma; Sláma and others, 2008) was used to calibrate the $^{206}\text{Pb}/^{238}\text{U}$ and $^{207}\text{Pb}/^{235}\text{U}$ ages, and the FC-1 standard (1099 Ma; Paces and Miller, 1993) was used for calibration of $^{207}\text{Pb}/^{206}\text{Pb}$ ages owing to its high count rate for ^{207}Pb (~ 2 –4 times higher than that of Plešovice). Zircon 91500 (1065 Ma; Wiedenbeck and others, 1995; $n=28$ $^{207}\text{Pb}/^{206}\text{Pb}$ age = $1063 \pm 2.4/-5.0$ Ma), Fish Canyon Tuff (~ 27.5 Ma Lanphere and Baadsgaard, 2001; $n=35$ $^{206}\text{Pb}/^{238}\text{U}$ age = $27.9 \pm 0.1/-0.2$ Ma) and Temora2 (417 Ma; Black and others, 2004; $n=48$ $^{206}\text{Pb}/^{238}\text{U}$ age = $417.0 \pm 1/-1$ Ma) were used as quality control standards. Data were processed offline using the Iolite software (Paton and others, 2011). Common Pb correction was performed using the ^{207}Pb method (Williams, 1998). Plots were calculated using Isoplot 4.16 (Ludwig, 2012).

Table B1. Detrital zircon maximum constraining age on tuffaceous sediment.

U-Pb site ID (sample ID) (geologic unit)		
GD4 (TPVm201a) (Evcn)		Zircon crystals extracted from a tuffaceous sediment bed (weathered to yellow bentonite) sampled near the base of more than 30 ft of Northcraft Formation interbedded volcanoclastic rocks and lavas (map unit Evcn). The sampled sediment rests on a 2–4 ft-thick paleosol that is itself weathered into gabbro of the "Columbia Granite" quarry (map unit Eign). The reported age is from the youngest of 92 zircons. The analysis was performed by Vic Valencia (ZirChron LLC) and Jeff Vervoort (Washington State University). Thin section petrography of the sample revealed irregularly shaped, angular fragments cemented to the slide. These fragments are comprised of 70–80% reddish-brown glass; 3–5% black oxides; $\sim 20\%$ altered feldspar; trace amounts of clinopyroxene microcrysts.
TRS	sec. 11, T15N R01E	
Lat/long. (degrees)	46.7936222801 -122.65039845	
Elev. (ft)	255	
Result Type		Age (Ma) $\pm 2\sigma$
Detrital Zircon U-Pb		$<38.4 \pm 0.5$

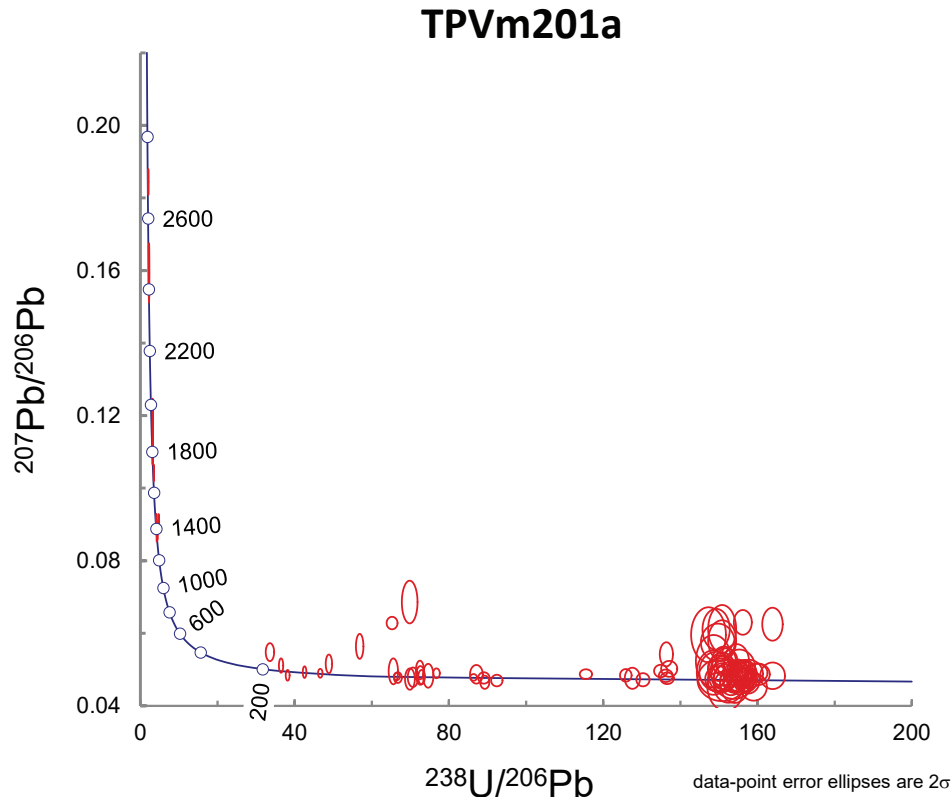


Figure B1A. Concordia plot $^{207}\text{Pb}/^{206}\text{Pb}$ vs $^{238}\text{U}/^{206}\text{Pb}$.

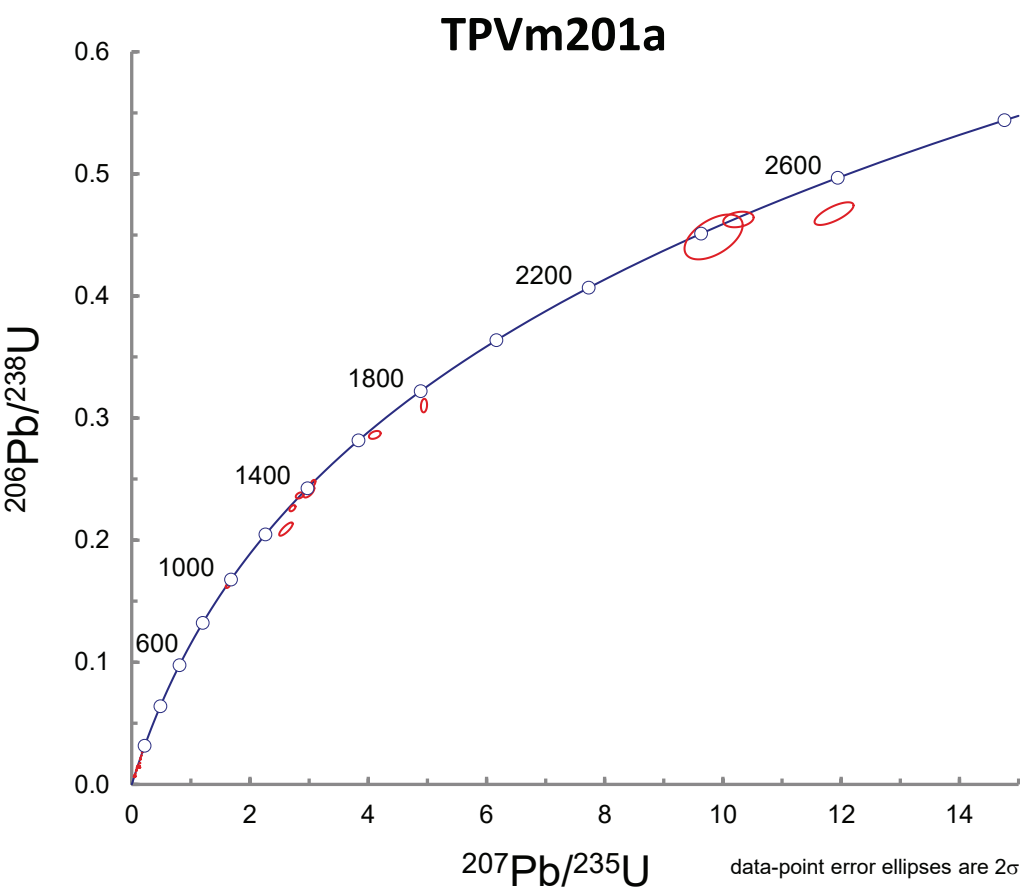


Figure B1B. Concordia plot $^{206}\text{Pb}/^{238}\text{U}$ vs $^{207}\text{Pb}/^{235}\text{U}$.

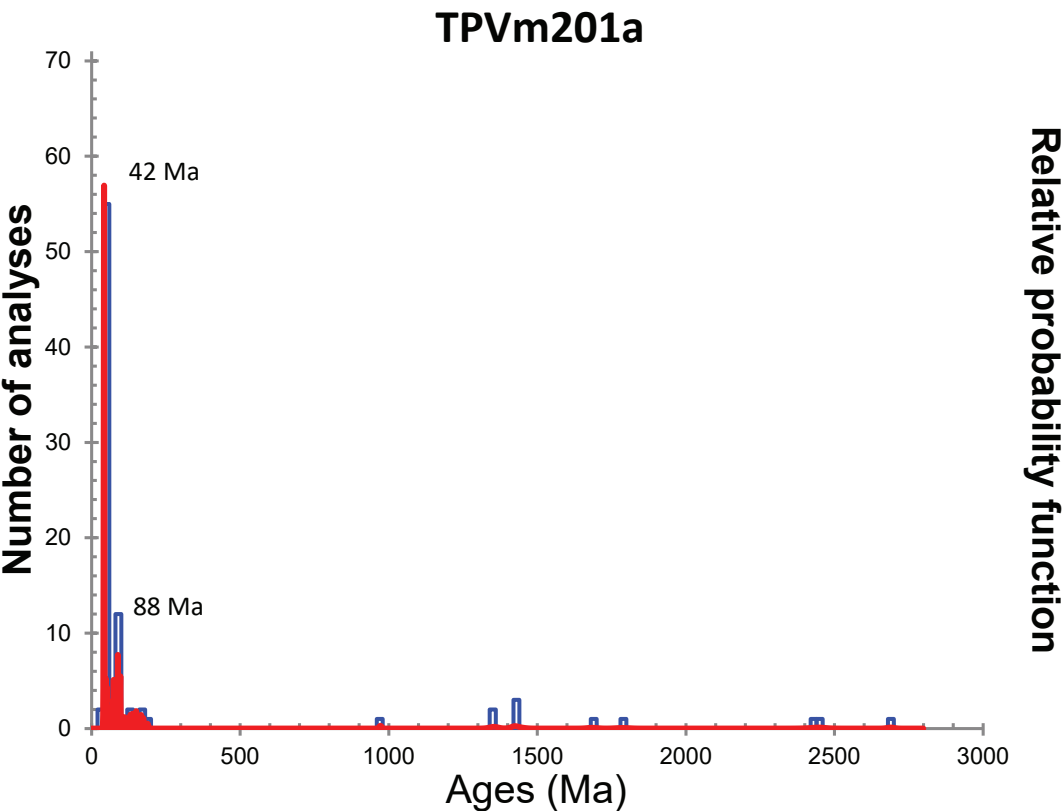


Figure B1C. Spectrum of detrital zircon ages from age site GD4. The blue line is a histogram of the ages of analyzed individual zircons binned into 20 Ma intervals. The relative probability function (red curve) presents a cumulative probability distribution of ages. The height of the red peaks are influenced by the precision error of the age analyses and the overlap of the age analyses. Thus the higher red peaks indicate higher probability age analyses of the sample.

Appendix C. New $^{40}\text{Ar}/^{39}\text{Ar}$ Age Estimates

Six Northcraft Formation samples from the Vail and Tenalquot Prairie 7.5-minute quadrangles yielded seven $^{40}\text{Ar}/^{39}\text{Ar}$ age analyses. Samples were crushed, sieved, washed, and dried using standard mineral separation techniques. Groundmass splits were rinsed with cold water and oven dried at 55°C. Dry samples were then sieved to 250–150 μm . Special care was taken to remove alteration material by intensive acid leaching using a combination of HCl and HNO₃ at different acid strength (Koppers and others, 2000). A final separate of groundmass was obtained by carefully removing any visible alteration or adhering crystal phases under a binocular microscope prior to packaging and irradiation of the sample.

$^{40}\text{Ar}/^{39}\text{Ar}$ ages (Tables C1 and DS3) were obtained by incremental heating using a ThermoFisher Scientific ARGUS-VI mass spectrometer and data collection using internal lab software ArArExperiments version 4.4.0. The samples were irradiated for 6 hours (Irradiations 20-OSU-05 and 21-OSU-01 in the CLICIT position in the Oregon State University's TRIGA nuclear reactor). Samples were irradiated with the Fish Canyon Tuff sanidine (FCT-2-NM sanidine) with an age of 28.201 ± 0.023 Ma, 1 σ flux monitor (Kuiper and others, 2008). Individual J-values for each sample were calculated by polynomial extrapolation of the measured flux gradient against irradiation height and typically give 0.06–0.12% uncertainties (1 σ). The $^{40}\text{Ar}/^{39}\text{Ar}$ incremental heating age determinations were performed on a multi-collector ARGUS-VI mass spectrometer at Oregon State University that has five Faraday collectors, two of which are fitted with 1012 Ohm resistors for masses ^{41}Ar and ^{40}Ar and three of which are fitted with 1013 Ohm resistors for argon masses ^{39}Ar , ^{38}Ar , and ^{37}Ar . One ion-counting CuBe electron multiplier is positioned next to the lowest mass Faraday collector. This allows us to measure simultaneously all argon isotopes, with mass 36 on the multiplier and masses 37 through 40 on the four adjacent Faradays. This configuration provides the advantages of running in a full multi-collector mode while measuring the lowest peak (on mass 36) on the highly sensitive electron multiplier (which has an extremely low dark-noise and a very high peak/noise ratio). Irradiated samples were loaded into Cu-planchettes in an ultra-high vacuum sample chamber and incrementally heated by scanning a Synrad Firestar 20 Watt defocused 30 W CO₂ laser beam in pre-set patterns across the sample, in order to release the argon evenly. Each heating step lasts 62 seconds. After heating, reactive gases were cleaned up using four SAES Zr-Al AP10 getters for 3 minutes; two operated at 450°C and two operated at room temperature (21°C). All ages were calculated using the corrected Steiger and Jäger (1977) decay constant of $5.530 \pm 0.097 \times 10^{-10}$ 1/yr (2 σ) as reported by Min and others (2000). For all other constants used in the age calculations we refer to table 2 in Koppers and others (2003). Incremental heating plateau ages and isochron ages were calculated as weighted means with 1/ σ^2 as the weighting factor (Taylor, 1997) and as YORK2 least-square fits with correlated errors (York, 1969) using the ArArCALC v2.6.2 software from Koppers (2002) available from the <http://earthref.org/ArArCALC/> website.

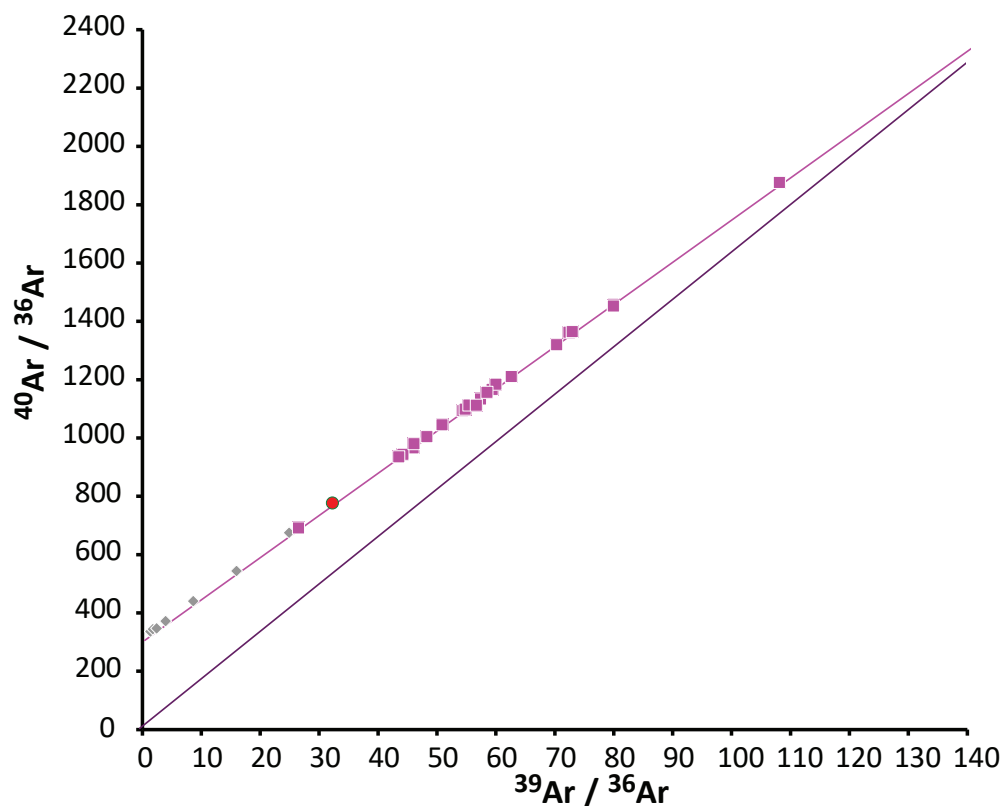
Argon isotopic results are corrected for system blanks, radioactive decay, mass discrimination, reactor-induced interference reactions, and atmospheric argon contamination. Decay constants reported by Min and others (2000) are utilized for age calculation. Isotope interference corrections as determined using the ARGUS VI are: ($^{36}\text{Ar}/^{37}\text{Ar}$) Ca = 0.0002703 ± 0.0000005 ; ($^{39}\text{Ar}/^{37}\text{Ar}$) Ca = 0.0006425 ± 0.0000059 ; ($^{40}\text{Ar}/^{39}\text{Ar}$) K = 0.000607 ± 0.000059 ; ($^{38}\text{Ar}/^{39}\text{Ar}$) K = 0.012077 ± 0.000011 . Ages were calculated assuming an atmospheric $^{40}\text{Ar}/^{36}\text{Ar}$ ratio of 298.56 ± 0.113 (Lee and others, 2006). Data reduction and age calculations were processed using Ar-Ar Calc 2.7.0 (Koppers, 2002). Plateau ages are defined as including >50% of the total ^{39}Ar released with at least three consecutive steps, where the $^{40}\text{Ar}/^{39}\text{Ar}$ ratio for each step is in agreement with the mean at the 95% confidence level. In many cases only a mini-plateau age is given, where a mini-plateau is present at <50% of the ^{39}Ar released.

Table C1. Summary of seven new $^{40}\text{Ar}/^{39}\text{Ar}$ ages from the Tenalquot Prairie and Vail 7.5-minute quadrangles. Elevations were estimated using best available lidar (as of 2020), mosaicked at WGS, projected to State Plane South, NAD 83 HARN, US Survey feet. Lidar-based elevation statements were not adjusted to account for systematic projection differences relative to the base map. Lidar level 0 is theoretically 3.396 to 3.488 ft below base map level 0 [http://www.ngs.noaa.gov/cgi-bin/VERTCON/vert_con.pr]. Latitude and longitude coordinates are in WGS84. $^{40}\text{Ar}/^{39}\text{Ar}$ analyses by Daniel Miggins and staff, Argon Geochronology Lab, College of Earth, Ocean, and Atmospheric Sciences, Oregon State University, Corvallis, Oregon. Petrography for sample characterizations by Frank Hladky (WGS).

⁴⁰ Ar/ ³⁹ Ar site (sample ID) (geologic unit)		Sample taken near inactive quarry along Johnson Creek Road. The geochronology lab tracked the Groundmass Mini-Plateau age (GD6) as sample TPVf021 and the Plagioclase Plateau age (GD5) as sample TPVf027. Both ages are, in fact, from the same sample, TPVf021. The rock consists of light medium tannish grey, porphyritic basalt with strikingly large plagioclase phenocrysts up to 1.5 cm, although most range 1 to 5 mm. Plagioclase phenocrysts account for 15–20% of the rock. Greenish black pyroxene up to 5 mm comprise about 3%. The rest of the rock is groundmass that microscopy indicates is comprised of 25–30% orange-brown glass, 50–55% plagioclase microlites, 10–15% clinopyroxene microcrysts, and 5–7% black oxides. Due to intense Ar ³⁹ recoil in the groundmass analysis the plagioclase yielded a younger age statement than the groundmass did.
GD5 and GD6 (TPVf021) (Evan)		
TRS	sec. 30, T16N R01E	
Lat/long. (degrees)	46.84797178 -122.7236031	
Elev. (ft)	398	
Result Type		Age (Ma) ± 2σ
Groundmass Mini-Plateau Age		43.59 ±0.12
Plagioclase Plateau Age		42.62 ±0.12
GD10 (TPVm021) (Evan)		Dark gray, basaltic andesite porphyry from a prominent outcrop on the south side of State Highway 507. Glomerocrystic plagioclase phenocrysts up to 6 mm and finer-grained plagioclase as small as 0.5 mm are about 50% of the rock, the rest consisting of a black crypto-granular groundmass that contains 1–3% black pyroxene <1 mm. Microscopy indicates the rock has a mostly intergranular [grain to grain] texture, although intersertal pools of glass locally separate grains. Overall, as viewed from low to high magnification, the rock consists of 2–3% black opaques, 20–25% clinopyroxene microcrysts, ~7% reddish greenish brown partly devitrified glass between grains, 70% plagioclase microlaths, and a trace of altered, fine-grained olivine crystals. The texture is consistent with hypabyssal intrusion or an exceedingly thick lava flow.
TRS	sec. 33, T16N R01E	
Lat/long. (degrees)	46.8246518911731 -122.683600197086	
Elev. (ft)	380	
Result Type		
Groundmass Total Fusion Age		45.80 ±0.07
GD8 (TPVf085) (Evan)		Dark gray to black, aphanitic andesite with tan weathering, sampled on a prominent knoll south of the summit of Baumgard Hill. The rock breaks concoidally, yielding sharp edges. Under medium magnification the rock consists entirely of microcrystalline material that includes 10-15% black opaque microcrysts, ~10% pyroxene microcrysts, and ~40% plagioclase microlites haphazardly oriented in 50% clear glass.
TRS	sec. 33, T16N R01E	
Lat/long. (degrees)	46.8246518911731 -122.683600197086	
Elev. (ft)	1585	
Result Type		
Groundmass Total Fusion Age		43.63 ±0.08
GD7 (TPVf020) (Evan)		Dark, olive-gray, very fine grained andesite, sampled south of an inactive quarry on Johnson Creek Road. Under the microscope the rock reveals hyalopilitic texture (randomly oriented plagioclase microlites in glass). The mineral proportions of the microcrysts are 15–25% opaque oxides, 25–35% glass, 20–25% plagioclase, and 5–10% partly altered clinopyroxene.
TRS	sec. 30, T16N R01E	
Lat/long. (degrees)	46.8440001952439 -122.724765549329	
Elev. (ft)	398	
Result Type		
Groundmass Mini-Plateau Age		43.51 ±0.08

Table C1 continued.

⁴⁰ Ar/ ³⁹ Ar site (sample ID) (geologic unit)		Dark greenish blue-gray, porphyritic andesite with light yellowish-orange weathering, sampled from a Weyerhaeuser quarry that was active during part of the 2020 field season. Viewed megascopically and microscopically, the rock is about 30% plagioclase phenocrysts 1–2 mm and 1–2% clinopyroxene phenocryst about 0.5 mm. The other 60–70% of the rock is mostly plagioclase microlites oriented haphazardly in clear glass, accented by a few percent of pyroxene microcrysts and 5–7% black opaque microcrysts.
GD9 (TPVf054) (Evan)		
TRS	sec. 7, T15N R01E	
Lat/long. (degrees)	46.8011557526894 -122.724997069147	
Elev. (ft)	827	
Result Type		Age (Ma) ± 2σ
Groundmass Mini-Plateau Age		44.08 ±0.08
GD11 (TPVf204) (Eign)		Gabbro from the "Columbia Granite" quarry, which was active during the 2020 field season. GD11 was collected as sample TPVf204; a duplicate sample (TPVf203) was used for thin section petrography and geochemical analysis (G55); additional petrography and geochemistry from a sample near the upper boundary of the gabbro (G51, sample TPVm201b) yielded similar geochemistry and petrographic trends but a slightly finer-grained texture. Petrography reveals an intergranular texture with no glass, and that the rock is 75% plagioclase ranging from mostly phenocrysts up to 5 mm (usually up to 3 mm) to groundmass size. Snively and others (1958) determined that the plagioclase is calcic (labradorite). Glomerocrystic clinopyroxene comprises 20% of the rock and ranges from groundmass to phenocrysts. Black opaques comprise about 7% of the rock and range from phenocrysts to groundmass; hornblende up to 2 mm is an occasional component. Broken rock surfaces sometimes display zeolite coatings 1–2 mm thick often as cm-scale radial rosettes. An erosionally unconformable contact with overlying Northcraft lava and volcanoclastic sediments ranges from undulatory to planar, locally includes a paleosol weathered into the gabbro (as at GD4), and broadly appears to dip a few degrees east, as exposed in the highwall and along the access road.
TRS	sec. 11, T15N R01E	
Lat/long. (degrees)	46.792565 -122.649423	
Elev. (ft)	684	
Result Type		
Stacked Groundmass Mini-Plateau Ages (n=2)		38.68 ±0.13

A**Ar-Ages in Ma**

WEIGHTED PLATEAU

 42.62 ± 0.12

TOTAL FUSION

 42.86 ± 0.12

NORMAL ISOCHRON

 42.72 ± 0.37

INVERSE ISOCHRON

 42.74 ± 0.37

MSWD

(PROBABILITY)

1.01 (45%)

Sample Info

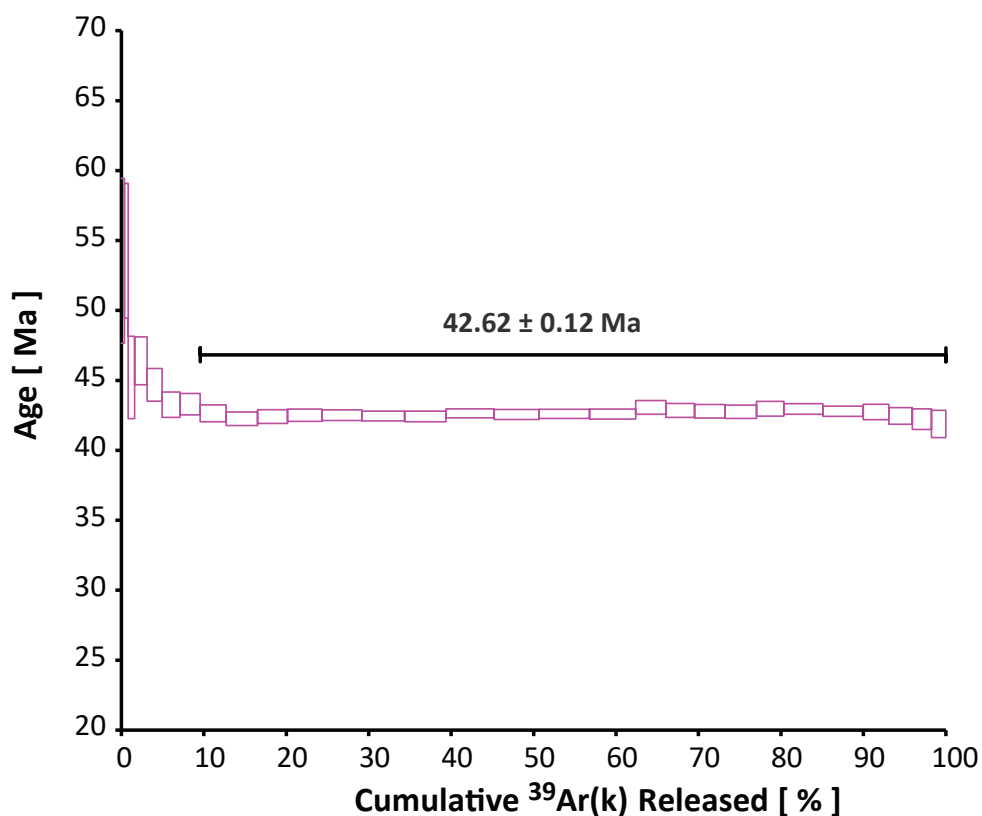
Plagioclase

West Cascades

Dan Miggins

IRR = 20-OSU-05

(SA30-20)

B**Ar-Ages in Ma**

WEIGHTED PLATEAU

 42.62 ± 0.12

TOTAL FUSION

 42.86 ± 0.12

NORMAL ISOCHRON

 42.72 ± 0.37

INVERSE ISOCHRON

 42.74 ± 0.37

MSWD

(PROBABILITY)

0.97 (49%)

Sample Info

Plagioclase

West Cascades

Dan Miggins

IRR = 20-OSU-05

(SA30-20)

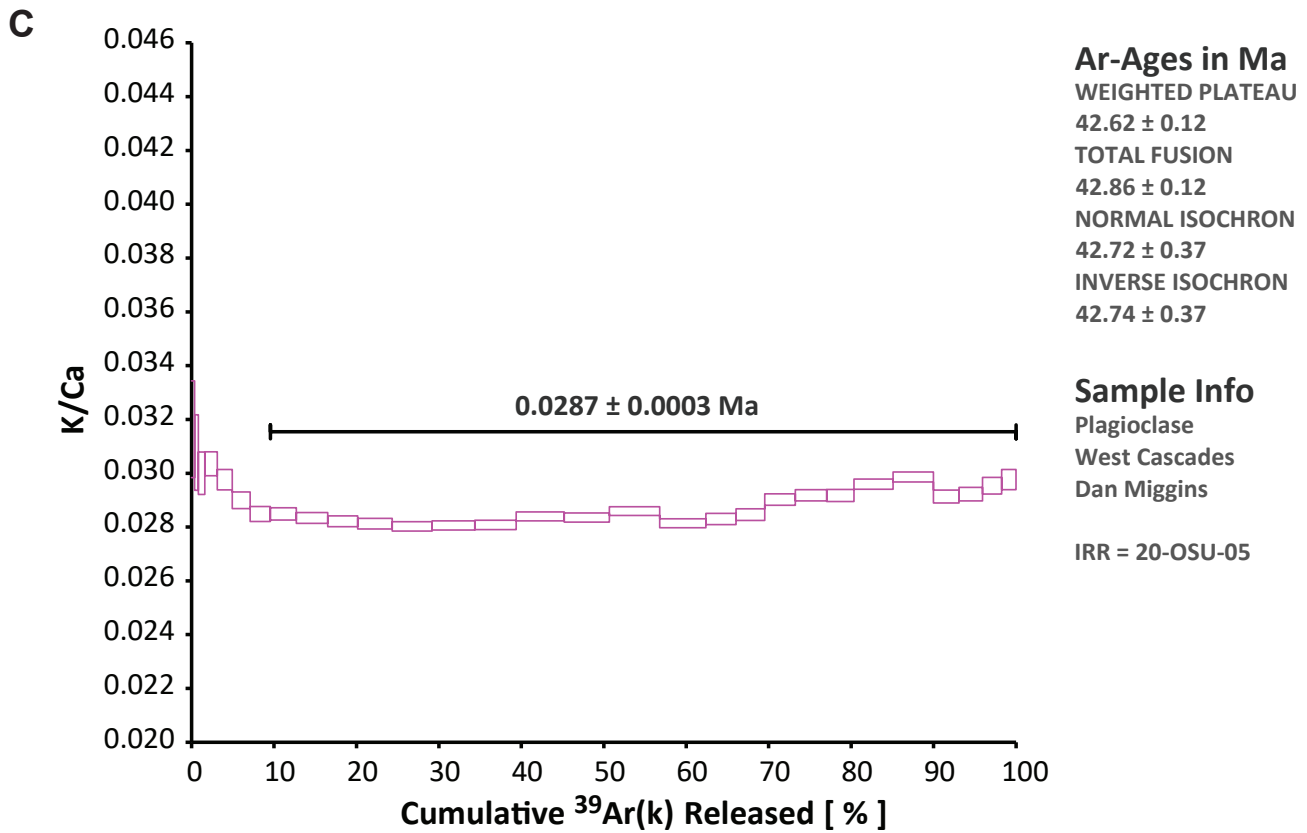
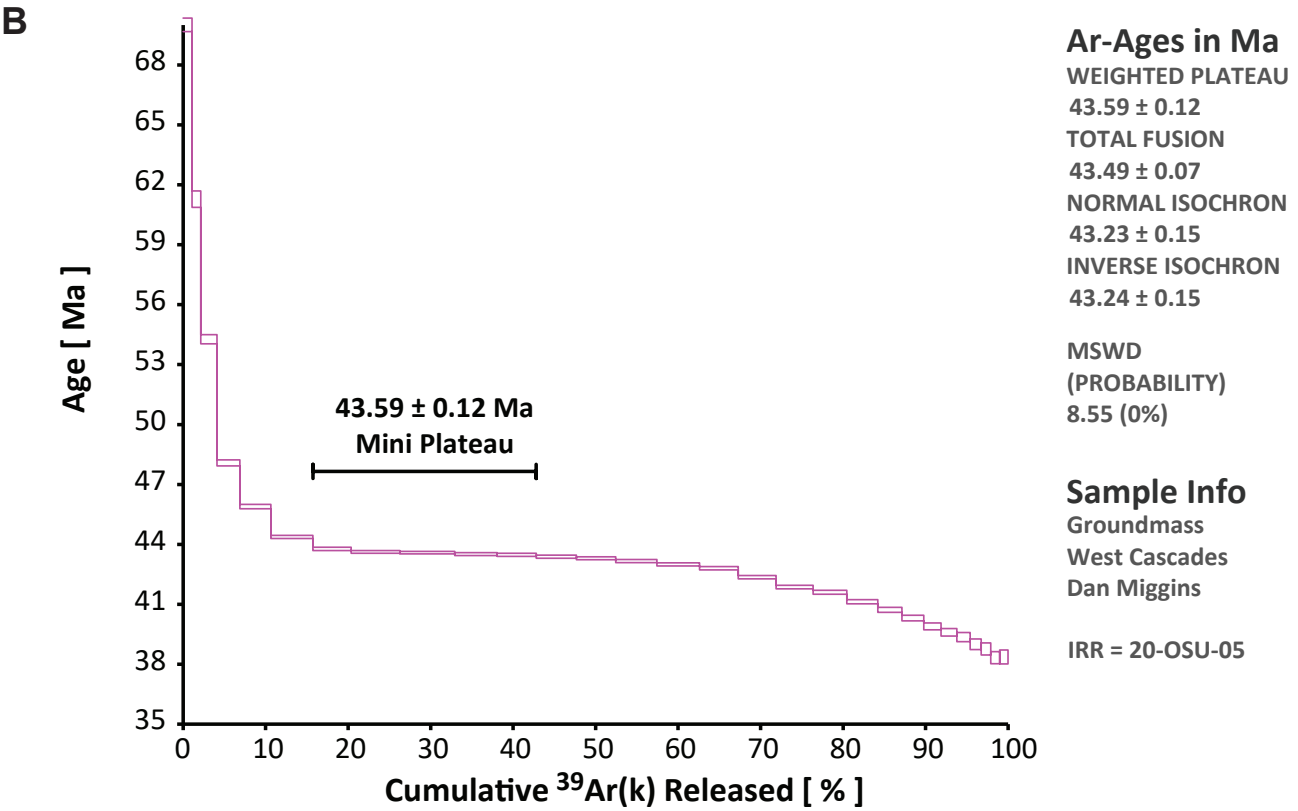
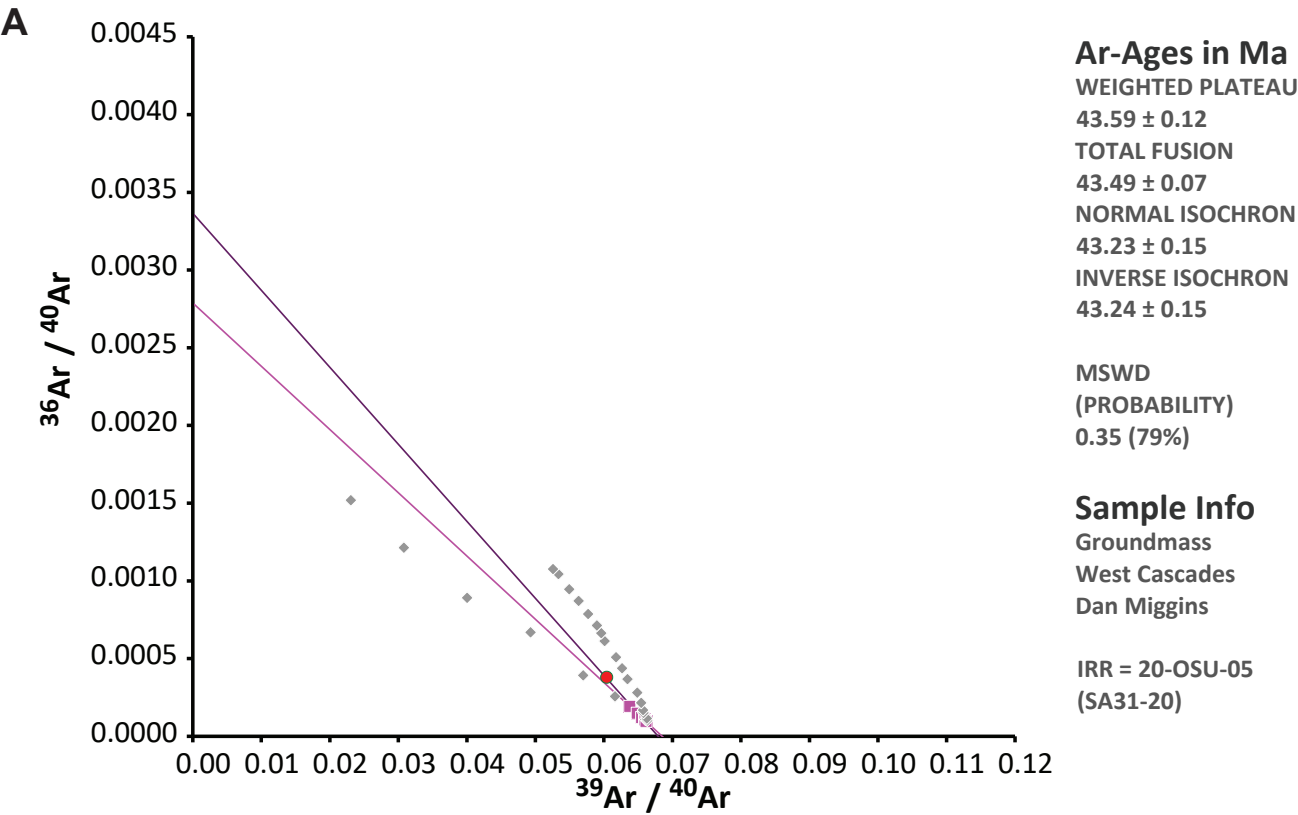


Figure C1. Step-heating results for $^{40}\text{Ar}/^{39}\text{Ar}$ analysis on unit Evan at age site GD5. Analysis was conducted on plagioclase grains. Subfigure A is a concordia diagram. Black bars in Subfigures B and C identify heating steps included in age estimate. Subfigure C shows the step-heating evolution of the K/Ca ratio.



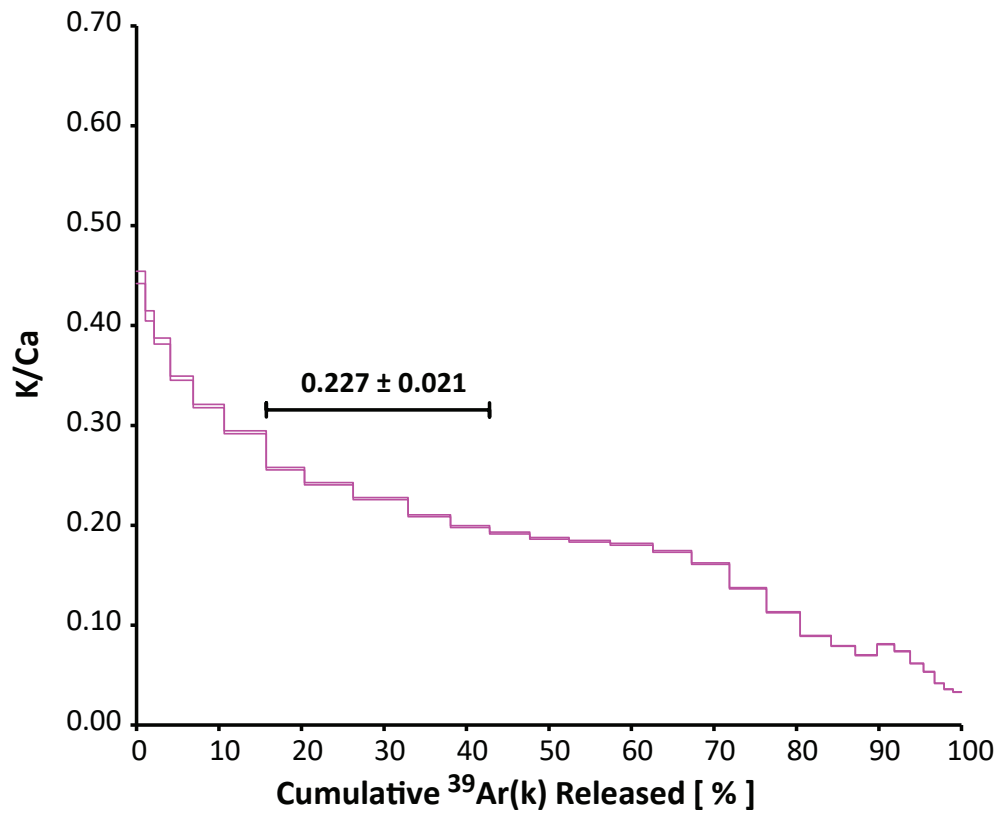
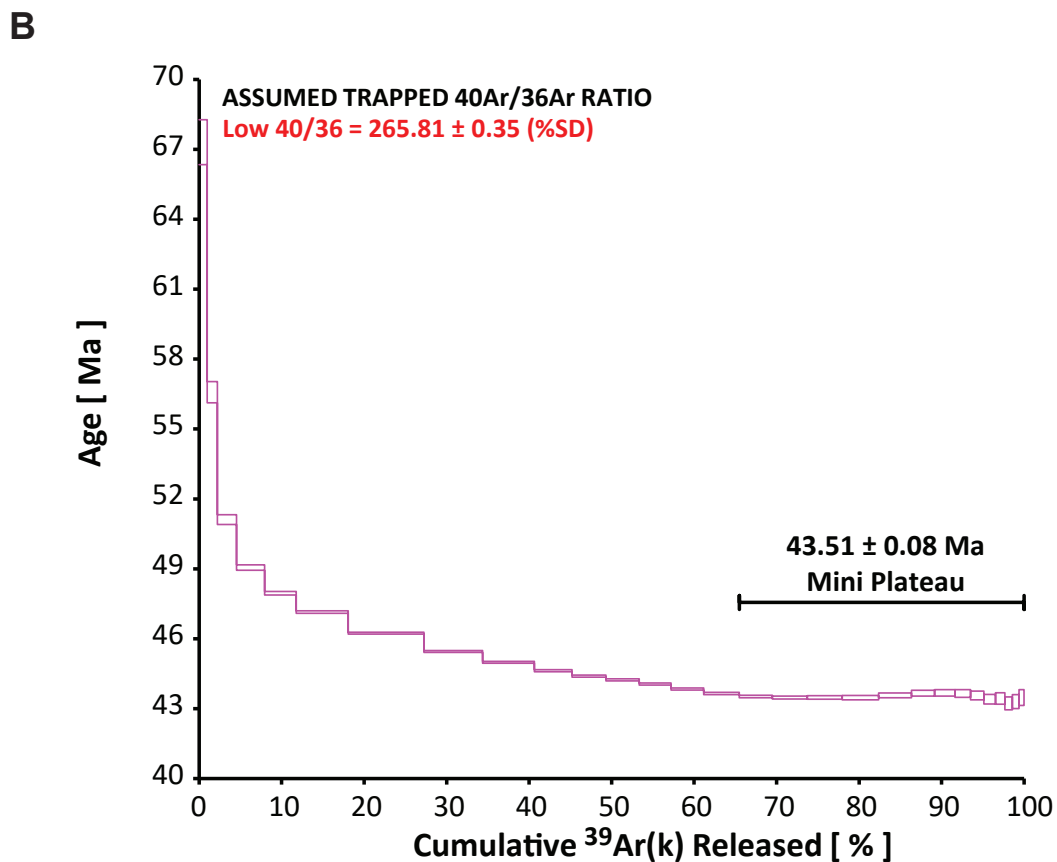
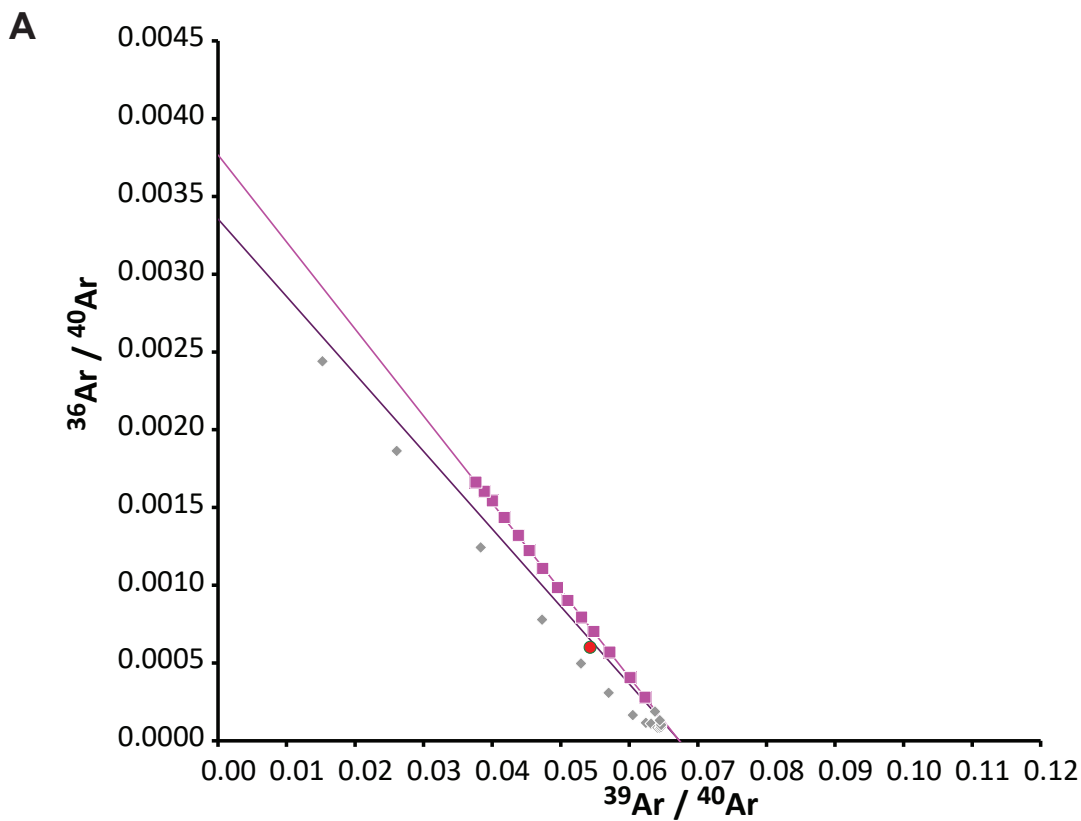
C

Figure C2. Step-heating results for $^{40}\text{Ar}/^{39}\text{Ar}$ analysis on unit Ev_n at age site GD6. Analysis was conducted on groundmass grains. Subfigure A is a concordia diagram. Black bars in Subfigures B and C identify heating steps included in age estimate. Subfigure C shows the step-heating evolution of the K/Ca ratio.



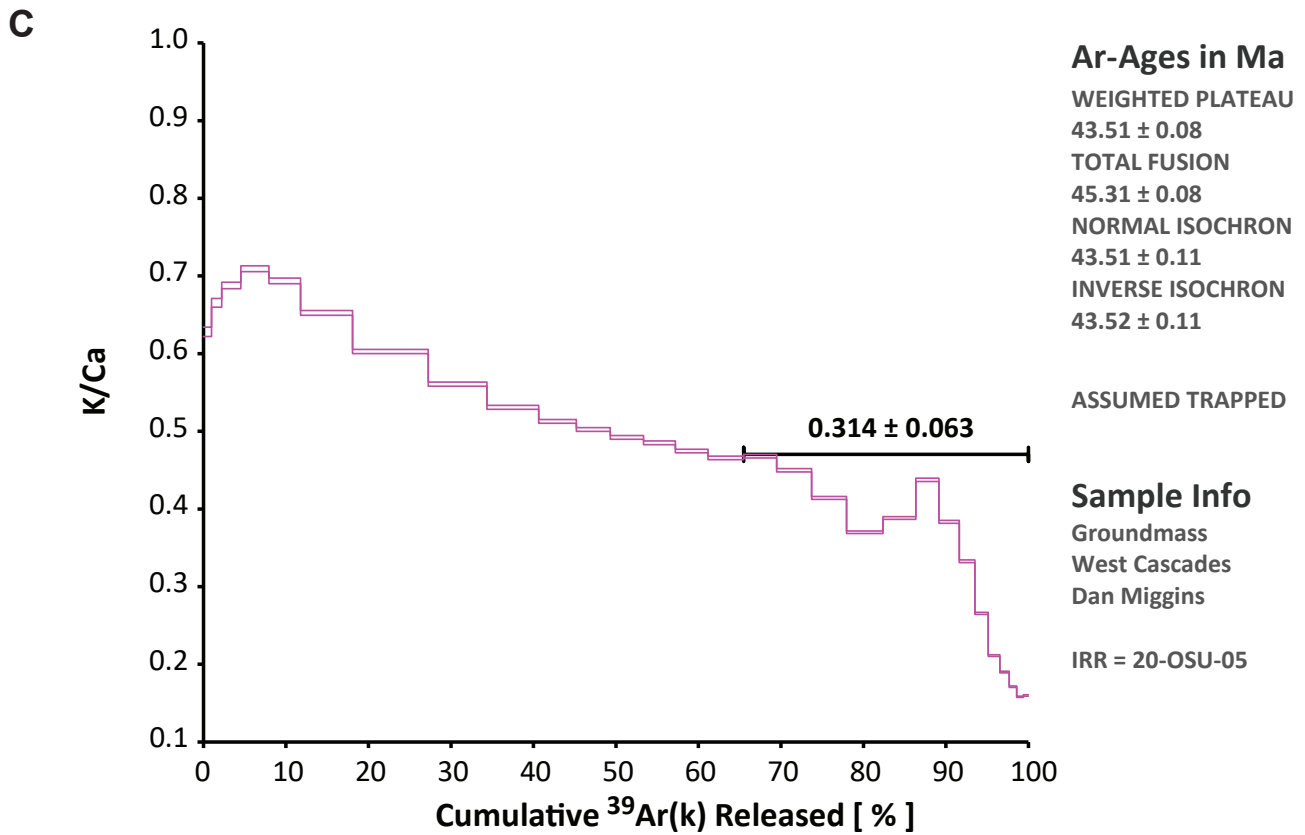
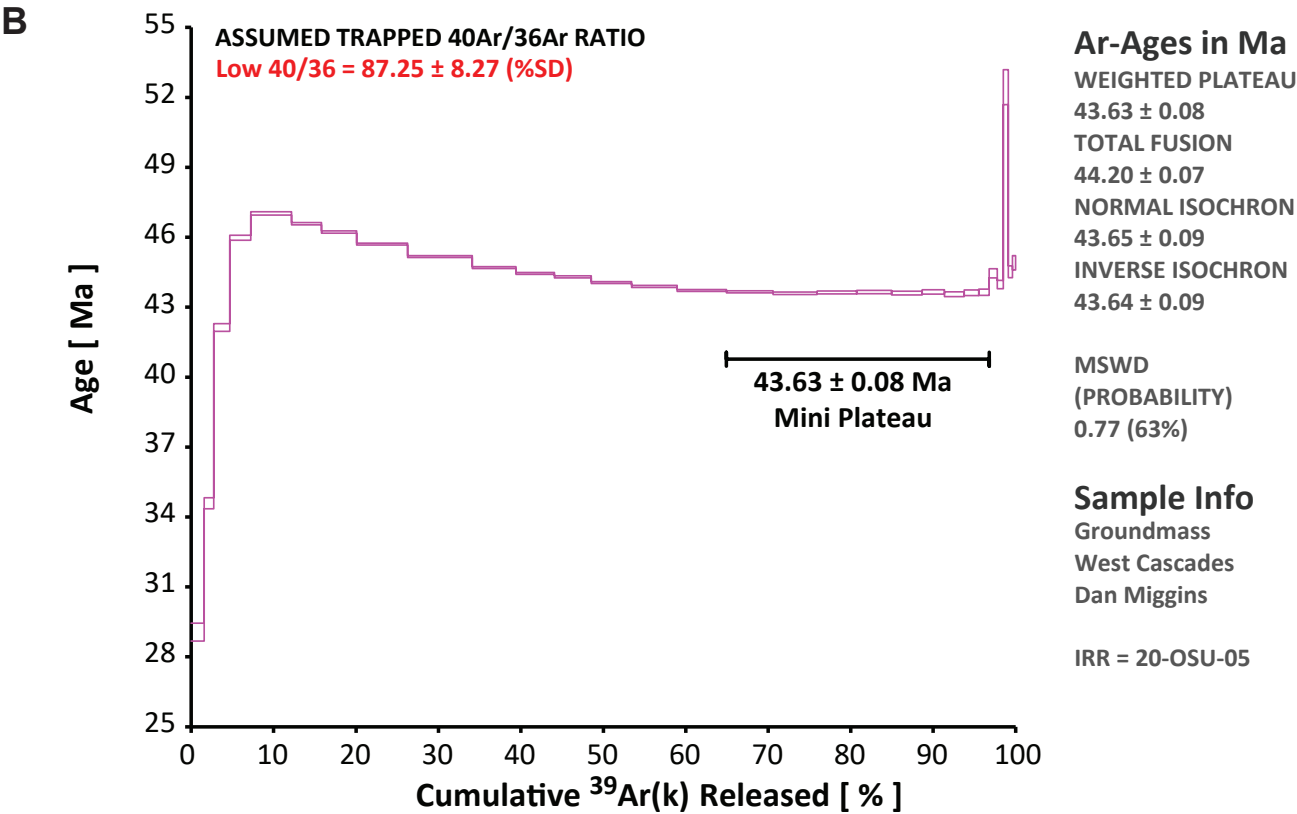
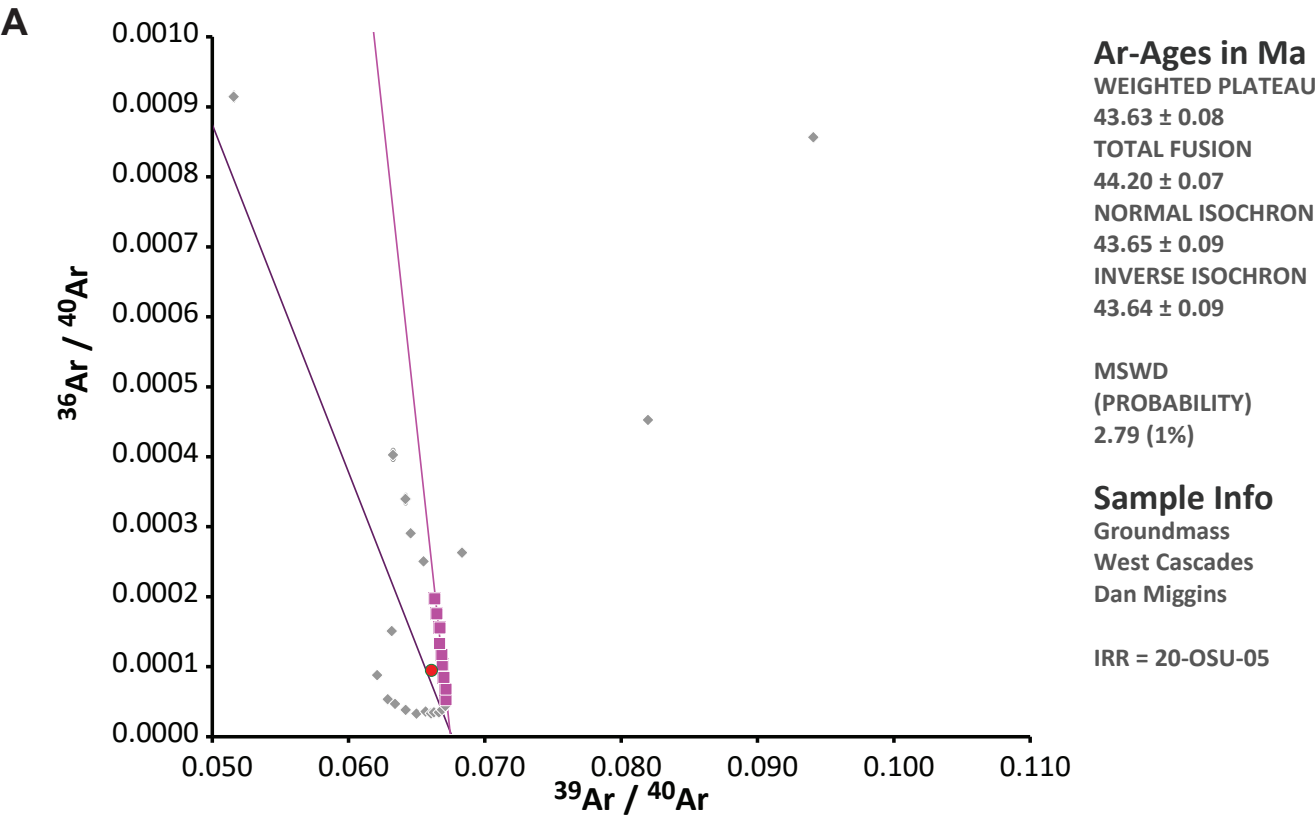


Figure C3. Step-heating results for $^{40}\text{Ar}/^{39}\text{Ar}$ analysis on unit Evn_1 at age site GD7. Analysis was conducted on groundmass grains. Subfigure A is a concordia diagram. Black bars in Subfigures B and C identify heating steps included in age estimate. Subfigure C shows the step-heating evolution of the K/Ca ratio.



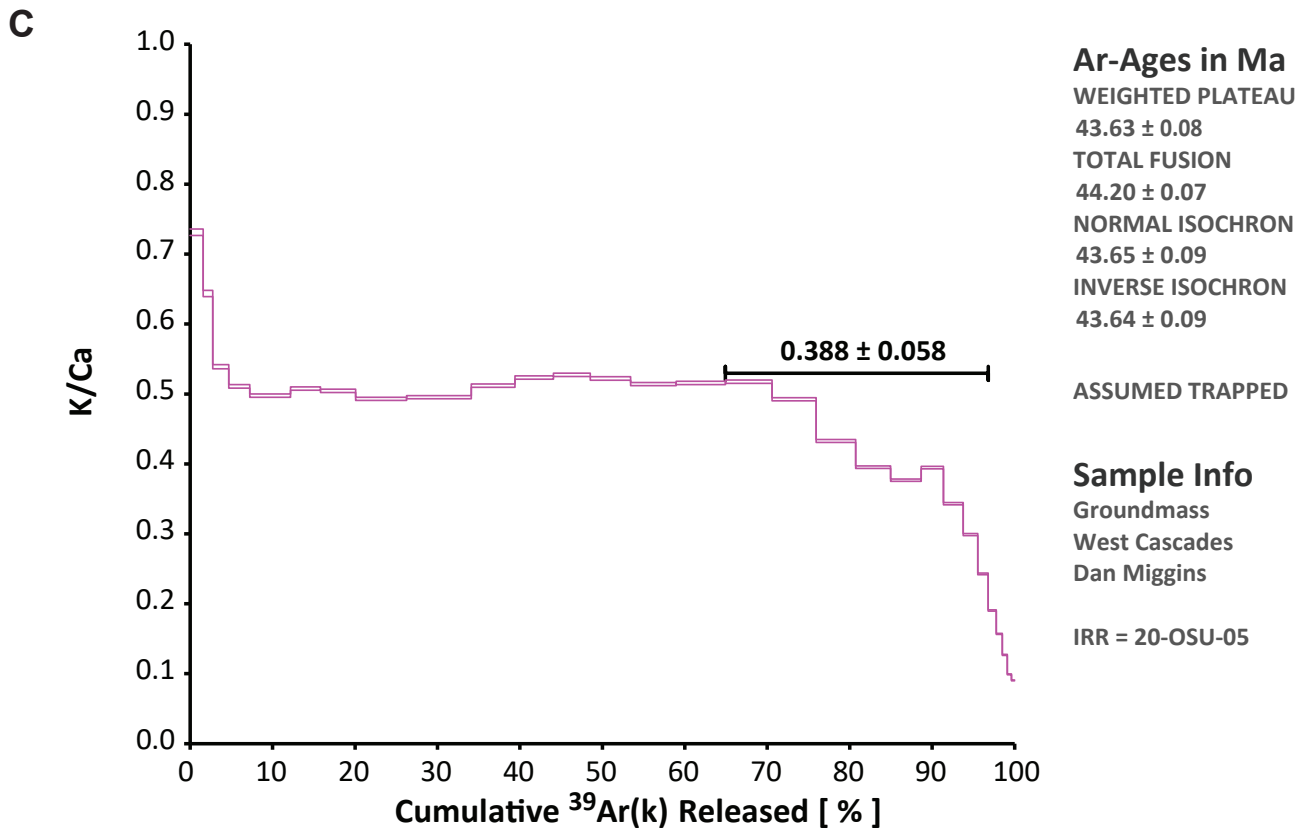
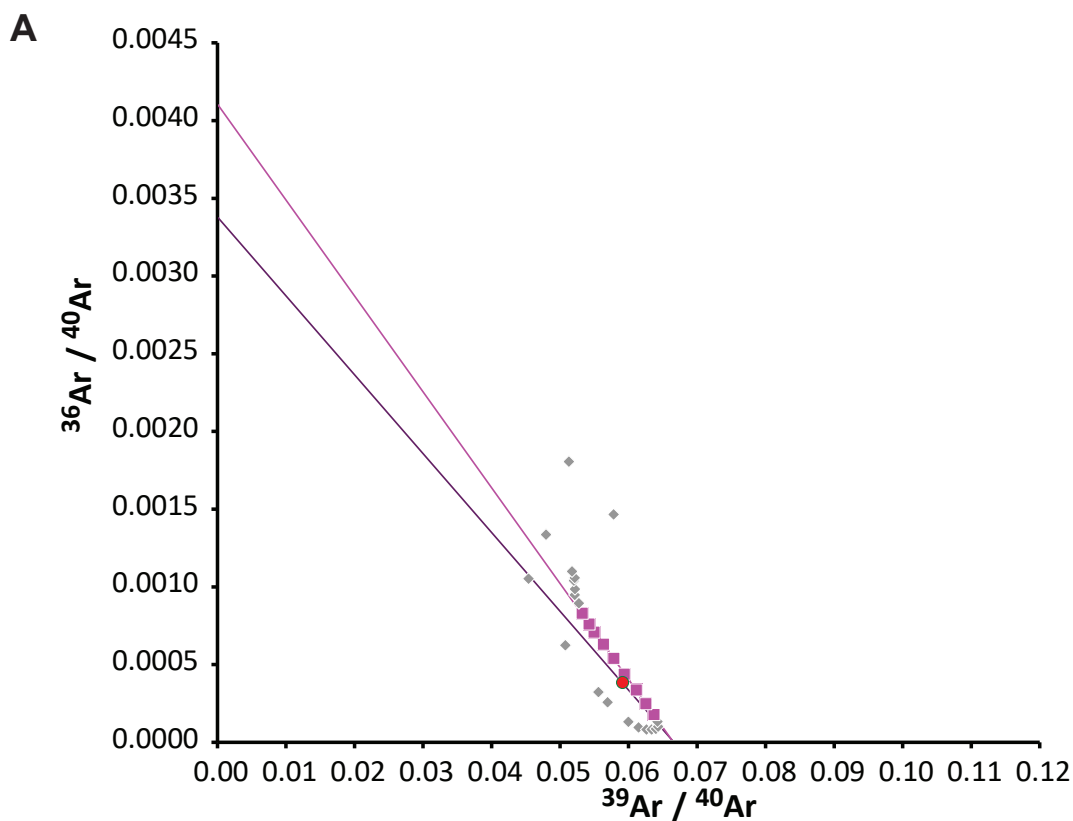


Figure C4. Step-heating results for $^{40}\text{Ar}/^{39}\text{Ar}$ analysis on unit Evan at age site GD8. Analysis was conducted on groundmass grains. Subfigure A is a concordia diagram. Black bars in Subfigures B and C identify heating steps included in age estimate. Subfigure C shows the step-heating evolution of the K/Ca ratio.

**Ar-Ages in Ma**

WEIGHTED PLATEAU

 44.08 ± 0.08

TOTAL FUSION

 44.97 ± 0.07

NORMAL ISOCHRON

 44.04 ± 0.10

INVERSE ISOCHRON

 44.05 ± 0.10

MSWD

(PROBABILITY)

3.43 (0%)

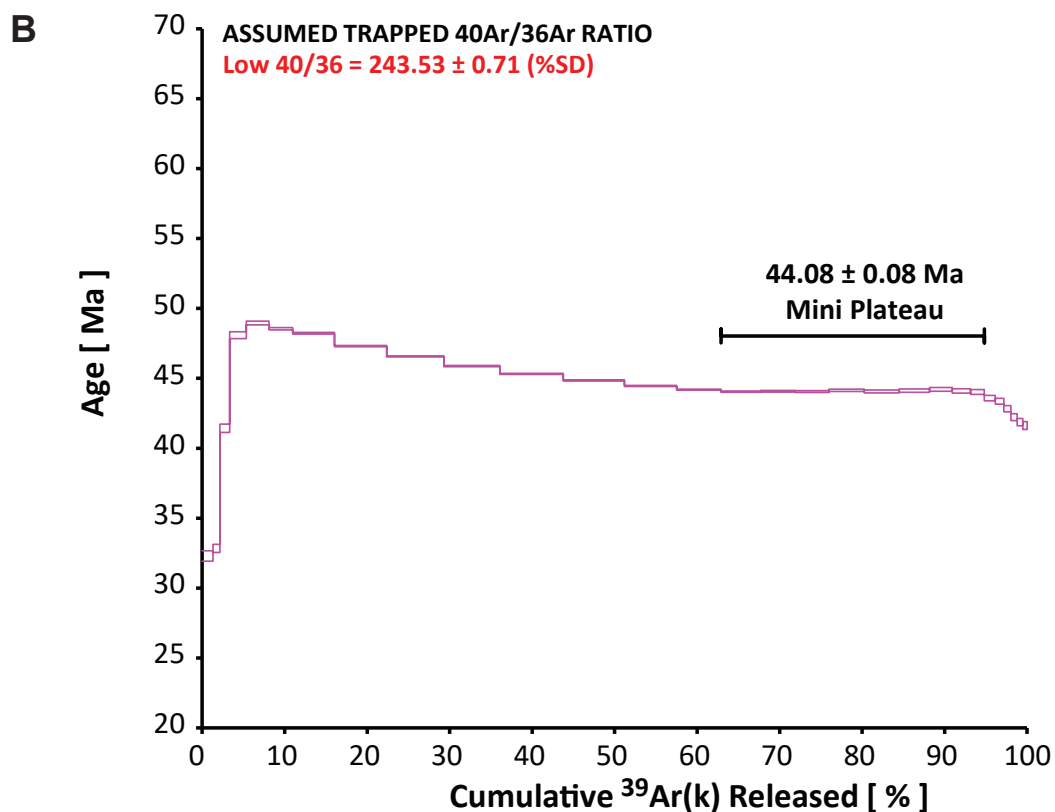
Sample Info

Groundmass

West Cascades

Dan Miggins

IRR = 20-OSU-05

**Ar-Ages in Ma**

WEIGHTED PLATEAU

 44.08 ± 0.08

TOTAL FUSION

 44.97 ± 0.07

NORMAL ISOCHRON

 44.04 ± 0.10

INVERSE ISOCHRON

 44.05 ± 0.10

MSWD

(PROBABILITY)

1.15 (33%)

Sample Info

Groundmass

West Cascades

Dan Miggins

IRR = 20-OSU-05

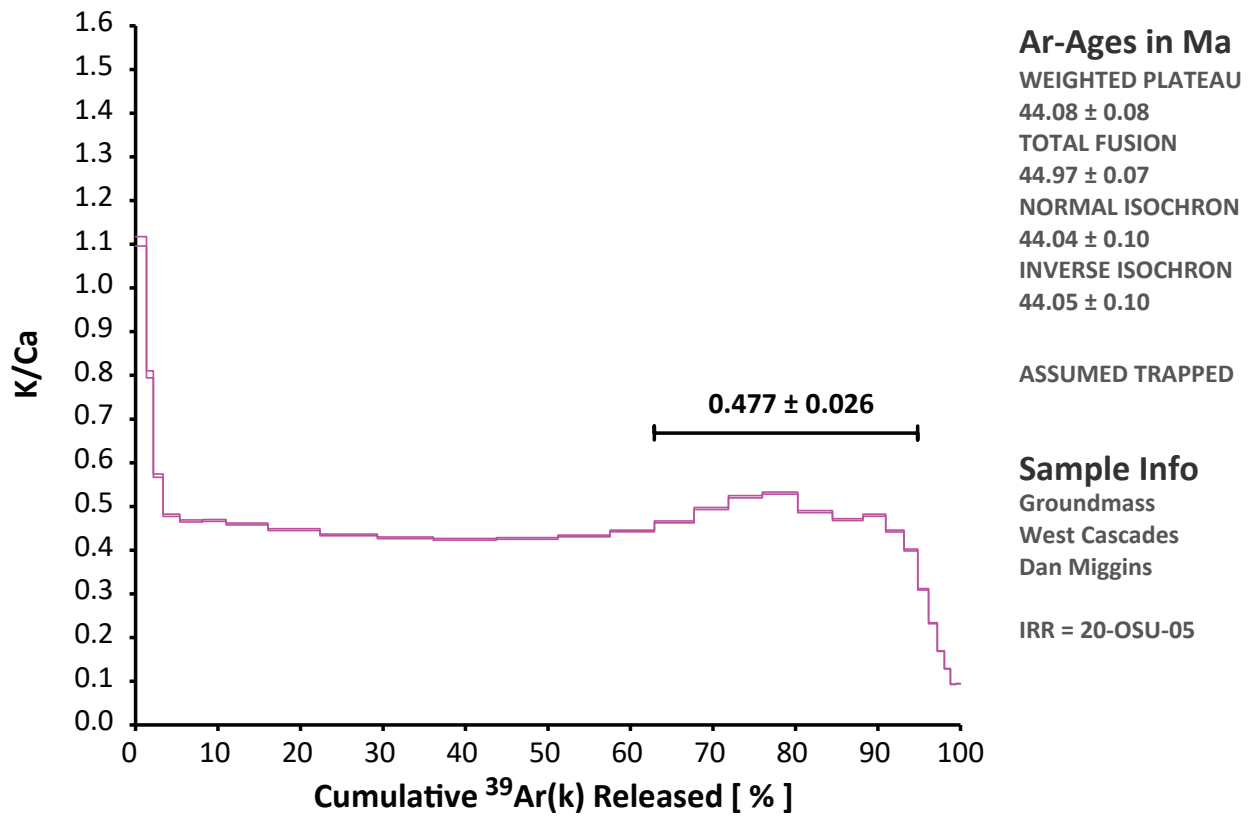
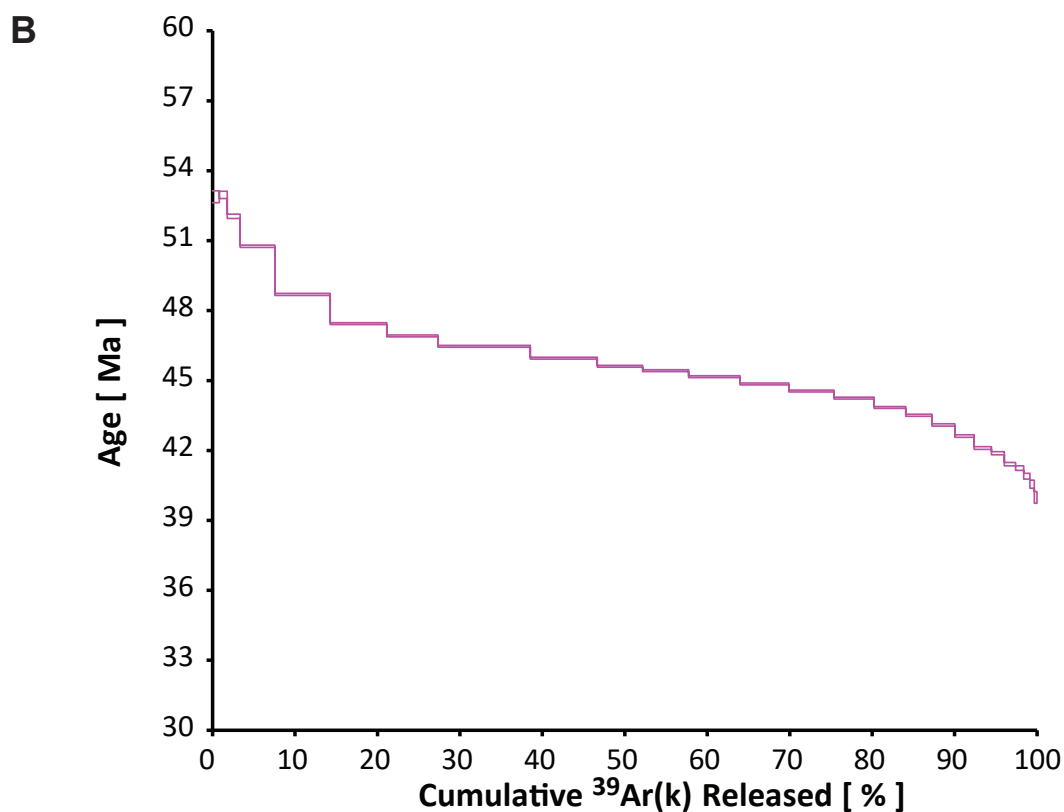
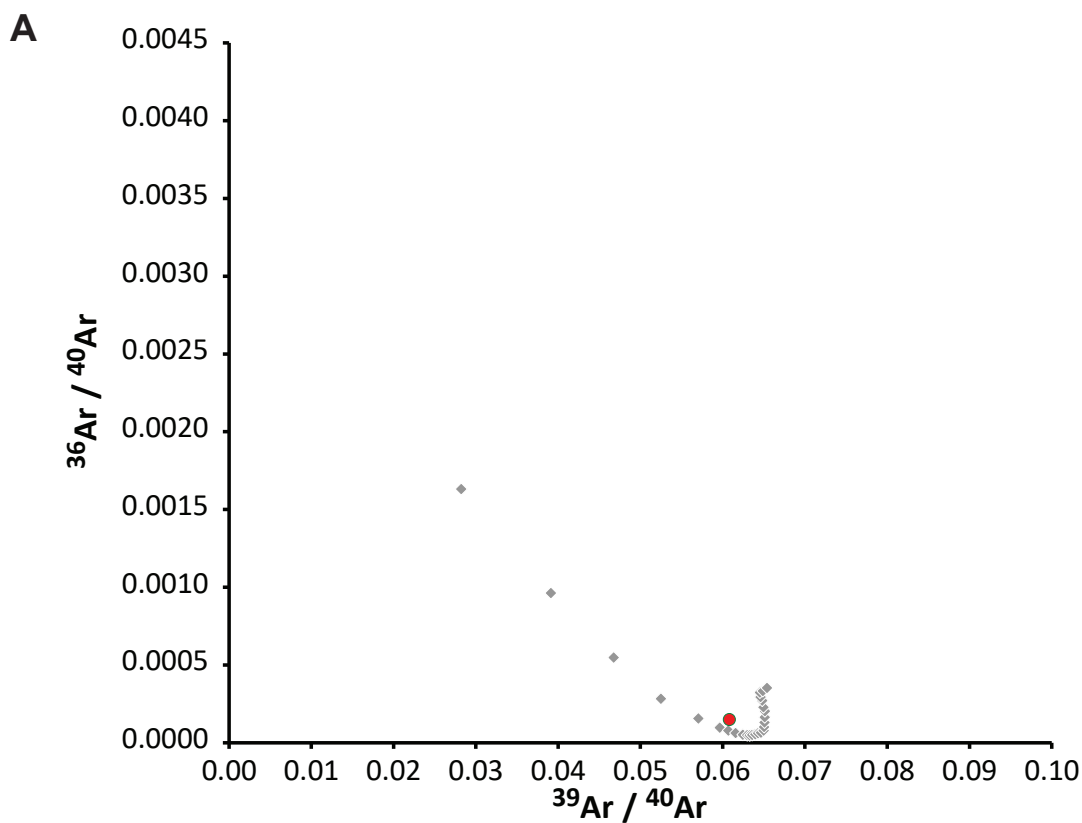
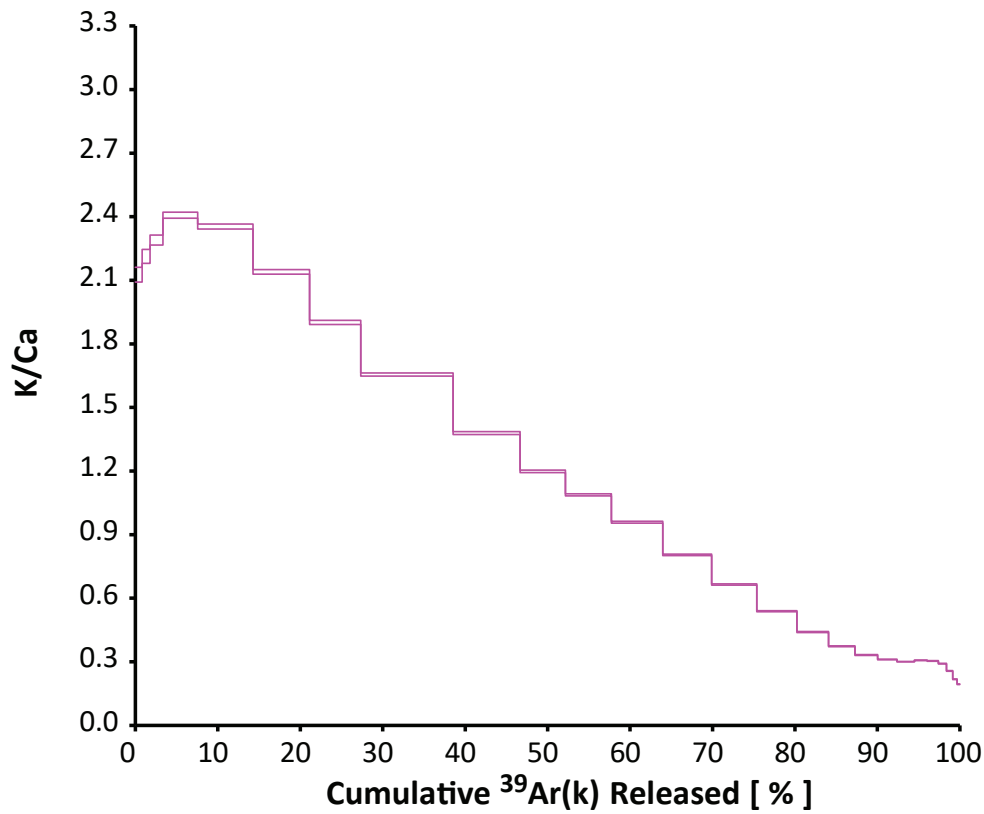
C

Figure C5. Step-heating results for $^{40}\text{Ar}/^{39}\text{Ar}$ analysis on unit Evan at age site GD9. Analysis was conducted on groundmass grains. Subfigure A is a concordia diagram. Black bars in Subfigures B and C identify heating steps included in age estimate. Subfigure C shows the step-heating evolution of the K/Ca ratio.



C**Ar-Ages in Ma****TOTAL FUSION** 45.80 ± 0.07 **ASSUMED TRAPPED****40AR/36AR RATIO**

Standard 40/36 =

 $298.56 \pm 0.104 \%SD$ **Sample Info**

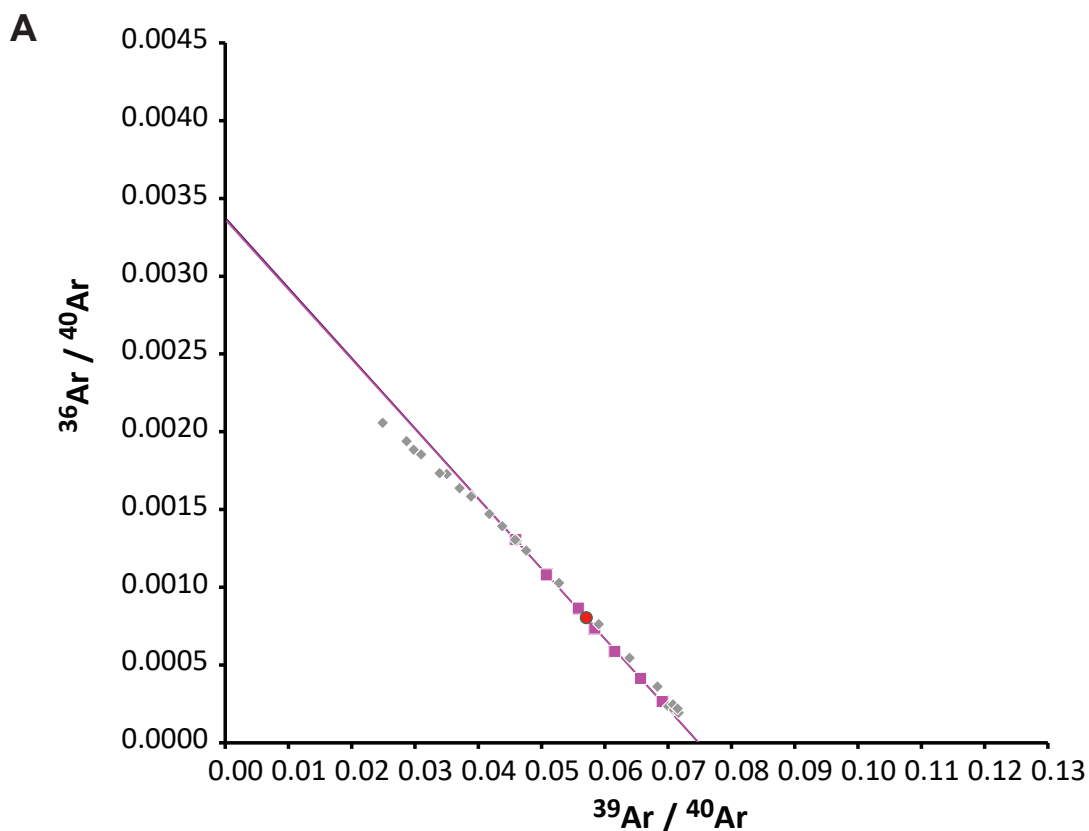
Groundmass

West Cascades

Dan Miggins

IRR = 20-OSU-05

Figure C6. Step-heating results for $^{40}\text{Ar}/^{39}\text{Ar}$ analysis on unit Evān at age site GD10. Analysis was conducted on groundmass grains. Subfigure A is a concordia diagram. Black bars in Subfigures B and C identify heating steps included in age estimate. Subfigure C shows the step-heating evolution of the K/Ca ratio.

**Ar-Ages in Ma**

WEIGHTED PLATEAU

 38.75 ± 0.13

TOTAL FUSION

 38.70 ± 0.12

NORMAL ISOCHRON

 38.71 ± 0.17

INVERSE ISOCHRON

 38.72 ± 0.17

MSWD

(PROBABILITY)

6.18 (0%)

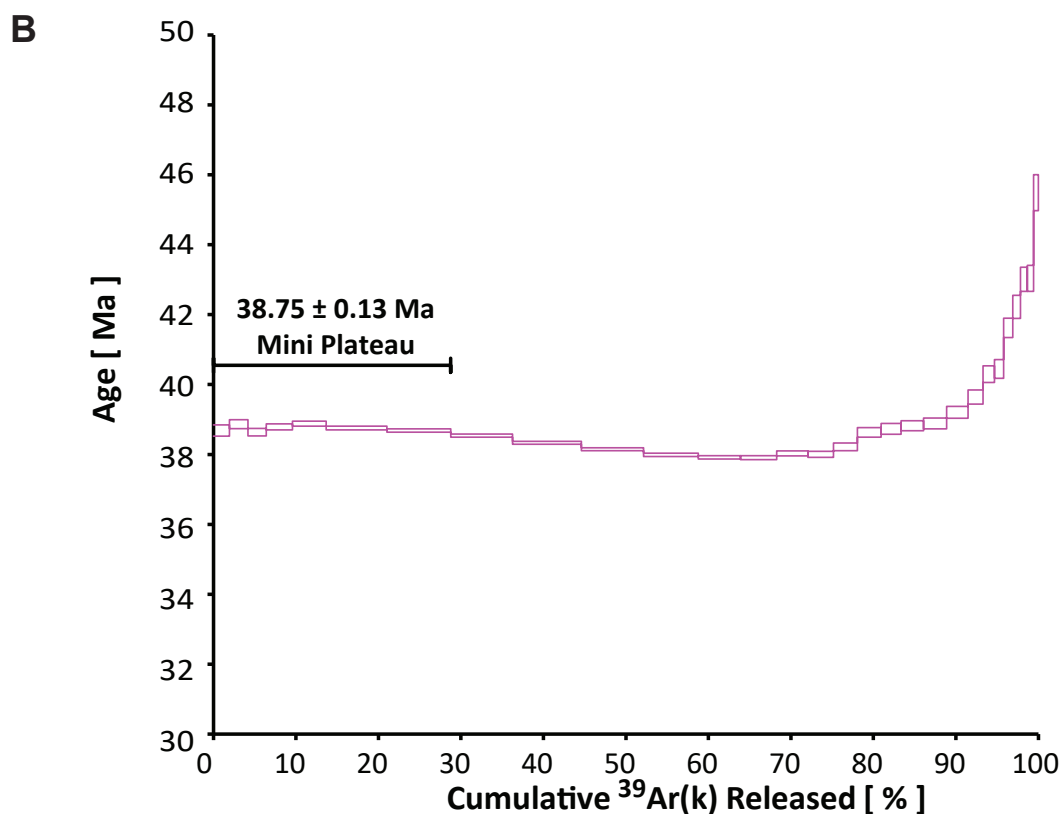
Sample Info

Groundmass

Columbia Quarry

Daniel Heaton

IRR = 21-OSU-01

**Ar-Ages in Ma**

WEIGHTED PLATEAU

 38.75 ± 0.13

TOTAL FUSION

 38.70 ± 0.12

NORMAL ISOCHRON

 38.71 ± 0.17

INVERSE ISOCHRON

 38.72 ± 0.17

MSWD

(PROBABILITY)

5.27 (0%)

Sample Info

Groundmass

Columbia Quarry

Daniel Heaton

IRR = 21-OSU-01

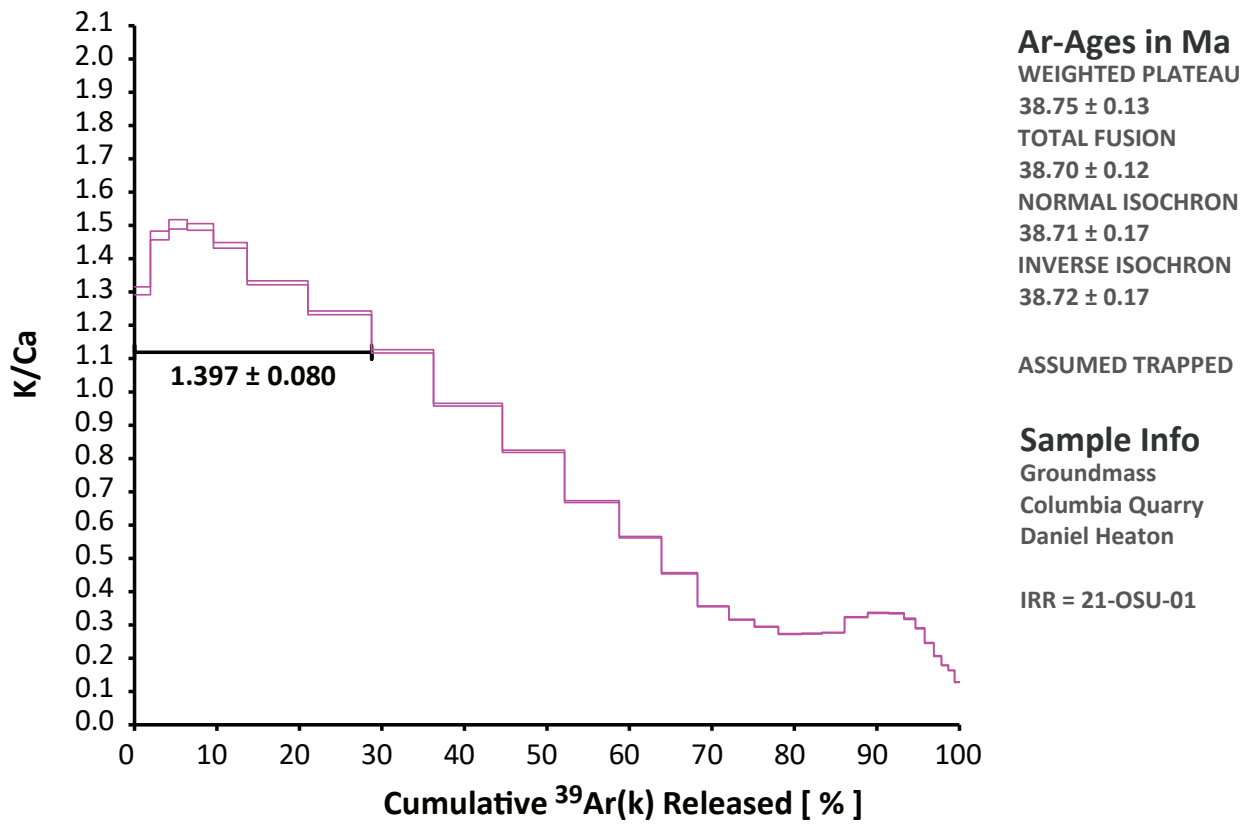
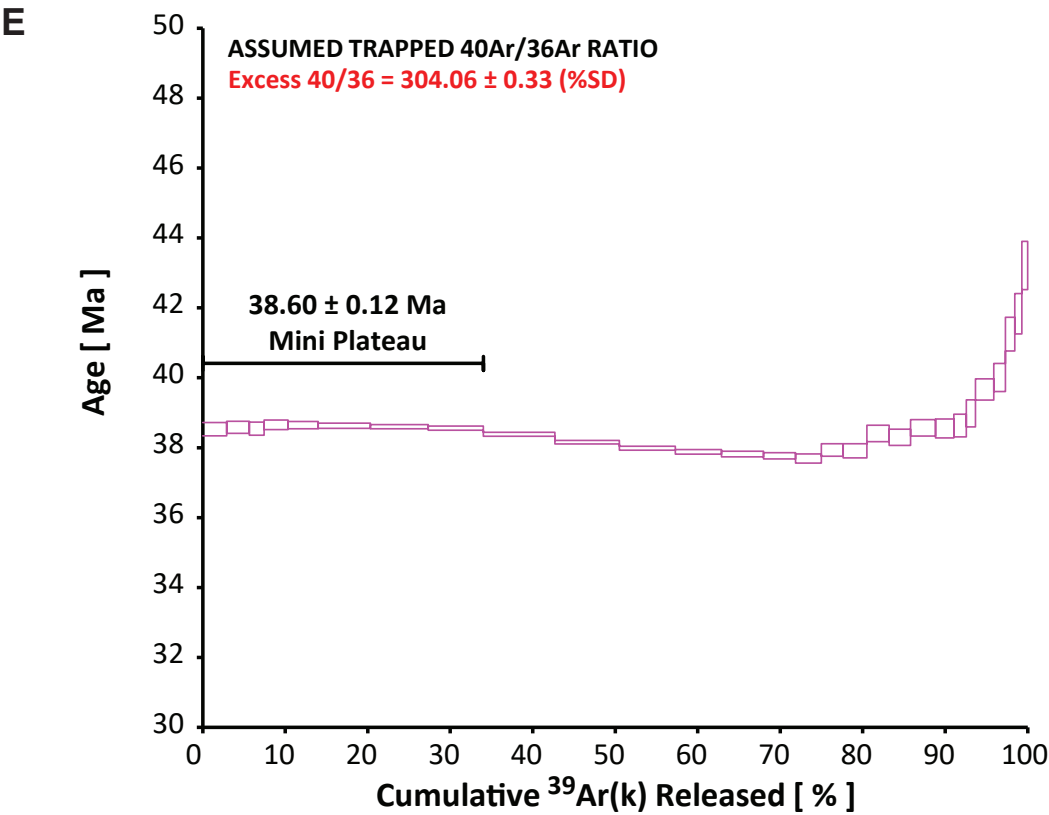
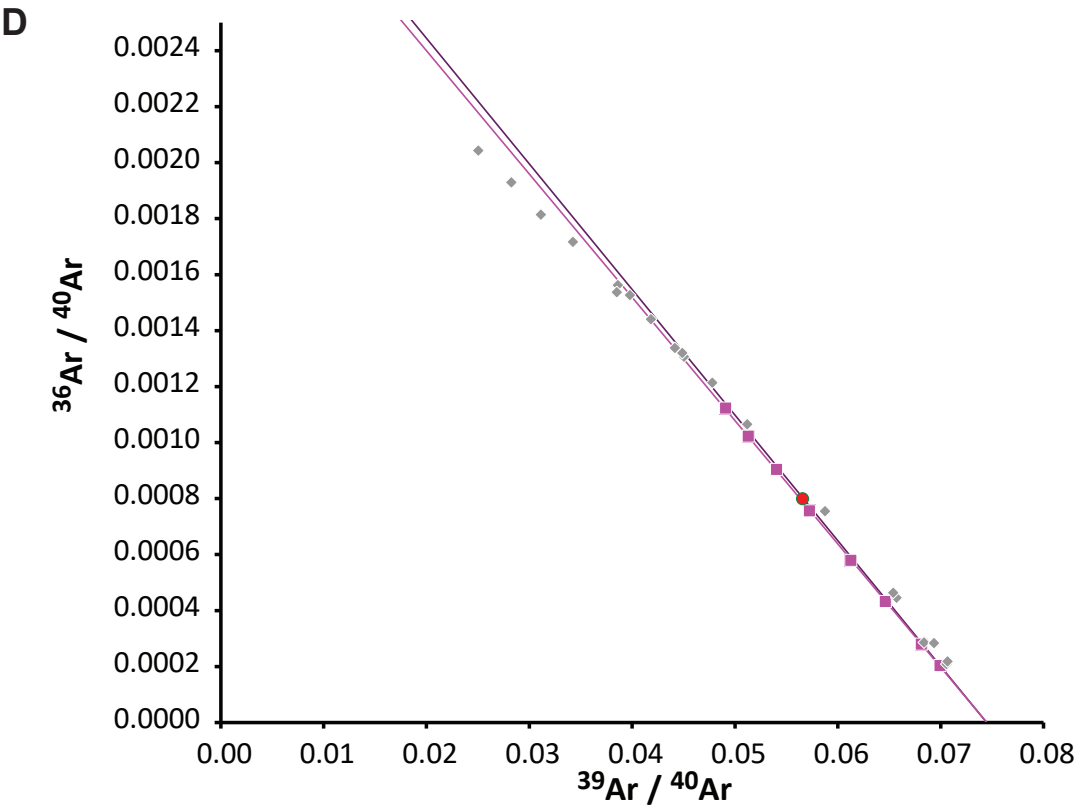
C

Figure C7. Step-heating results for $^{40}\text{Ar}/^{39}\text{Ar}$ analysis on unit Eign at age site GD11. Analysis was conducted on groundmass grains. Subfigure A is a concordia diagram. Black bars in Subfigures B and C identify heating steps included in age estimate. Subfigure C shows the step-heating evolution of the K/Ca ratio.



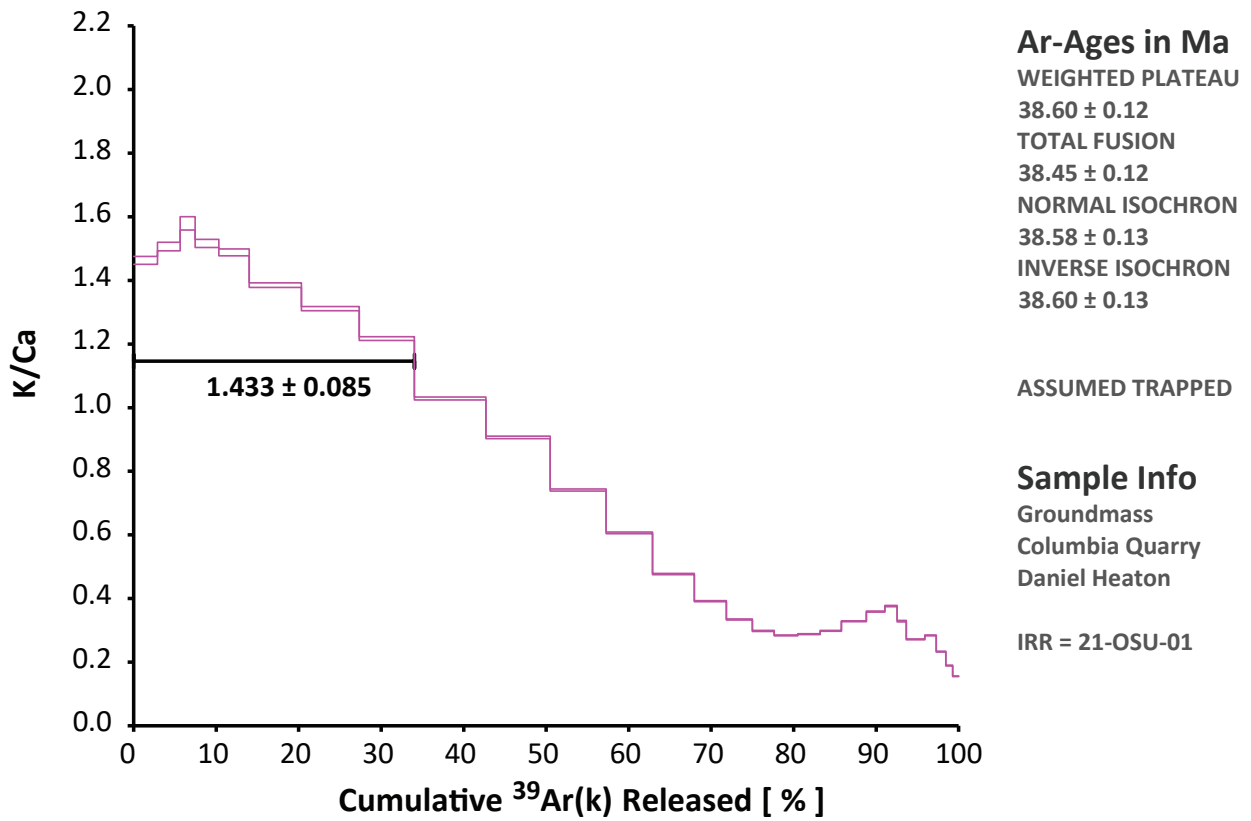
F

Figure C7 continued. Step-heating results for $^{40}\text{Ar}/^{39}\text{Ar}$ analysis on Eigh at age site GD11. Analysis was conducted on groundmass grains. Subfigure A is a concordia diagram. Black bars in Subfigures B and C identify heating steps included in age estimate. Subfigure C shows the step-heating evolution of the K/Ca ratio.